Cooperative and parametric strategies for 3D airborne electromagnetic inversion

by

Michael S. G. McMillan

B.Sc., The University of British Columbia, 2008

A THESIS SUBMITTED IN PARTIAL FULFILLMENT
OF THE REQUIREMENTS FOR THE DEGREE OF

Doctor of Philosophy

in

THE FACULTY OF GRADUATE AND POSTDOCTORAL STUDIES
(Geophysics)

The University of British Columbia
(Vancouver)

April 2017

Abstract

Airborne electromagnetic (AEM) data is commonly collected for detecting buried natural resources, and this technique is sensitive to subsurface electrical resistivity distributions. The subsequent process of 3D AEM inversion constructs a physical property model from this data in order to better understand the size and shape of potential hidden resources. This thesis is designed to develop practical strategies to improve 3D AEM inversion accuracy in geologic settings where AEM data sets produce inconsistent or unsatisfactory inversion results.

In this research, two overarching problematic scenarios are examined. First, in regions where an AEM survey overlaps with other electromagnetic data sets, a novel cooperative approach is introduced. This method is first tested on synthetic data where instead of producing an inversion model from each data set, the cooperative algorithm finds one consistent 3D resistivity model with improved resolution. The approach is then applied to field data over a high-sulfidation epithermal gold deposit where similar improvements are observed.

The second scenario relates to improving 3D AEM inversions over thin conductive anomalies, a common geophysical target for copper and gold deposits. A new parametric inversion is developed using skewed Gaussian ellipsoids to represent target bodies. The approach is general but applied to frequency and time-domain AEM data with one or multiple anomalies. Combined with a voxel algorithm, the parametric inversion forms a hybrid approach capable of resolving thin conductive targets with smooth surrounding features. This hybrid technique is tested on synthetic data over conductive targets in a resistive background, and consistently produces models that are easier to interpret compared to voxel inversions alone. Field examples from a volcanogenic massive sulfide and an orogenic gold deposit

highlight the practical nature of this method to image conductive mineralization with increased precision.

The thesis concludes by analyzing a setting where multiple spatially overlapping AEM data sets exist over narrow conductive anomalies. Here, parametric, cooperative and voxel inversions are applied together to generate a consistent 3D resistivity model with thin targets and smooth background features. This section includes a discussion about potential pitfalls of such an approach when incompatible field measurements are encountered.

Preface

The following document presents original research I completed at the Geophysical Inversion Facility (GIF) in the Department of Earth, Ocean and Atmospheric Sciences at the University of British Columbia (UBC), Vancouver, Canada. Portions of this research can be located in two peer-reviewed journal articles as well as seven expanded conference proceedings, and I have presented this work at nine conferences worldwide.

Chapter 2 contains text and figures from the published paper McMillan and Oldenburg (2014) in *Geophysics*. I came up with the idea, carried out the numerical experiments and wrote the manuscript. Dr. Douglas Oldenburg helped to edit the manuscript and Dr. Eldad Haber assisted with some of the numerical content. The work first appeared in the SEG expanded abstract McMillan and Oldenburg (2012).

Chapter 3 is a revised version of the published paper McMillan et al. (2015c) in *Geophysics*. The idea developed from discussions with Dr. Eldad Haber, Dr. Elliot Holtham and myself. I performed the numerical experiments with help from Dr. Christoph Schwarzbach, and I wrote the journal paper with editing help from Dr. Douglas Oldenburg. The work was first shown in the SEG expanded abstract McMillan et al. (2014).

Chapter 4 is currently in preparation for submission. The idea was my own, I did the numerical experiments with help from Dr. Christoph Schwarzbach, and I wrote the resulting chapter with edits from Dr. Douglas Oldenburg. The work first appeared in the EAGE expanded abstract McMillan et al. (2015b).

Chapter 5 is part of ongoing research that will lead to a future publication. I thought of the idea, and I completed the numerical trials with help from Dr. Christoph Schwarzbach and Dr. Eldad Haber. I wrote the chapter with edits from

Dr. Douglas Oldenburg, and the work was first shown in the EAGE expanded abstract McMillan et al. (2016).

Appendix A and Appendix B contain material relevant to Chapter 4 and Chapter 5 and represents more of my original research.

This thesis manuscript is entirely my own work, and I prepared it and wrote it with editing help from Dr. Douglas Oldenburg and Dr. Eldad Haber.

Table of Contents

List of Tables

List of Figures

Acknowledgments

This epic adventure known as a Ph.D. degree would not have been possible without the help of countless people along the way. My teachers and instructors have provided an amazing learning pathway for which I am forever grateful, from elementary school in Smithers, B.C. all the way to professors in graduate school at UBC. To Doug Oldenburg, who introduced me to applied geophysics back in 2007, and who continues to support me, I owe more than words can describe. To Eldad Haber, who has given me the most unique type of nebulous guidance along with plenty of criticism throughout my Ph.D., I thank for making this process as entertaining as it has been rewarding. Roman Shekhtman also needs special thanks for being the glue that holds the whole UBC-GIF group together.

To my fellow graduate students at GIF who have gone through this adventure with me, thank you for your cooperation, support, encouragement and friendship. We have shared laughter, pain, happiness, suffering, joy, despair, love, heartbreak and every other possible human emotion over these six years. I look forward to following each of your successes in the future.

Thank you to NSERC for sponsoring much of this research, and to Newmont Mining and Computational Geosciences for allowing me to keep my fingers in the world of applied geophysics while pursuing a doctorate degree.

To my close friends, from Smithers, from UBC, from my travels near and far, I appreciate all the support that you guys have provided. In all my silly endeavors, I can always count on my huge network of amazing friends for help and advice.

Finally to my parents and to my brother, thank you for always believing in my abilities, it means the world to me and I could not have completed this degree without each of you.

Chapter 1

Introduction

1.1 Research Motivation

The subsurface of the earth, in particular the top kilometer of the crust, contains most of the available natural resources that society will need over the course of the next generation. Whether it be in the search for metal, water, oil or other commodities of interest, accurately mapping these resources is vitally important for conservation, extraction and monitoring purposes. Imaging this upper crustal region of the earth with geophysical techniques is an appealing cost effective solution compared to the likes of drilling. One such geophysical method, broadly known as electromagnetics, is sensitive to electrical resistivity, which is a physical property that measures the degree to which a material opposes the flow of electric current. Variations in resistivity within the earth can indicate a change in rock type, alteration or in-situ fluid condition. These variations can in turn help locate and even characterize buried resources.

The usefulness of electromagnetic and specifically airborne electromagnetic (AEM) data for mineral exploration and commodity detection has been known for many decades. Companies have steadily acquired data in various configurations over the years, and as a result, an ongoing question is how to interpret the ensuing data sets. Only within the past decade has the AEM problem become tractable for 3D inversion, a process designed to reconstruct a feasible 3D earth model that best matches the collected electromagnetic observations. This is due to software

algorithms taking advantage of the increased computing power and novel massive parallelization options not previously available. Consequently, decades of historic data sets over a wide range of geologic targets are now being inverted with modern 3D techniques.

The process of inverting historic as well as modern data sets has opened up many new questions with regards to best practices for 3D AEM inversion. One scenario that commonly occurs due to the abundance of historic data sets, is what to do when two surveys have been collected over the same area but at different times. The question that arises is whether the information from each survey can be combined in a useful manner. The other common problem relates to the resolution of 3D inversion models. Often exploration companies plan drill holes based on 3D inversion models, and for certain targets such as narrow thin anomalies, conventional inversion results have trouble accurately representing this compact geometry. In this thesis, I introduce novel algorithms and develop practical strategies to address these questions with regards to improving the accuracy and capabilities of 3D frequency and time-domain AEM inversion.

This first introductory chapter will present a review on general electromagnetics and relevant equations, the airborne electromagnetic method, fundamentals of voxel, cooperative and parametric 3D inversion and will conclude with an outline of the thesis.

1.2 Electromagnetic Survey Techniques

Electromagnetic surveys detect contrasts in electrical resistivity, which can help distinguish rock types and alteration zones within the earth (Keller, 1988). But, these data can be collected in a multitude of ways, and selecting an appropriate survey design is critical to ensure that the target of interest can be imaged. A general electromagnetic layout consists of a transmitter that generates a signal that penetrates the ground and a set of one or more receivers that measure the induced response that emanates from the earth. When designing a survey, there are many choices to consider in terms of the type of transmitter and receiver to use and how to place these instruments during data acquisition. Some major distinctions between survey configurations are listed below.

1. Type of transmitter - inductive, galvanic or natural source.

2. Type of receiver measurements - electric field (**e**), magnetic flux (**b**) or time rate of change of magnetic flux ($\frac{\partial \mathbf{b}}{\partial t}$).

3. Spatial component of measurements - x, y, or z.

4. Transmitter and receiver locations - airborne, ground or borehole.

5. Domain of measurements - frequency or time domain.

This list is not meant to be exhaustive, but it is clear that many choices are available when designing an electromagnetic survey, and there are pros and cons to each choice depending on the goal of the particular project. In this thesis I will focus primarily on AEM configurations (Macnae et al., 1991) both in the frequency and time domain. AEM surveys have been collected since the late 1950's (Palacky and West, 1973), and deploy inductive sources, which excite the earth using a time-varying magnetic field. Figure 1.1 shows a cartoon of a generic frequency and time-domain helicopter AEM configuration. A frequency-domain setup generally consists of multiple small transmitter loops that can be oriented in any direction. Figure 1.1 depicts a simplified version with one transmitter loop in a horizontal coplanar orientation, also known as a vertical dipole. A time-domain system often possesses a much larger transmitter loop, and due to the size of the loop it is usually oriented in a horizontal fashion as shown in Figure 1.1. The heavier time-domain loop generally maintains a higher terrain clearance compared to the frequency-domain counterpart, but the exact terrain clearance will vary depending on the survey specifications and the amount of topography present in the area. Both frequency and time-domain AEM receivers are generally small loops located in the air that measure components of **b** or $\frac{\partial \mathbf{b}}{\partial t}$ from secondary fields induced in the earth by the transmitted source. These secondary fields are dependent on the true heterogeneous resistivity distribution of the earth, but for demonstration purposes can be thought of as due to a background resistivity ρ_0 and an anomalous target region ρ_1.

In the frequency domain, the transmitted waveform oscillates continuously as displayed in Figure 1.2a, and the recorded data from the receiver is decomposed

into real (in-phase with the transmitter source) and imaginary (out-of-phase with the transmitter source) components. Conversely in the time domain, the transmitter waveform is usually turned on for a period of time in a pulse-like manner with a large amount of current and then shut off as shown in Figure 1.2b. During this 'off-time', the receiver records the secondary fields from the earth in the absence of the transmitted primary signal. Note that many variations of waveforms are used in time-domain AEM systems, from square waves (Eaton et al., 2013) to triangular waves (Boyko et al., 2003) to half-sine waves (Mulè et al., 2012), with many combinations in between. Some newer systems combine two transmitter pulses, one high and one low amplitude pulse, to suit both deep and near-surface targets (Chen et al., 2015).

Other data sets mentioned throughout this work include controlled source audio frequency magnetotellurics (CSAMT) (Zonge and Hughes, 1991) and the direct current (DC) resistivity method (Kunetz, 1966). A CSAMT survey uses receivers on the ground to measure electric fields and magnetic fluxes in response to a galvanic transmitter many kilometers away that injects current directly into the earth at frequencies between 0.1 Hz and 10 kHz.

In contrast, a DC configuration is often considered an electrical technique, but it can be thought of as a special case of the electromagnetic method that operates at a near-zero frequency. The DC method injects current with a galvanic transmitter, and often operates in the time domain using a half-duty cycle square wave electric current with an eight second period. Frequency-domain DC surveys also exist, and they inject an oscillating electric current into the ground instead of a square wave. In either the time or frequency domain, DC data consist of electric potential differences measured between grounded receiver electrodes known as dipoles. CSAMT and DC data are sensitive to electrical conductivity, and as such they are both helpful to reconstruct conductivity distributions through Maxwell's equations.

1.3 Maxwell's Equations

Electromagnetic induction is governed by Maxwell's equations, which are written in quasi-static form in the time domain as

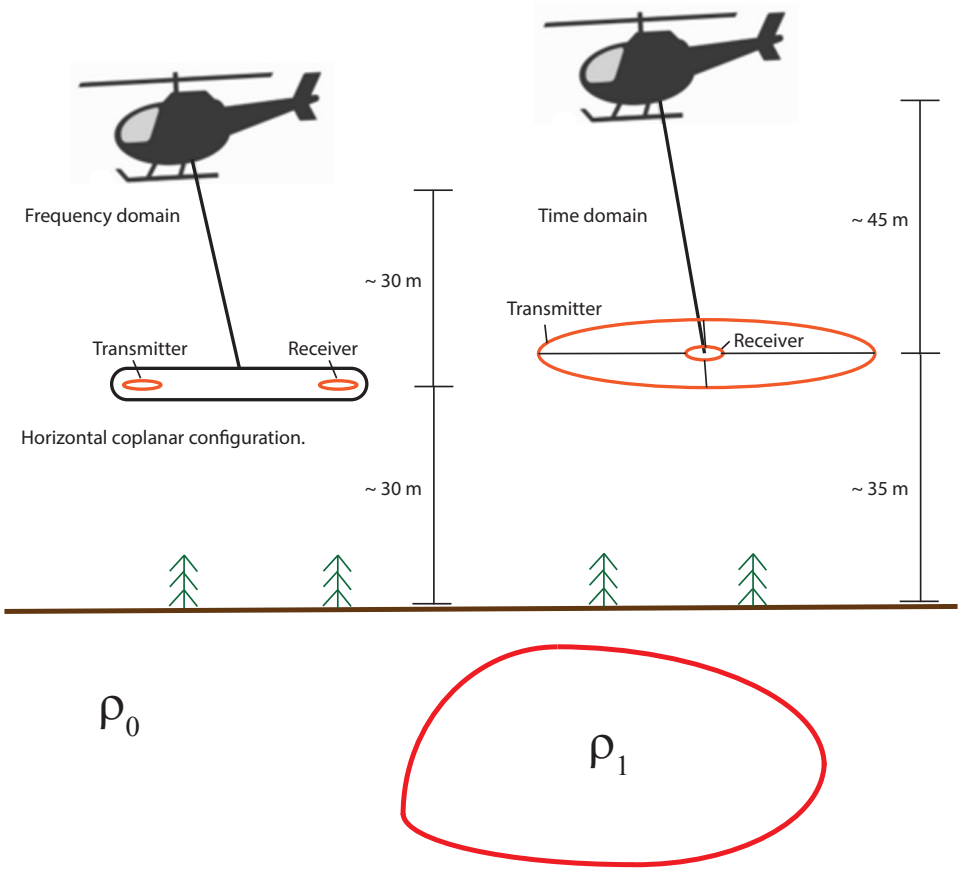

Figure 1.1: Simplified helicopter airborne electromagnetic setup for a generic frequency and time-domain system. ρ_0 is the background resistivity and ρ_1 represents the target resistivity.

$$\nabla \times \mathbf{e} + \mu \frac{\partial \mathbf{h}}{\partial t} = 0 \tag{1.1}$$

$$\nabla \times \mathbf{h} - \sigma \mathbf{e} = \mathbf{s} \tag{1.2}$$

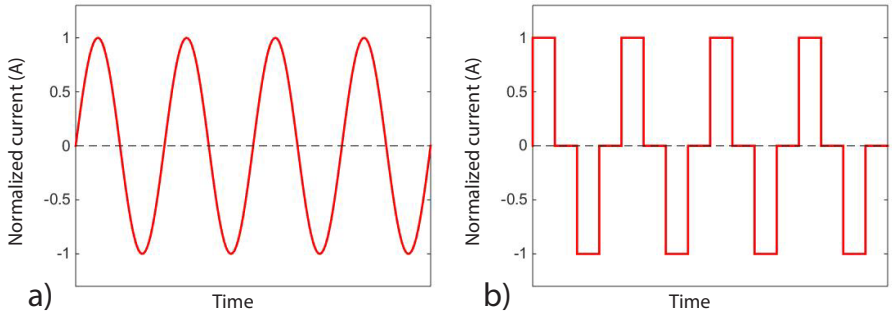

Figure 1.2: Generic frequency and time-domain waveforms used for an airborne electromagnetic survey. a) Frequency domain. b) Time domain.

where **e** is the electric field, **h** is the magnetic field, μ is the magnetic permeability, σ is the electrical conductivity and **s** is a source vector. Electrical resistivity ρ, the reciprocal of conductivity, is mentioned interchangeably with conductivity throughout this dissertation.

The same equations can be written in the frequency domain as

$$\nabla \times \mathbf{E} + i\omega\mu\mathbf{H} = 0 \tag{1.3}$$

$$\nabla \times \mathbf{H} - \sigma\mathbf{E} = \mathbf{S}. \tag{1.4}$$

where ω is the angular frequency and the capitalized notation represents the frequency-domain version of the fields and source term. The relationship between fields and fluxes is summarized by constitutive equations

$$\mathbf{B} = \mu\mathbf{H} \tag{1.5}$$

$$\mathbf{J} = \sigma\mathbf{E} \tag{1.6}$$

where **B** is the magnetic flux density and **J** is the current density vector. In this work we presume that $\mu = \mu_0$, the magnetic permeability of free space $(4\pi \times 10^{-7}\ \mathrm{N/A^2})$.

From Maxwell's equations, the skin depth (δ) can be derived, which is an

informative metric that describes the depth at which point the amplitude of the electromagnetic wave is reduced by a factor of 1 / e, and it is written as

$$\delta = \sqrt{\frac{2}{\mu_0 \sigma \omega}}. \tag{1.7}$$

The equivalent in the time domain is the diffusion distance (d) that describes the depth at which point the amplitude of the electromagnetic wave is at a maximum for a fixed time t, and it is written as

$$d = \sqrt{\frac{2t}{\mu_0 \sigma}}. \tag{1.8}$$

1.4 Electromagnetic Modeling and Inversion

This work builds upon techniques for discretizing Maxwell's equations for numerical modeling and inversion of electromagnetic data as shown in Haber et al. (2007b); Haber and Schwarzbach (2014); Oldenburg et al. (2013); Ruthotto et al. (2016). Namely that the forward problem is written as

$$F(\mathbf{m}) = \mathbf{d} \tag{1.9}$$

where F is a forward operator of Maxwell's equations, $\mathbf{m}$ is the relevant physical property (i.e. electrical conductivity or resistivity) and $\mathbf{d}$ is the data. The choice of discretization is a finite-volume approach, however finite-difference (Commer and Newman, 2004; Egbert and Kelbert, 2012; Weiss and Constable, 2006), finite-element (Key and Weiss, 2006; Li and Key, 2007; Schwarzbach and Haber, 2013) and integral equation (Cox et al., 2010; Zhdanov, 2010) techniques are also commonly employed. The inverse problem is then written as the optimization of

$$\arg\min_{\mathbf{m}} \phi(\mathbf{m}) = \phi_d(\mathbf{m}) + \beta \phi_m(\mathbf{m}) \tag{1.10}$$

where ϕ_d is the data misfit, ϕ_m is the model regularization term, and β is a trade-off or regularization parameter. The data misfit is defined by a least-squares measure

$$\phi_d(\mathbf{m}) = \|\mathbf{W}_d(\mathbf{d}_{\text{pred}} - \mathbf{d}_{\text{obs}})\|_2^2 \tag{1.11}$$

where $\mathbf{W}_d$ is a diagonal matrix containing the reciprocal of data error standard deviations, $\mathbf{d}_{\text{pred}}$ is the predicted data computed from the forward operator $F(\mathbf{m})$, the observation data is given by $\mathbf{d}_{\text{obs}}$ and $\| \ \|_2^2$ is the squared ℓ^2 norm. The default model regularization term is given by

$$\phi_m(\mathbf{m}) = \alpha_s||\mathbf{W}_s(\mathbf{m}-\mathbf{m}_0)||_2^2 + \alpha_x||\mathbf{W}_x(\mathbf{m})||_2^2 + \alpha_y||\mathbf{W}_y(\mathbf{m})||_2^2 + \alpha_z||\mathbf{W}_z(\mathbf{m})||_2^2 \tag{1.12}$$

where the α values are user-defined weights that control the proximity of the model $\mathbf{m}$ to a reference model $\mathbf{m_0}$ and the overall smoothness of $\mathbf{m}$. Diagonal weighting matrices $\mathbf{W}$ act on particular model cells or cell boundaries and can be used to incorporate a priori information into the inversion process. In Equation 1.12, $\mathbf{m}_0$ may also be included in the $\mathbf{W}(\mathbf{m})$ terms as $\mathbf{W}(\mathbf{m}-\mathbf{m}_0)$ if desired. Although ℓ^2 norms are common in the model regularization, ℓ^1 and approximations to ℓ^0 type norms can be used as well to encourage compactness (Ekblom, 1973; Fournier, 2015; Last and Kubik, 1983; Portniaguine and Zhdanov, 1999). The optimization problem is solved with an iterative Gauss-Newton approach, and the minimization of the objective function at the $(i+1)^{th}$ Gauss-Newton iteration requires the solution of

$$(\mathbf{J}^T\mathbf{W}_d^T\mathbf{W}_d\mathbf{J} + \beta\mathbf{R}_m)\delta\mathbf{m} = -\mathbf{J}^T\mathbf{W}_d^T\mathbf{W}_d(\mathbf{d}_{\text{pred}}^{(i)} - \mathbf{d}_{\text{obs}}) - \beta\mathbf{R}_m(\mathbf{m}^{(i)} - \mathbf{m}_0) \tag{1.13}$$

where $\mathbf{J}$ is a Jacobian matrix of sensitivities, $\mathbf{R}_m$ is a regularization term composed of $\mathbf{W}_s$, $\mathbf{W}_x$, $\mathbf{W}_y$ and $\mathbf{W}_z$ matrices and $\delta\mathbf{m}$ is a model perturbation vector. The inversion model is updated through Equation 1.13 until a suitable step can no longer be found or the target data misfit has been reached. In this thesis, the data misfit will be normalized by the number of data points, meaning the target data misfit will always be equal to unity.

1.5 Airborne Electromagnetic Interpretation Techniques

As AEM techniques have been around for decades, there have been a variety of methodologies developed to interpret and model AEM data sets, and these methods are now discussed.

1.5.1 Semi-quantitative methods

Prior to inversion, analysis of AEM data relied on semi-quantitative approaches, where approximations and simplifications to the structure of the earth are used. These techniques can produce valuable inferences and range from curve-fitting of simple geometric shapes such as vertical ribbons representing thin plates to determine the conductance of an anomaly (Palacky and West, 1973), to calculating a best-fitting apparent resistivity value at each transmitter/receiver pair (Fraser, 1978). Later on, groups started developing efficient conductivity-depth transforms for imaging anomalies at depth (Eaton, 1998; Macnae et al., 1998; Macnae and Lamontagne, 1987; Macnae et al., 1991) as well as analyzing the time-constant exponential rate of decay of the fields to gain knowledge of the conductivity and shape of the target (Macnae et al., 1998; Nabighian and Macnae, 1991). While simple and fast, semi-quantitative methods have limitations due to their simplicity and various approximations, but they paved the way for electromagnetic inversion.

1.5.2 Voxel inversion methods

AEM inversion began with 1D layered earth inversions (Constable et al., 1987; Farquharson and Oldenburg, 1993; Raiche et al., 1985), and moved to 2D (Wilson et al., 2006), before 3D voxel AEM inversions became computationally feasible (Cox et al., 2010, 2012; Haber and Schwarzbach, 2014; Oldenburg et al., 2013; Ruthotto et al., 2016; Yang et al., 2014). The term 3D voxel inversion means that the earth is discretized into cells in a 3D mesh, where the conductivity value in each cell is solved for during the inversion process. This technique, sometimes referred to as a pixel method, provides flexibility in the sense that any arbitrary anomaly shape or geologic structure that can be discretized on a mesh can be theoretically recovered by the inversion.

In a 3D AEM setting, the system of equations to solve can become excessively

large for a number of reasons. The vast area covered in an airborne survey means that a significant number of 3D mesh cells are required to discretize the expansive spatial domain. In addition, the number of source locations can easily exceed 100,000, which makes for an expensive system to solve at many source locations. To tackle these numerical obstacles, Cox et al. (2012) introduces the concept of a moving sensitivity footprint to reduce the spatial domain size of the forward problem. Alternatively, an adaptive mesh refinement can be used (Key and Weiss, 2006), where the mesh is refined in areas that require a higher numerical accuracy, while retaining a coarse solution in other areas. This approach is applied in Haber and Schwarzbach (2014), where the full spatial domain is modeled, but the problem size is reduced by using decoupled forward and inverse adaptive octree meshes, specifically for time-domain problems. Recently, Ruthotto et al. (2016) introduced the operators necessary to model the full spatial responses in both the frequency and time domain through the Julia language framework (Bezanson et al., 2012). It is worth noting that a potential drawback of the voxel approach in large surveys is that it can be difficult to accurately fit small-scale features, especially thin anomalies with high resistivity contrasts compared to the background. Strategies to address this issue will be discussed in the parametric section.

1.5.3 Cooperative and joint inversion

The inversion methodology becomes ambiguous when multiple data sets are present over a common spatial area. If individual inversions produce inconsistent models this can lead to the question of why the models are different, and which one should be used for ensuing interpretation purposes. In a cooperative inversion, a common physical property model is sought by incorporating the inversion result from one data set as a priori knowledge for another data set, either through a reference model, initial model or inversion weights (Commer and Newman, 2009; Lines et al., 1988; Oldenburg et al., 1997). A variation of the cooperative approach is the alternating direction method of multipliers (ADMM) (Wahlberg et al., 2012) where the objective function is re-written as an optimization problem with a Lagrangian multiplier and a constraint that the resistivity models from each data set must be equal. An application of ADMM to 3D hydrogeophysical inversion can be found in Steklova

and Haber (2016). These approaches differ from a joint approach, where multiple data sets are inverted simultaneously to produce one inversion model (Albouy et al., 2001; Gallardo and Meju, 2004; Oldenburg et al., 1997; Sosa et al., 2013; Vozoff and Jupp, 1975). This requires being able to forward model and compute sensitivities for all data within a single code, and it also requires proper relative assignments of uncertainties.

1.5.4 Constrained inversion

Physical property values can be extracted from drilling or surface rock samples, and represents an efficient manner to incorporate geologic knowledge into the inversion as constraints. Constrained inversions have been studied at length and the reader is advised to peruse Lelièvre and Oldenburg (2009); Lelièvre et al. (2009); Li and Oldenburg (2000); Williams et al. (2009) for a detailed account of various ways to add such information. In this thesis, geologic constraints will be added in the form of reference models and upper and lower physical property bounds when this information is available.

1.5.5 Parametric methods

Parametric inversion methods can be advantageous when prior geometric or geologic knowledge suggests that the target anomaly has a particular shape or a simplistic geometry. Parametric inversions solve for a reduced set of parameters that describe the physical property space instead of solving for the value in every mesh cell. Early parametric methods incorporated a reduced-physics approach where various assumptions and approximations to Maxwell's equations were used. A reduced-physics approach was applied to the AEM problem by Keating and Crossley (1990) where a plate parameterization in free space is assumed, by Xiong and Tripp (1995) with the software package Marco Air, where 3D prisms are placed in a layered-earth environment, and by Raiche (1998) with the package Leroi Air, where 3D plates are modeled in a layered earth setting. Currently, a commonly used reduced-physics forward modeling and inversion parametric algorithm is Maxwell EMIT (2005), where the response from one or multiple plates is calculated in free-air, in a half-space or in a layered-earth media using electrical ribbon

currents located on plate edges. Although these parametric programs are highly useful for modeling responses from simplified conductors, they contain significant numerical approximations that can create issues when dealing with multiple targets or complex geometries. One of the major contributions of this thesis is that the parametric algorithm that is introduced models the full 3D Maxwell's equations shown in Equations 1.1 and 1.2.

1.6 Thesis Outline

This thesis is composed of four main chapters, the first two have been published in peer-reviewed journals, the third is in preparation for submission and the fourth is part of ongoing research. The content is written under the common theme of developing practical cooperative and parametric strategies to improve the accuracy of 3D AEM inversion in a variety of geologic settings where conventional techniques face difficulties. Each chapter contains both synthetic and field examples to demonstrate how the approaches are both theoretically and practically viable. These novel algorithms focus on two common scenarios, and the goals of this dissertation are listed below.

1. To develop strategies to invert AEM data in 3D that spatially overlap with other electromagnetic surveys.

2. To develop methods to invert AEM data in 3D to recover thin, high contrast anomalies.

Chapter 2 focuses on the first topic where I propose a cooperative methodology for incorporating multiple electromagnetic data sets over a common area. In Chapter 3 I look at the second goal where I introduce a new parametric method of inverting AEM data for narrow, highly conductive targets. In Chapter 4 I expand the method from Chapter 3 to allow for multiple anomalies, making the approach suitable for a larger range of geologic scenarios. Finally in Chapter 5 I address the situation where both topics apply, and here I modify the cooperative strategy from Chapter 2 to incorporate both parametric and voxel based inversion algorithms.

Collectively, my specific contribution to science includes:

1. Presenting a new cooperative algorithm for spatially overlapping electromagnetic data sets that is also general for other types of geophysical data.

2. Developing the first parametric algorithm for airborne electromagnetics that models the full 3D Maxwell equations.

3. Introducing the first parametric hybrid inversion for geophysical applications where smooth features are incorporated along with compact parametric anomalies within one framework.

Chapter 2

Cooperative Inversion of Multiple Electromagnetic Data Sets

In this chapter, I develop a cooperative methodology for inverting AEM data that spatially overlaps with other electromagnetic surveys. The approach produces a consistent 3D resistivity model with improved resolution compared to inverting each data set independently, and adheres to geologic knowledge from borehole measurements through bound constraints. Synthetic and field data from the Antonio gold deposit in Peru are used to demonstrate the benefits of this technique.

2.1 Introduction

Conventionally, an individual AEM survey is inverted to create a single resistivity inversion model; however, when multiple spatially overlapping surveys, possibly from different time periods, produce inconsistent inversion models, this can lead to difficulties in interpretation. These model discrepancies suggest that a joint or cooperative approach, where one consistent inversion model is sought, could be beneficial.

The advantage of a cooperative approach is that individual algorithms, tailored to inverting a particular data type, can be used. This is beneficial because carrying out inversions of multiple data sets individually is generally much faster than inverting them simultaneously. Cooperative inversion is also less sensitive to prob-

lematic or noisy measurements compared to joint inversion. Erroneous data within the entire suite of observations can cause a joint inversion and to a lesser degree a cooperative approach to proceed very slowly or to stall, and may produce unwanted artifacts in the final model. By breaking up the inversion into small steps using one single data set at a time, as in the cooperative approach, the inversion has an easier time finding a suitable model update step. In a joint inversion this computed step is based on all data sets, each with a different noise signature, and can be more problematic to obtain.

There are numerous ways to implement a cooperative inversion through the use of reference models, constraints, or weightings in the regularization term of the objective function (Commer and Newman, 2009; Lines et al., 1988; Oldenburg et al., 1997). However, there is also the question of whether one such consistent model exists due to the presence of induced-polarization effects or a frequency-dependent conductivity. Therefore, a cooperative inversion needs a set methodology or work flow to address specific issues in implementation. In this chapter, time-domain AEM data are cooperatively inverted with a joint CSAMT and DC resistivity data set. Here, the DC data are modeled as a very low frequency EM survey in order to model simultaneously with the CSAMT data in a generalized frequency-domain inversion code. This chapter focuses on three primary research objectives.

- To develop a cooperative inversion method for AEM data that spatially overlap with other geophysical EM data sets.
- To prove, with a synthetic example, that a cooperative method increases the accuracy of the resulting 3D resistivity model.
- To apply a cooperative approach to field data to produce a consistent inversion model where additional geologic interpretations can be established.

Three spatially overlapping data sets are first introduced over the Antonio high-sulfidation epithermal gold deposit: time-domain AEM, CSAMT, and DC resistivity. As an initial step, each survey is inverted individually in 3D to estimate a resistivity structure sensitive to that particular survey. Similarities and differences in the resulting models are then noted. The inversion results coupled with geological insights regarding the deposit are subsequently used to construct a synthetic model

that emulates, as close as possible, the Antonio deposit. Simulated data sets, using field measurement locations, are computed over the synthetic model. Synthetic data are inverted individually to ascertain whether differences again occur between resulting models. At this point, a cooperative approach is applied, which aims to improve the accuracy of the synthetic inversion model in a qualitative and quantitative sense. This cooperative work flow is then applied to the Antonio field data. A constrained cooperative inversion follows where bound constraints from boreholes measurements are used, which yields a consistent final model from which geologic interpretations can be made.

Figure 2.1: Map of Peru with location of Antonio deposit marked as a black star. Modified from McMillan and Oldenburg (2014).

2.2 Antonio Geologic Background

The Antonio gold deposit is located in the Andes mountains of Northern Peru, as shown in Figure 2.1, and resides within the larger Yanacocha high-sulfidation epithermal gold system. Newmont Mining Corporation owns the majority of this active mining and exploration project. The region experienced pervasive hydrothermal alteration to form a zone of massive silicic alteration in the innermost zone, flanked by alunite, pyrophyllite, kaolinite and montmorillonite assemblages with an outermost halo of propylitic alteration (Teal and Benavides, 2010). This alteration zonation is characteristic of high-sulfidation deposits (Arribas, 1995). Fig-

ure 2.2 shows a regional view of the alteration zones at Yanacocha, and the corresponding relationship between high grade gold deposits in black and silica alteration in red.

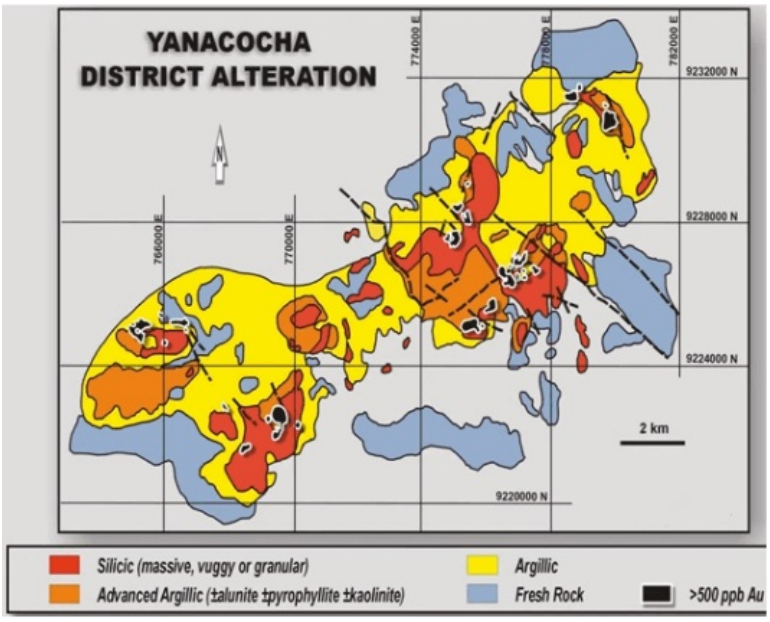

Figure 2.2: Yanacocha regional alteration map with location of major gold deposits. (modified from Hoschke (2011)).

It is clear that the bulk of the gold mineralization resides within or near massive silica, vuggy silica and granular silica units. The resistive nature of silica alteration compared to the relatively conductive background makes it an applicable target for EM surveys (Goldie, 2000; Hoschke, 2011; Oldenburg et al., 2005). These quartz-rich areas of metasomatism are often found near faults where confined fluid flow occurred (Teal and Benavides, 2010). Furthermore, the intersection of faults, often conductive in nature, where hydrothermal breccias broke through overlaying volcanic units is especially prospective for gold mineralization. These structural traps within favorable pyroclastic lithologies, such as ignimbrite beneath or proximal to flow dome complexes, are typical geologic hosts to gold deposits in the region (Loayza and Reyes, 2010). Much of the surrounding clay alteration, which

is generally more conductive than silica alteration (Goldie, 2000), at Antonio has also been enriched with silica. For the sake of this study, any zone significantly enriched with quartz is referred to as silica alteration. Figure 2.3 shows a geologic map of the Antonio region with lithologies and structures marked. The primary extent of near-surface (0 - 100 m depth) silica alteration is outlined in dashed red.

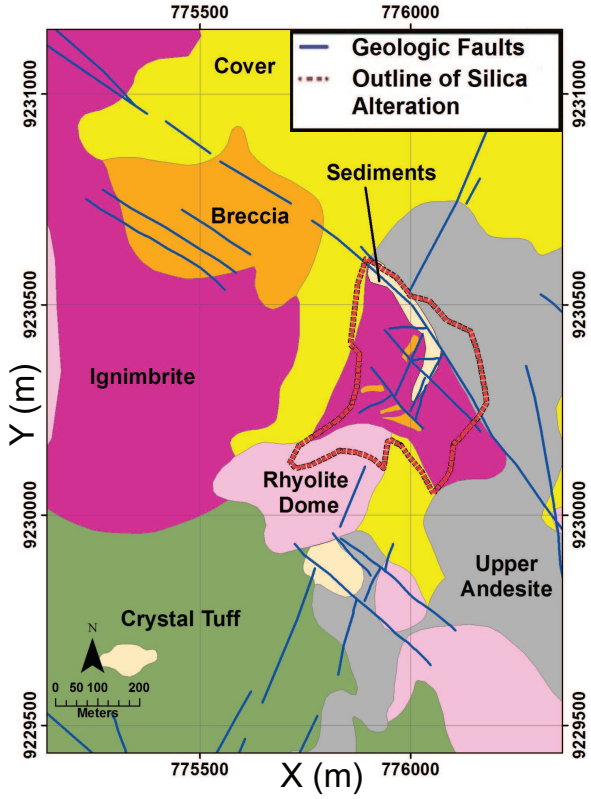

Figure 2.3: Antonio geology with lithologies, structures and near-surface silica alteration outlined.

2.3 Antonio Geophysical Data Sets

2.3.1 Time-domain AEM

In 2003, a helicopter based time-domain AEM survey was collected using the NEWTEM I system (Eaton et al., 2013). Five East-West lines over the Antonio deposit, extracted from the larger airborne survey, are analyzed in this chapter. The peak current of the transmitter was 245 A, with a transmitter loop area of 289 m^2. z-component responses ($\frac{\partial \mathbf{b}_z}{\partial t}$), measured out to 6.35 ms after current shut-off were recorded every 20 m with a line spacing of 200 m for a total of 268 transmitter positions. Time channels from 30 μs to 2000 μs are used for analysis, and the discretized waveform is shown in Figure 2.4 with logarithmically spaced time channels plotted for reference. The waveform closely approximates a square wave, which is advantageous for near-surface mapping of weakly conductive or resistive targets (Allard, 2007). Smaller discretized time steps are taken near the first recorded time channel for numerical accuracy purposes (Haber and Schwarzbach, 2014). Due to mountainous terrain, the drape of the transmitter above the ground varied from 32 m to 146 m, with a mean value of 62 m. Exact system locations are shown as orange circles in Figure 2.5.

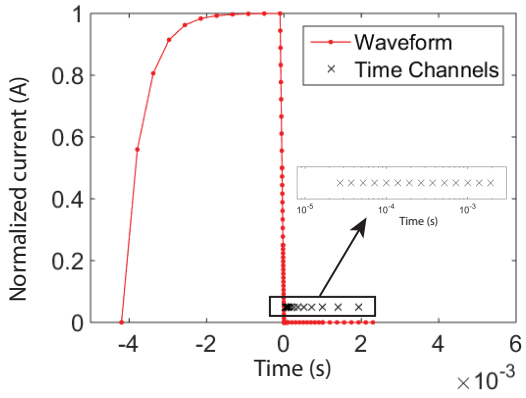

Figure 2.4: NEWTEM-I discretized waveform in red with measured time channels marked as black crosses.

2.3.2 CSAMT

In 2003, an asynchronous scalar CSAMT (Zonge and Hughes, 1991) survey was acquired by Quantec Geoscience with a total of five East-West (EW) and eight North-South (NS) lines over the Antonio deposit. Two transmitters: an EW oriented transmitter 6.2 km to the south, and a NS oriented transmitter 5.9 km to the east provided the source for EW and NS lines respectively. Having transmitters with orthogonal orientations permitted the earth to be energized from two directions. Line spacings varied between 150 m and 200 m, and stations were spread 50 m apart. In-line electric field, and orthogonal magnetic field measurements from 11 frequencies ranging between 2 Hz and 2048 Hz are used in this study. Receiver locations are shown as red stars in Figure 2.5.

2.3.3 DC resistivity

In 1998, a conventional in-line time-domain pole-dipole DC resistivity survey was acquired with five EW lines spread 150 m to 200 m apart with 50 m spaced dipoles, and a transmitter/receiver separation (N spacing) of 1 to 6. In 2004, one additional line of 150 m spaced dipoles situated 50 m south of the previous survey was collected. Receiver locations are shown as green triangles in Figure 2.5. Examples of field data from each survey can be seen in Figure 2.6.

2.4 Inversion Methods

2.4.1 Inversion preparation

Prior to inverting field data, initial steps such as quality control of the data, preparing suitable meshes, and assigning appropriate uncertainty values, need to be completed, as well as removing field data below an estimated noise threshold. Even though inversions are carried out separately in a cooperative inversion, it is desirable to have a common mesh so that difficulties in transferring results from one mesh to another are avoided. Here, because there are frequency and time-domain surveys, the design of the mesh is based on diffusion distance and skin depth (Nabighian and Macnae, 1991; Ward and Hohmann, 1988) shown in Equations 1.7 and 1.8.

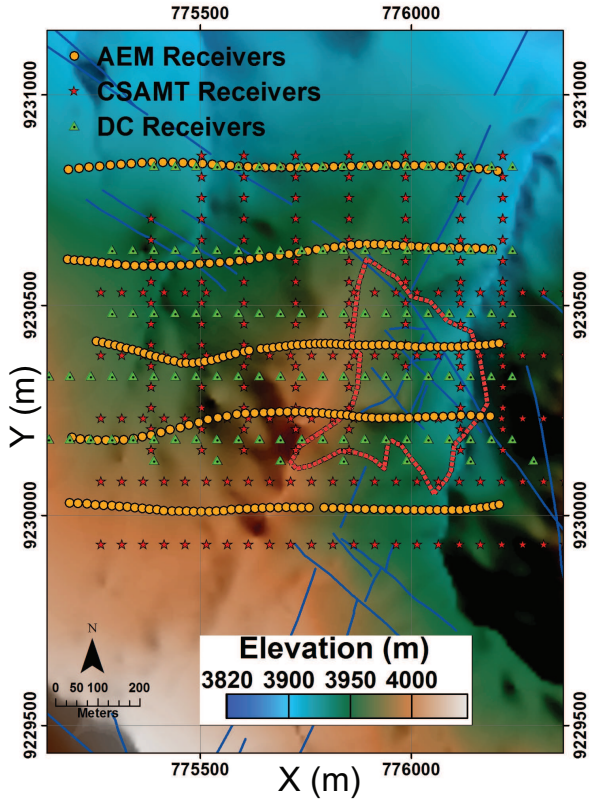

Figure 2.5: Antonio geophysics locations. Receiver sites for AEM (orange circles), CSAMT (red stars), and DC Resistivity (green triangles) overlaid on topography with near-surface silica alteration outlined in dashed red and geologic faults in thin blue.

In order to minimize numerical accuracy issues, mesh creation in this chapter and throughout the thesis adheres to the guidelines below, which are based on experience working with EM inversion codes. Additionally, when significant topography, such as at Antonio, is present, the topography discretization error must be taken into consideration when determining a finest mesh cell size.

- The mesh contains padding cells extending to a minimum of twice the largest diffusion distance, or twice the largest skin depth. For a 50 Ωm half-space

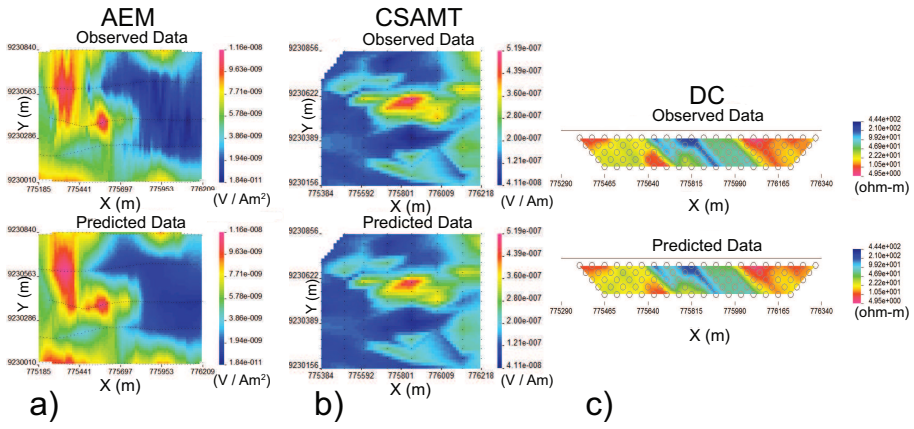

Figure 2.6: Observed and predicted field data from individual inversions. a) AEM plan view of $\frac{\partial \mathbf{b}_z}{\partial t}$ at 139 μs b) CSAMT plan view of y-component electric field amplitudes at 16 Hz c) DC apparent resistivity pseudo-section from line 9230630.

this equates to roughly four kilometers of padding around the core area of interest for AEM, and five kilometers of padding around the CSAMT receivers.

- The smallest cell size in the mesh is at most half the minimum diffusion distance or minimum skin depth. For a 50 Ωm half-space this produces a minimum cell size of 24 m and 40 m for AEM and CSAMT respectively.

In an inversion, there is always a trade-off between accuracy and total size of the mesh. Using the above guidelines, the final mesh is designed to be suitable for all three surveys, and contains core cell sizes of 25 m $\times$ 50 m $\times$ 25 m in x, y, z. To accommodate CSAMT transmitters far away from the receiver area without greatly increasing the number of total cells, an adaptive ocTree mesh is used (Haber et al., 2007a) with a total number of inversion mesh cells of 86,942. For AEM inversions, forward and inverse meshes are decoupled for maximum efficiency as described in Haber and Schwarzbach (2014), and these forward meshes have roughly 10,000 cells per mesh.

The next task is to assign uncertainties to the data. The assigned error uncer-

tainty is made up of a percentage and a floor value. Percentages range between 10% and 15%, depending on the noisiness of the data, and noise floors are selected as shown in Table 2.2.

2.4.2 Inversion methodology

AEM, CSAMT and DC 3D inversions follow algorithms outlined in (Haber et al., 2004; Haber and Schwarzbach, 2014; Oldenburg and Li, 1994). In this chapter, three Gauss-Newton iterations are computed for each trade-off value of β, known collectively as one β iteration, and the inversion terminates when the data misfit reaches its target level ϕ_d^* of unity.

2.4.3 Individual Antonio inversions

3D inversions for all individual field data sets are performed, and examples of predicted data results are shown in Figure 2.6. Resistivity plan maps at a constant elevation of 3870 m above sea-level through the resulting models are shown in Figure 2.7 with a consistent color scale. Due to rolling topography, a constant elevation slice of 3870 m corresponds to an average depth below surface of roughly 75 m, although it ranges from 10 m to 150 m throughout the survey area. Additional constant elevations slices at 3895 m, 3845 m, 3820 m, and 3795 m are displayed in Figure 2.16. These inversions are unconstrained, and use a 50 Ωm half-space reference model. Details about uncertainty assignments and final data misfits are summarized in Table 2.1. Geologic faults and the outline of known near-surface silica alteration are plotted for reference. Figure 2.7a shows a slice through the 3D AEM inversion model along with data locations, and the result recovers a large uniform resistor in the center of the survey area. This anomaly agrees well with the known resistive silica alteration outline and past studies (Oldenburg et al., 2005, 2004), although the resistor extends beyond the known outline to the north-west for approximately 200 m.

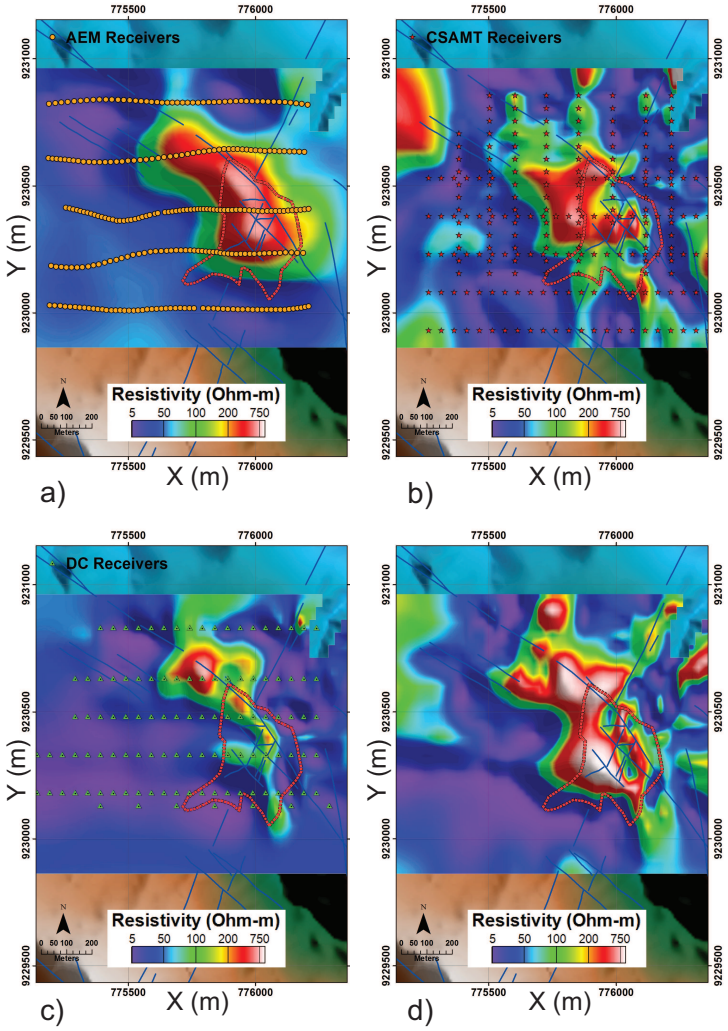

Figure 2.7: Resistivity 3D inversions from field data at a 3870 m elevation slice with receiver locations shown. Near-surface silica alteration outline in dashed red and geologic faults in thin solid blue. a) AEM b) CSAMT c) DC Resistivity d) Cooperative.

Table 2.1: Error assignments and final data misfits for individual field and synthetic inversions.

Data Set	**Error** (%)	**Error** (floor)	**Final** ϕ_d
Field			
AEM	15	4.2×10^{-10} V/Am^2	0.98
CSAMT	10	3.5×10^{-8} V/m (**E**)	0.96
		2.7×10^{-8} A/m (**H**)	
DC	10	0.5 mV	0.91
Synthetic			
AEM	10	4.2×10^{-10} V/Am^2	1.00
CSAMT	10	1.0×10^{-9} V/m (**E**)	0.52
		1.0×10^{-9} A/m (**H**)	
DC	10	1.5 mV	0.72

Figure 2.7b portrays a 3870 m constant elevation slice through the 3D CSAMT inversion result along with receiver locations. Due to the asynchronous nature of the CSAMT survey, meaning the transmitter and receiver clocks are not synchronized, only the amplitude and not the phase of the electric and magnetic fields are inverted. The imaged resistor has some similarity to that from the AEM inversion, but it deviates more from the known silica alteration outline. Although the recovered resistivity magnitudes compare well with that from AEM, the center of the CSAMT anomaly is shifted to the west, and the resistor extends 100 m to 200 m west of the mapped alteration zone. The CSAMT anomaly is broken up into multiple pieces, unlike the cohesive AEM image, and some small conductive areas occur within the resistive region. There is also a spurious anomaly in the extreme north-west corner of Figure 2.7b, which is outside the data supported region and should be ignored.

The inversion of DC potential differences is shown as a 3870 m constant elevation slice in Figure 2.7c, along with receiver electrode locations. The recovered model exhibits a similar curved north-northwest trending resistivity feature as the AEM survey, although the strongest resistor occurs outside the dashed outline to the north-west. Within the known alteration zone, much of the area is modeled as conductive, although there is a thin resistive feature that extends down through the marked anomaly to the south-east portion of the survey. Resistivity magnitudes are generally weaker compared to AEM and CSAMT results, and the overall shape is narrower and smaller compared to the other two models.

2.4.4 Cooperative inversion work flow

Discrepancies between individual field inversion results suggest that joint and/or cooperative methods are warranted to produce one resistivity model that fits all the data sets. Intrinsically this may be challenging. Each survey has its own noise signature, and the geometric layout of transmitters and receivers may be sensitive to different portions of the earth. In addition the process of homogenization, or representing micro-scale features in the earth as a homogeneous physical property value within a mesh cell, may not yield equivalent results across all electromagnetic techniques (Caudillo-Mata et al., 2016). Hence, each survey will not neces-

sarily image the ground in the same manner. Furthermore, induced-polarization effects, anisotropy, data quality variations, acquisition location differences, modeling errors, and different source types (galvanic vs. inductive) can all potentially complicate results. That being said, at Antonio, the frequency-dependent nature of conductivity within sulfides is thought to be minimal and there is no reason to believe that anisotropy is a major factor. Galvanic and inductive sources will image the ground in unique ways, but it is postulated that the combined information from these data sets will be beneficial for inversion accuracy instead of detrimental. Therefore, it is assumed that producing a consistent isotropic resistivity model is possible, while the mesh generation guidelines above should minimize modeling errors. First, the AEM data is cooperatively inverted with a joint CSAMT/DC data set. In this joint CSAMT/DC data set, DC voltages are converted into electric fields, and then treated as a 0.125 Hz frequency input in the CSAMT data. This frequency is sufficiently low that there are no inductive effects observed in the simulated data.

The cooperative work flow developed is proposed in Figure 2.8. Starting with an initial model σ_0, the first task is to calculate a model update from data set d_1 using a starting beta, $\beta_1^{(1)}$, where the subscript refers to data set (d_1), and the superscript in parenthesis refers to the cooperative iteration number. The Gauss-Newton system is solved multiple times for a given β, known as an inner iteration, to produce a revised model $\sigma_1^{(1)}$. This updated model becomes the initial and reference model for the first cooperative iteration for data set d_2, and the output is $\sigma_2^{(1)}$. Subsequently, the process repeats and $\sigma_2^{(1)}$ becomes the initial and reference model for a second cooperative iteration. The values of β for this next, and future, iterations are reduced according to a schedule $\beta_1^{(i+1)} = \gamma\beta_1^{(i)}$ and $\beta_2^{(i+1)} = \gamma\beta_2^{(i)}$, where $\gamma \leq 1$. For the work here $\gamma = 0.2$, which is an aggressive β reduction scheme; however, experience with the code suggests that solving the Gauss-Newton system multiple times per β makes this a feasible approach.

This cooperative work flow continues up to a maximum number of iterations $i_{\max}$, until the target misfit is reached for one or both data sets or until a suitable step that reduces the data misfit can no longer be found. If a single model hits both target misfits, ϕ_{d1}^* for d_1 and ϕ_{d2}^* for d_2, each data set has been adequately fit and the process stops.

If only one data set is fit, i.e. d_1, then the emphasis shifts to continued Gauss-Newton iterations for d_2. If the output model $\sigma_2^{(i)}$ is still compatible with d_1 but still not satisfactory for d_2, then further iterations are performed with d_2. After additional work with d_2, if the misfit for d_1 is significantly increased, then the cooperative inversion cycle resumes with d_1 starting with the last used β_1^i. At this point, if the misfit for d_2 no longer decreases, the current model is accepted as the final result. The strategy is automated and requires only a few user parameters.

2.5 Synthetic Inversion Results

2.5.1 Individual synthetic inversions

In synthetic modeling, a geophysical data set is computed over a pre-defined resistivity distribution, noise is then added to simulate errors encountered in field data and this noisy synthetic data set is inverted in an attempt to recover the original model. The synthetic model in this section is designed to encapsulate the primary features of the Antonio area. It includes a 225 m thick 1000 Ωm resistor placed in a uniform 50 Ωm background. Two conductive 10 Ωm blocks with dimensions of 100 m $\times$ 150 m $\times$ 100 m are embedded. The northern conductive block is buried 75 m below the surface while the southern block is exposed at the surface. Topography for the Antonio area is used for the synthetic study. Figure 2.9 shows a 3870 m constant elevation slice through this synthetic model. Additional elevation slices, are shown in Figure 2.13a.

Forward modeling of AEM, CSAMT and DC surveys is carried out by keeping data locations and other specifications equivalent to those of the field setups. 10% Gaussian noise is added to the measurements prior to inversion. Error assignments and final data misfit values are summarized in Table 2.1. Constant elevation slices at 3870 m through the resulting inversions are shown in Figure 2.10, with additional elevation slices presented in Figure 2.13. The images all display a resistive body centered in the correct location, but the extent of the resistor, and the ability to detect the conductive blocks varies between the three models. In Figure 2.10a, the AEM inversion is able to image the outline of the resistor, but is not able to detect either of the two conductive bodies. Figure 2.10b shows the CSAMT inversion

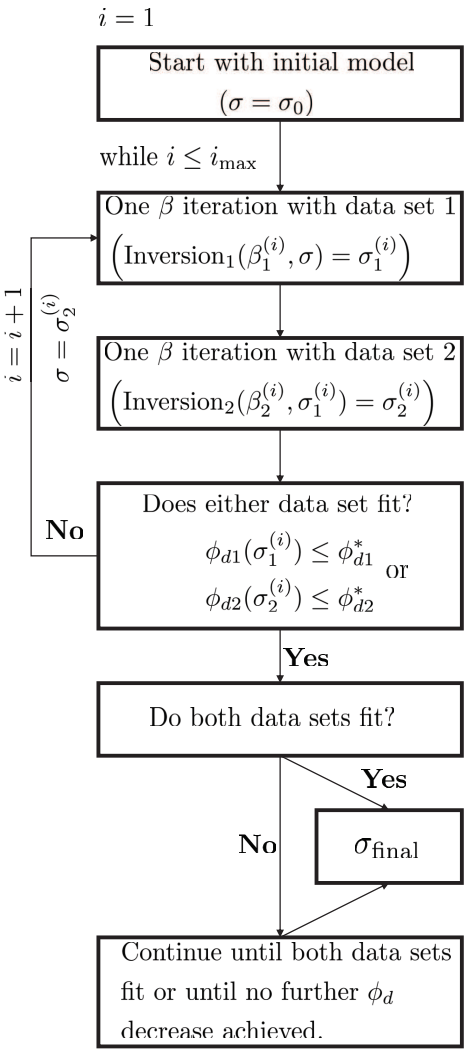

Figure 2.8: Cooperative inversion work flow. $\sigma_j^{(i)}$ = conductivity model from the i^{th} cooperative iteration for data set j, β = trade-off parameter, ϕ_d = data misfit, ϕ_d^* = target data misfit.

recovery. The result accurately images the overall resistor geometry, while clearly detecting the southern conductor, and faintly identifying the northern anomaly. For CSAMT data, real and imaginary electric and magnetic fields are inverted instead of amplitude-only data as in the field example, and this produces twice the number of data points. As field components (real and imaginary) represent a typical data set collected by industry, these are used to showcase the maximum improvement that can be obtained with the cooperative inversion. Experience has also shown that using field components can sometimes be better at recovering the true resistivity structure compared to amplitude data only. Numerical computations are also easier with field components as the equations are more linear compared to using amplitudes and phases, and this reduces the chance of being stuck in a local minimum during optimization. Error floors for synthetic CSAMT data are also set considerably lower to prevent dramatic under fitting of the data. The DC inversion result is displayed in Figure 2.10c, which depicts the overall geometry of the resistor and the southern conductive block. Resistivity magnitudes are closer to those in the synthetic model compared to the CSAMT and AEM results; however, the northern block is not seen. The three inversions have each produced valuable information, but significant differences exist in the models. At this point, the cooperative work flow is tested on these data sets in the hopes of establishing a common resistivity model.

2.5.2 Synthetic cooperative inversion

The cooperative work flow from Figure 2.8 is applied to the synthetic data sets. A common mesh is used for all inversions, and previous error assignments are kept from the individual synthetic inversions with the addition of an error floor of 3.0×10^{-5} V/m for electric fields at 0.125 Hz converted from DC voltages. A convergence curve documenting the data misfit progression for each data set is plotted in Figure 2.11, and summarized in Table 2.2. For each cooperative iteration there are a maximum of four data misfit evaluations, representing the initial data misfit, and the resulting misfit after each of the three inner iterations. It can be seen on Figure 2.11a that the joint CSAMT/DC data, pictured as red x's, hits the target misfit, shown by a black dashed line, on the third cooperative iteration. On the fourth co-

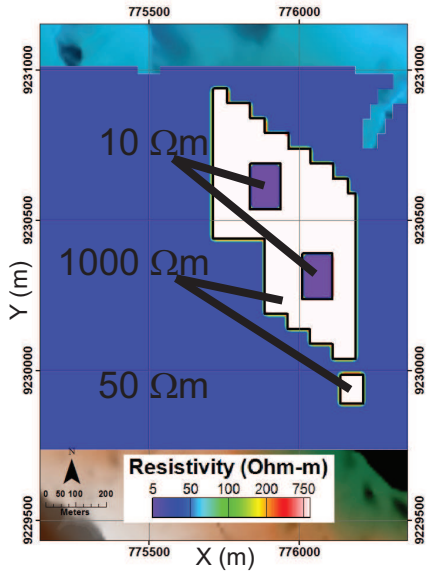

Figure 2.9: Synthetic model resistivity at a 3870 m elevation slice.

operative iteration, the initial data misfit for the joint data set is still below the target level, and thus no additional model update is performed. Eventually the process is stopped after iteration 7, because the AEM data misfit increases compared to that in iteration 6, indicating the inversion is trending in the wrong direction. Therefore, the model after iteration 6 of the AEM inversion is chosen as the final result. At that point, the CSAMT/DC and AEM final data misfits are very close to their desired target misfits. Figure 2.10d shows a 3870 m constant elevation slice through this sequential synthetic inversion model. The resistor magnitude and shape is defined more uniformly compared to the individual inversions, and the northern conductor is now better detected. The southern conductor is still clearly defined, although not as strongly as in the individual CSAMT or DC inversion. Although the AEM individual inversion does little to resolve the two conductive targets, it contributes to the cooperative inversion by helping to define the main resistive target. As AEM is an induction method, it should be sensitive to conductive targets; however, the northern conductor is buried, which masks the signal. Furthermore, the flight lines

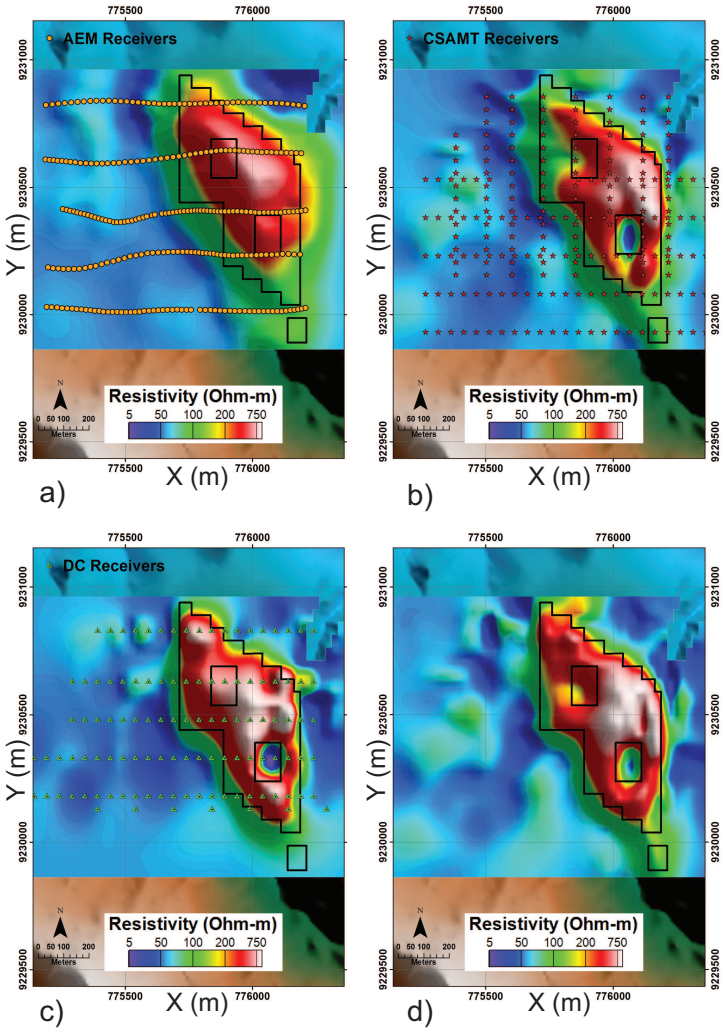

Figure 2.10: Resistivity 3D inversions from synthetic data at a 3870 m elevation slice with receiver locations shown. True resistor outline in black. a) AEM b) CSAMT c) DC Resistivity d) Cooperative.

Table 2.2: Final data misfits for cooperative synthetic and field inversions.

Inversion Method	**Data Set**	**Final ϕ_d**
Synthetic Cooperative	AEM	1.01
	CSAMT/DC	1.02
Field Cooperative	AEM	1.62
	CSAMT/DC	1.15
Synthetic Constrained Cooperative	AEM	1.00
	CSAMT/DC	1.00
Field Constrained Cooperative	AEM	1.29
	CSAMT/DC	1.15

do not directly pass over the southern conductor. In a resistive setting, the signal level is also smaller, and the conductive responses may be washed out by the Gaussian noise added, and by the relatively high uncertainty assignments.

Visual interrogation of the models shows that the cooperative result is better than any of the individual inversions. In an attempt to quantify this numerically, a region of the model is extracted that consists of the resistor and its included conductive blocks. The recovered models are numerically evaluated to determine how close they are to the true model using a residual (R) as the metric of choice as shown in Equation 2.1.

$$\mathrm{R} = \frac{1}{N}\|\log_{10}(\mathbf{m}) - \log_{10}(\mathbf{m}_{\text{true}})\|_2^2 \tag{2.1}$$

where $\mathbf{m}$ and $\mathbf{m}_{\text{true}}$ are the recovered and true resistivity model values respectively, and N is the number of cells in the volume of interest. A lower value of R refers to a smaller deviation from the true model, and hence a more accurate recovery. The residuals corresponding to the individual and cooperative inversions, and also the residual from the starting model, a 50 Ωm half-space, are shown in Table 2.3. The cooperative inversion performs the best, followed closely by the DC result, while the CSAMT and AEM models fare increasingly worse. As expected, all four inversions recover a more accurate model compared to a uniform 50 Ωm half-space. This synthetic example demonstrates that a cooperative method improves the accuracy of the recovered anomalies. Because of its close association with the

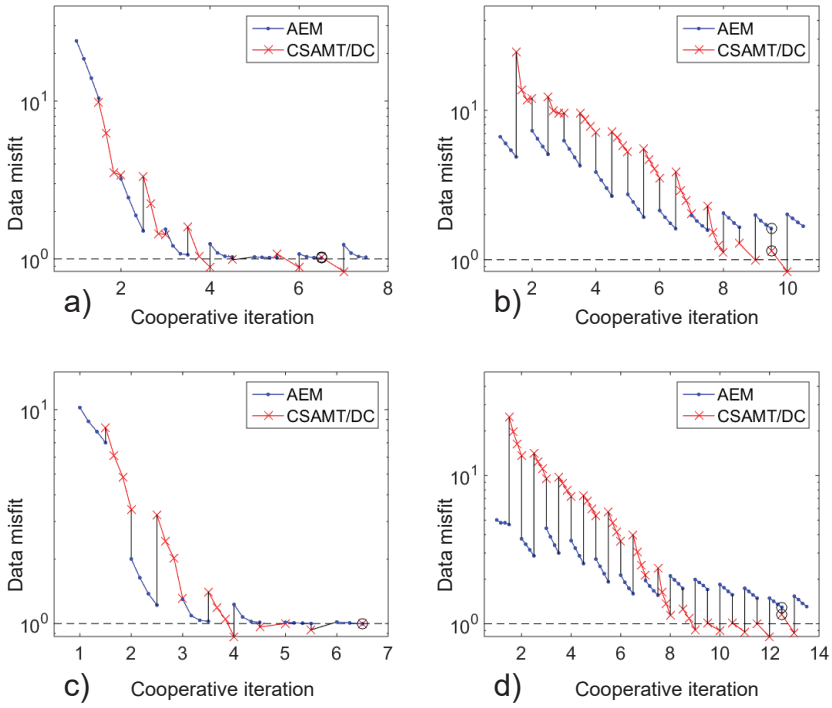

Figure 2.11: Data misfit convergence curves with target misfit shown in dashed black with final models circled in black. a) Synthetic data without bounds b) Field data without bounds c) Synthetic data with bounds d) Field data with bounds.

field data example, the same conclusions are anticipated there.

2.5.3 Synthetic constrained cooperative inversion

Thus far, all inversions have been unconstrained, and all start with a 50 Ωm half-space initial and reference model. To test a constrained approach, the synthetic example is revisited. Constraints are extracted from drilling information from 78 synthetic boreholes which are replicas of the field boreholes over the Antonio deposit. Each hole intersects multiple discretized cells in the synthetic 3D model, and this information is used to produce upper and lower resistivity bounds. The upper

Table 2.3: Quantitative assessment of synthetic inversions using a residual (R) value. A lower residual refers to a more accurate recovery.

Inversion Model	**Residual (R)**
50 Ωm half-space	1.62
AEM	0.80
CSAMT	0.66
DC	0.55
Cooperative	0.47
Bounded Cooperative	0.26

and lower bounds for each model cell intersected by a borehole are respectively set to 5% above and below the corresponding resistivity value in the synthetic model. The regularization of the inversion algorithm attempts to smooth this information away from constrained cells, and a global bound range of 1 Ωm to 5000 Ωm is applied to all cells not intersected by boreholes. This global bound prevents extreme inversion artifacts from emerging, and allows the conductivity to vary freely within this range.

The cooperative method from Figure 2.8 is implemented. The convergence plot from Figure 2.11c shows that after the third cooperative iteration, the CSAMT/DC data set reaches its target value, and after the sixth AEM cooperative iteration, both data sets reach convergence. Therefore, the addition of bounds helps guide the cooperative approach to a single solution that fits both data sets. A 3870 m constant elevation image of the constrained inversion result is shown in Figure 2.12a with additional elevation slices in Figure 2.13f. The outline of the resistor is much improved compared to previous results, and both the northern and southern conductors are clearly imaged. Even the small resistive zone at the southern tip of the survey is recovered, thanks primarily to a synthetic borehole. Quantitatively, the constrained cooperative method produces a residual value of 0.26, which outperforms all other synthetic inversions.

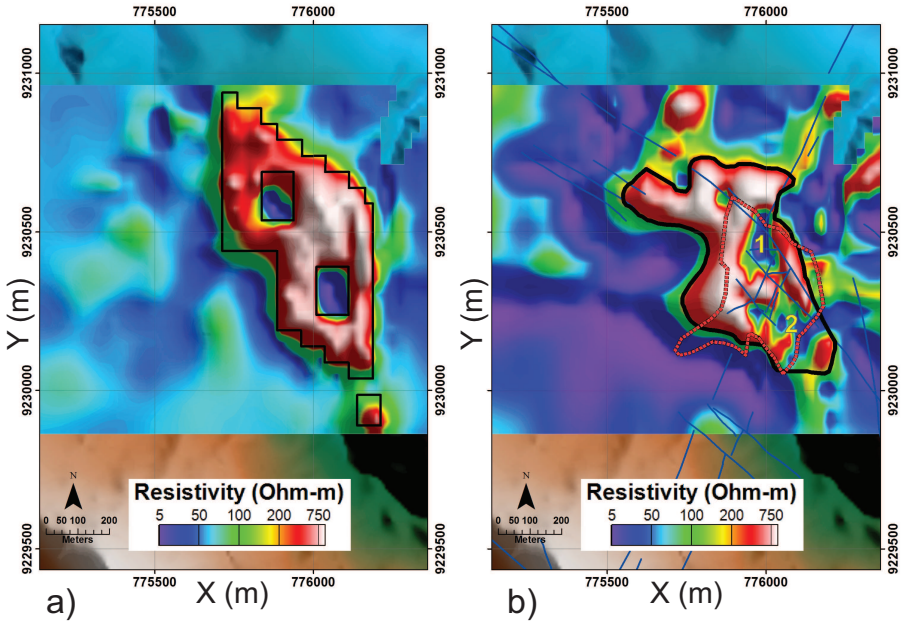

Figure 2.12: Cooperative 3D inversions with bounds at a 3870 m elevation slice a) Synthetic data with the true resistor outline in thin black b) Field data with the outline of known near-surface silica alteration in dashed red, interpreted silica alteration outline at 3870 m elevation in solid black, geologic faults in thin blue, and conductive anomalies of interest numbered in yellow.

2.6 Antonio Inversion Results

2.6.1 Antonio cooperative inversion

The cooperative approach is applied to the field data, once again using the same common mesh and error assignments as before. A noise floor of 1.0×10^{-5} V/m is placed on 0.125 Hz electric fields converted from DC data. The convergence curves are plotted in Figure 2.11b and final data misfit values are described in Table 2.2. The joint CSAMT/DC data set reaches its target level, after cooperative iteration 8, and the inversion terminates after iteration 9, when the AEM data misfit is greater than after iteration 8. The model after the eighth AEM iteration is

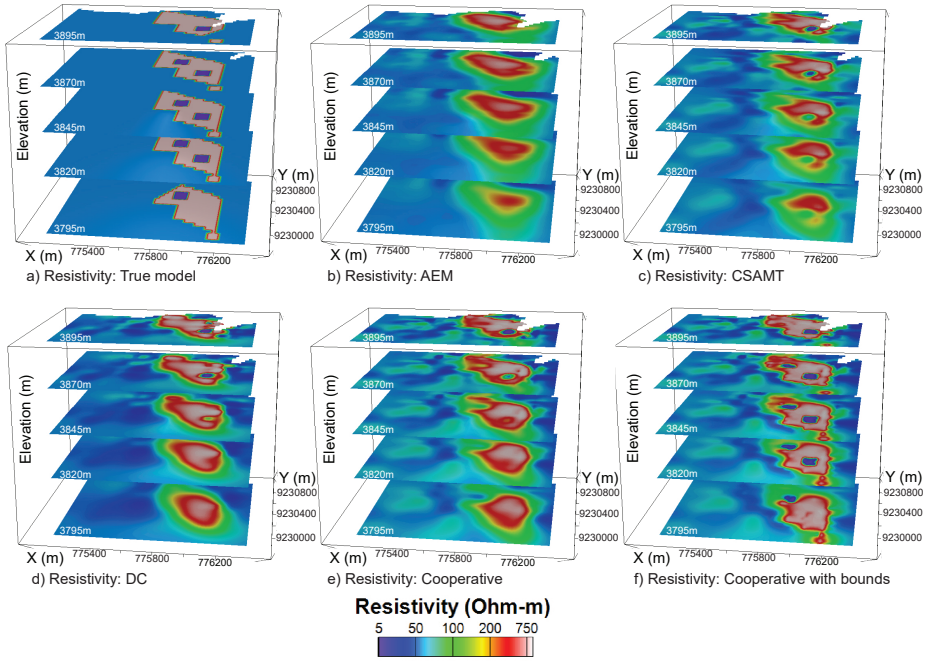

Figure 2.13: Resistivity 3D inversions from synthetic data at five elevation slices: 3895 m, 3870 m, 3845 m, 3820 m, 3795 m. a) True model b) AEM c) CSAMT d) DC Resistivity e) Cooperative f) Cooperative with drilling bounds.

chosen as the end result. The final AEM data misfit of 1.62 is above the target value of 1.0, which demonstrates that the inversion has a more difficult time fitting AEM measurements to the assigned error levels, compared to CSAMT/DC data, where the final data misfit is only slightly higher than the target value. A constant 3870 m elevation image of the result is displayed in Figure 2.7d. The recovered resistive anomaly has a better agreement with the silica alteration outline compared to the individual inversions and additional conductive features are clearly visible within the deposit region. Comparable to the synthetic case, the AEM contributes most to the cooperative result by mapping the extent of the large resistor, while the conductive features are largely due to the CSAMT/DC data. This may seem

counter intuitive at first, but the NEWTEM waveform is designed specifically to be sensitive to near-surface resistors, and the CSAMT/DC surveys have more data points directly over the well-imaged southern conductor compared to AEM measurements. The magnitude of the cooperative resistor is slightly stronger than the individual inversions, and the resistive anomaly extends past the mapped outline to the north-west. Erroneous resistive anomalies in the extreme north-west and north-east corner are beyond the data supported region, and should be neglected. As would be expected, the cooperative model is similar to all three individual images in some aspects, but not identical to any, and is interpreted to be a more accurate representation of the resistivity signature over the Antonio deposit.

2.6.2 Antonio constrained cooperative inversion

The constrained cooperative method is now applied to field data, which requires borehole resistivity information. However, boreholes at Antonio have alteration logging and geochemical assay values, but only a limited number of resistivity measurements. Surprisingly, from the samples available there is a poor correlation between alteration or rock type with resistivity; thus, another proxy for resistivity information is needed. Nelson and Van Voorhis (1983) noted an inverse relationship between total weight percent sulfide and resistivity for in-situ rock measurements in a porphyry environment. Although Antonio is a high-sulfidation deposit and not a porphyry, this concept is investigated by plotting in Figure 2.14 the total weight percent sulfur against resistivity for 30 rock samples at Antonio, colored by alteration type. The linear regression curve, represented by the black line in Figure 2.14, does not include propylitic samples, and has a resulting Pearson correlation coefficient of -0.73, indicating a statistical negative correlation. Nearly an identical relationship is extracted when resistivity is compared to total weight percent sulfide, but total sulfur content is used because more of these measurements are available.

This regression relationship is applied to the alteration values from 78 field boreholes, whose locations are shown in Figure 2.15a, and total sulfur content from 61 boreholes, displayed in Figure 2.15b. The product of the relationship is a resistivity reference model, shown in Figure 2.15c. Propylitic samples are

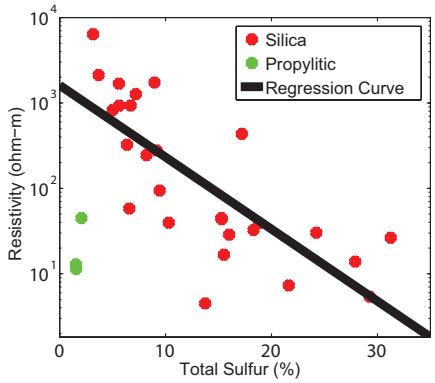

Figure 2.14: Linear regression curve, shown as a black line, for the resistivity versus total sulfur relationship from 30 borehole samples.

assigned a resistivity value of 23 Ωm in the reference model, equal to the mean of the three samples in Figure 2.15a. To create upper and lower bounds, the mean and standard deviation of the resistivity values within each model cell are calculated, and the bounds are set respectively to one standard deviation above or below the mean cell value. The incorporation of these bounds to a cooperative constrained field inversion produces the convergence curve shown in Figure 2.11d. The final target AEM misfit of 1.29 is lower than the unconstrained cooperative inversion, but still above the target level, whereas the joint CSAMT/DC final misfit of 1.15 is identical to the unconstrained case. A 3870 m constant elevation slice from this model is displayed in Figure 2.12b. This result has a strong agreement with the known silica outline, and with previous studies (Oldenburg et al., 2005, 2004), although some additional features are present, and will be discussed further in the geologic interpretation section.

Caution must be placed when implementing constraints such as upper and lower resistivity bounds, because they could erroneously bias the inversion model. Field constraints are derived from a relationship between total sulfur content and resistivity based on 30 laboratory rock measurements. This represents a small sample size from which to produce constraints for an entire model. But the validity of this relationship is corroborated by the similarity between the unconstrained and

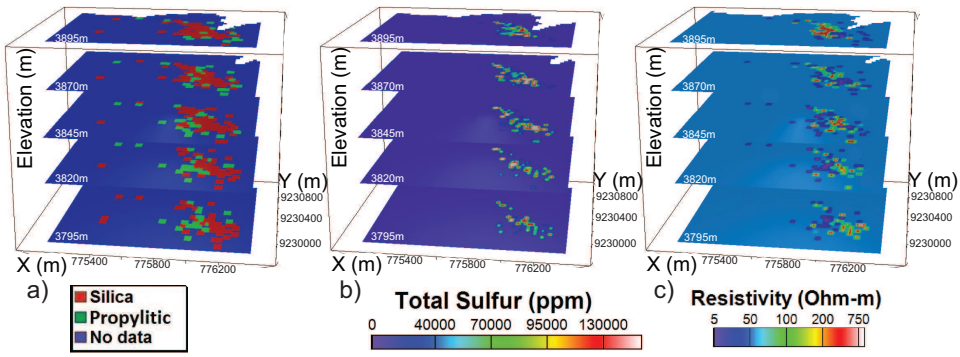

Figure 2.15: Drilling information for model cells intersected by 78 boreholes at Antonio. a) Alteration b) Total sulfur content c) Resistivity derived from a regression relationship between total sulfur/alteration and resistivity.

constrained cooperative inversions. For additional confidence in the bounds, more petro-physical measurements should be acquired, and this is recommended for future constrained cooperative studies.

2.6.3 Geologic interpretation

The constrained cooperative inversion result shown in Figure 2.12b is considered the final field inversion, and additional elevation slices are displayed in Figure 2.16f. This final result compares well with the unconstrained cooperative model in Figure 2.7d, which adds more confidence to the regression relationship that helped calculate the upper and lower resistivity bounds. In all elevation slices, the final model maps the target silica alteration zone as a strong resistor. At an elevation of 3870 m, the resistive zone extends past the mapped alteration outline to the north-west, which suggests that the silica alteration does as well. Consequently, an outline shown in solid black in Figure 2.12b represents the interpreted silica alteration zone at 3870 m elevation based on the final field inversion.

Within this resistive alteration region, small conductive areas are recovered, and two such anomalies are numbered 1 and 2 in Figure 2.12b. From borehole alteration logs, anomaly 1 represents a small area of propylitic alteration, and anomaly 2 coincides with a large total sulfur anomaly within silica alteration, which suggests

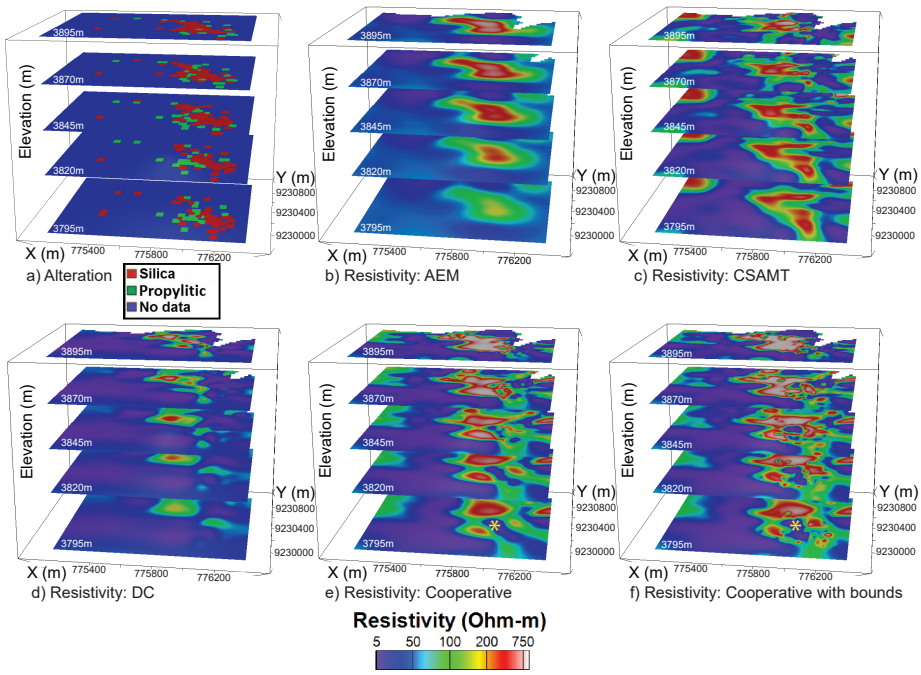

Figure 2.16: Resistivity 3D inversions from field data at five elevation slices: 3895 m, 3870 m, 3845 m, 3820 m, 3795 m. a) Alteration from boreholes b) AEM c) CSAMT d) DC Resistivity e) Cooperative. An example of a conductive anomaly potentially linked to propylitic alteration is highlighted with a yellow star f) Cooperative with drilling bounds.

extensive sulfide mineralization. This location of inferred sulfide mineralization is potentially explained by its proximity to fault intersections directly to the north and west, where fluid flow would have been confined. Anomaly 2 also sits on a chargeability high from induced-polarization data. Based on these characteristics, anomaly 2 is a prime target for gold mineralization. Borehole assays corroborate this observation with anomalous gold values present within anomaly 2 but not in anomaly 1.

At greater depths, many conductive anomalies within the confines of silica alteration can be explained by the presence of propylitic alteration. This agreement

is noted even in the unconstrained cooperative inversion where borehole constraints have not been applied. An excellent example is the large conductive zone at an elevation of 3795m as shown by yellow stars in Figures 2.16e and 2.16f. When compared to the region of propylitic alteration in Figure 2.16a there is a strong spatial correlation. Other smaller conductive anomalies within the silica-rich zone not linked to propylitic alteration may indicate the presence of sulfides, and these regions are considered prospective targets for gold mineralization.

2.7 Conclusions

The mineralization at Antonio is known to occur within areas of silica alteration, which is a resistive geophysical target. However, AEM data in addition to two other geophysical surveys over the Antonio deposit image the resistivity signature differently. The cooperative inversion method inputs all this information into one physical property model, and images the resistive zone at Antonio with a high level of agreement to the known silica alteration. This method is successful in ensuring a consistent inversion result, as demonstrated with a synthetic and field example.

Through synthetic modeling, the cooperative method is shown to improve the accuracy of 3D resistivity inversions. Moreover, adding geologic constraints to the inversion, in the form of upper and lower resistivity bounds for each 3D model cell, produces a result closer to the true synthetic model. Consequently, in a field setting, when reliable borehole physical property information exists, it should be incorporated into the 3D inversion. The final constrained cooperative field model clearly images the large silica alteration zone, and its shape is in general correspondence with drilling and previous studies of the area. An area of silica alteration from the field inversion that extends beyond the previous known outline offers a new interpretation of the mapped alteration. Further analysis from this final model highlights potential areas of sulfide and gold mineralization, within the silica alteration zone, in the form of small conductive anomalies.

Collectively this study illustrates that a practical cooperative constrained inversion methodology is possible for AEM and other electromagnetic data sets, and that exploration companies could benefit from such a technique for spatially overlapping surveys with or without borehole constraints.

Chapter 3

Single Anomaly Parametric Inversion of AEM data

In this chapter, I demonstrate a method to invert AEM data using a parametric level-set approach combined with a conventional voxel-based technique to form a parametric hybrid inversion. The approach is designed for situations where a voxel-based inversion alone may struggle, such as a conductive thin dipping plate with a large physical property contrast between itself and a highly resistive background. Synthetic and field data from the Caber volcanogenic massive sulfide deposit in Quebec, Canada, are shown to highlight the advantages of this technique. Although the approach is shown for time-domain data, the same functionality has been developed for the frequency domain and will be showcased in later chapters.

3.1 Introduction

It has been established that AEM surveys are widely used as a mineral exploration tool for imaging subsurface electrical resistivity distributions to help identify rock types, mineralization, and alteration zones (Keller, 1988). In a conventional voxel-based electromagnetic inversion, the resistivity value in every active mesh cell is solved for, and in recent years, inversion algorithms have been modified to facilitate thousands of source locations. This has resulted in numerous 3D inversion codes tailored toward AEM data (Cox et al., 2012; Haber and Schwarzbach, 2014;

Oldenburg et al., 2013; Ruthotto et al., 2016).

When an anomaly of interest has sharp boundaries and a large physical property contrast compared to the background, experience with voxel-based inversion codes suggests that accurately defining these abrupt resistivity contrasts can be challenging. Moreover, the true resistivity of the target is often poorly estimated, especially with a low resistivity or high conductivity target. One option is to use minimum or compact norm solutions for voxel-based problems to help achieve sharp anomalies (Farquharson and Oldenburg, 1998; Fournier, 2015; Last and Kubik, 1983; Portniaguine and Zhdanov, 1999; Zhdanov and Cox, 2013); however, experience has shown mixed results when applying these types of solutions to 3D AEM problems.

Another approach that will be explored further in this chapter is the parametric method (Abubakar et al., 2006; Aghasi et al., 2011). Here, instead of solving for the resistivity in every cell, only a few parameters are sought to describe the physical property space, and the reduction in the number of variables can typically be many orders of magnitude. Parametric inversions can also be coupled with such methods as level sets (Osher and Fedkiw, 2001; Osher and Sethian, 1988), to solve for the resistivity and shape of a target of interest (Aghasi et al., 2011). Level-set methods have previously been applied to 2D electromagnetic tomography and inverse scattering (Dorn and Lesselier, 2006; Dorn et al., 2000), as well as other geophysical inverse problems such as 2D travel time (Zheglova and Farquharson, 2016), 2D DC resistivity (Ascher and Roosta-khorasani, 2016; van den Doel and Ascher, 2006), 3D gravity (Isakov et al., 2011) and 3D gravity gradient data (Lu and Qian, 2015).

This research focuses on 3D AEM data, and specifically on parametric level-set inversion methods, which adds a level of stability to the inverse problem compared to traditional level-sets by restricting the shape of the anomaly; thus, acting as a form of regularization (Aghasi et al., 2011). A parametric level-set approach enables the inversion to find optimally shaped anomalies with potentially sharp boundaries and a high resistivity contrast compared to the background with a minimal number of variables. This study adds to previous hybrid modeling approaches for AEM data such as Leroi Air (Raiche, 1998), where thin sheet integral equations are used with 3D plates in a layered earth, and Marco Air (Xiong and Tripp, 1995), where volume integral equations are incorporated with 3D prisms in a lay-

ered earth.

Finding an appropriate parameterization is critical, and this work chooses to work with a skewed Gaussian ellipsoid to represent the target anomaly, although other options are available such as radial basis functions or truncated Gaussian distributions (Aghasi et al., 2011; Pidlisecky et al., 2011). The Gaussian ellipsoid shape is chosen for its flexibility, as it can easily discretize high-frequency features including plates and thin layers, as well as broader shapes such as large intrusions. It is recognized that the skewed Gaussian parameterization has limitations, especially in the single-anomaly case. Therefore, to account for additional features in the model space, a voxel-based stage is added to solve for smooth background features. The choice of parameterization is specific, but the method developed here is general to any parameterization, and could be applied to other geophysical data sets such as ground EM, potential fields or induced-polarization. The data sets presented in this section are all in the time domain, but the method has also been developed for frequency-domain observations.

The three research goals in this chapter are listed below.

- To develop a parametric inversion for AEM data with a skewed Gaussian ellipsoid parameterization.
- To show, with a synthetic and field example, that the novel parametric inversion can accurately recover a thin dipping plate; a pertinent target for mineral exploration.
- To combine parametric and voxel-based methods to form a hybrid technique that can model a single target of interest with parametric inversion, while filling in remaining features with a voxel-based code.

This chapter first discusses general electromagnetic theory before going into detail regarding the parametric hybrid methodology. Simulated AEM data over a synthetic model composed of a thin dipping conductor in a resistive half-space is then introduced to provide a means to test the code. Following the synthetic example, the hybrid inversion, which to our knowledge is the first algorithm to combine smooth and parametric features for a geophysical application, is tested on

AEM field data over a volcanogenic massive sulfide (VMS) deposit. The results are subsequently compared to previous work and to geologic knowledge from drilling.

3.2 Electromagnetic Background

This chapter focuses on AEM platforms where the receiver is contained in the center of the transmitter loop, known as coincident loop systems (Allard, 2007). The data collected are typically x, y, z component $\frac{\partial \mathbf{b}}{\partial t}$ data, although components of $\mathbf{b}$ alone can also be calculated.

For conventional voxel-based time-domain AEM inversions, the approach discussed in Haber and Schwarzbach (2014) is followed, where Gauss-Newton based optimization is used to solve quasi-static Maxwell's equations in space and time subject to boundary and initial conditions

$$\mathbf{n} \times (\nabla \times \mathbf{h}) = 0 \tag{3.1}$$

$$\mathbf{h}(x, y, z, t = 0) = \mathbf{h}_0 \tag{3.2}$$

$$\nabla \cdot \mu \mathbf{h_0} = 0 \tag{3.3}$$

using a finite-volume discretization on ocTree meshes (Haber et al., 2007a). Here $\mathbf{n}$ is a normal vector, x, y, z are spatial observation coordinates and t is time. For further information on voxel-based electromagnetic inversion theory, see Haber et al. (2004); Haber and Heldmann (2007); Haber et al. (2007b). Details regarding the parametric hybrid inversion are now discussed.

3.3 Inversion Methodology

Consider an inverse problem where the forward problem has the form

$$F(m(\mathbf{x})) + \varepsilon = \mathbf{d} \tag{3.4}$$

where F maps the function $m(\mathbf{x})$, with position vector $\mathbf{x}$, to the discrete data $\mathbf{d}$, and ε is the noise that is assumed to be Gaussian. After discretization of the model, the

discrete problem

$$F(\mathbf{m}) + \varepsilon = \mathbf{d} \tag{3.5}$$

is obtained where $\mathbf{m}$ is a discrete approximation to the function $m(\mathbf{x})$. A maximum likelihood approach would minimize the global misfit ϕ as shown in Chapter 2.

$$\min_{\mathbf{m}} \phi(\mathbf{m}) = \frac{1}{2}(F(\mathbf{m}) - \mathbf{d})^{\mathbf{T}} \mathbf{W}_d^{\mathbf{T}} \mathbf{W}_d (F(\mathbf{m}) - \mathbf{d}) \tag{3.6}$$

However, this problem is typically ill-posed, and there are many possible solutions that minimize the global misfit. To obtain a well-posed problem, two possible routes can be taken. First, if the model $\mathbf{m}$ does not have any particular form some smoothness can be assumed and this results in a regularized least-squares approach. A second option is where some specific a priori information is available, and it is assumed that the model $\mathbf{m}$, with n number of cells, can be expressed by a small number of j parameters denoted as $\mathbf{p}$. This can be expressed by

$$\mathbf{m} = f(\mathbf{p}) \tag{3.7}$$

where $f: \mathbf{R}^j \rightarrow \mathbf{R}^n$ is a known smooth function that is continuously differentiable.

In some cases both assumptions about the model are valid. The model can be made of a smooth background and an anomalous body that can be parametrized. That is

$$\mathbf{m} = \mathbf{m}_s + f(\mathbf{p}) \tag{3.8}$$

where $\mathbf{m}_s$ is some smooth background and $f(\mathbf{p})$ describes an anomalous conductive or resistive body. This leads to the following regularized problem to be solved.

$$\min_{\mathbf{m}_s, \mathbf{p}} \phi(\mathbf{m}_s, \mathbf{p}) = \frac{1}{2}(F(\mathbf{m}_s + f(\mathbf{p})) - \mathbf{d})^{\top} \mathbf{W}_d^{\mathbf{T}} \mathbf{W}_d (F(\mathbf{m}_s + f(\mathbf{p})) - \mathbf{d}) + \beta \mathbf{R}(\mathbf{m}_s) \tag{3.9}$$

Here, $\mathbf{R}(\cdot)$ is a regularization term that enforces smoothness on the background model and β is a regularization parameter. Additional restrictions, such as bounds on $\mathbf{p}$ or $\mathbf{m}_s$ can also be invoked. Equation 3.9 is a discrete optimization problem

for the smooth background model $\mathbf{m}_s$ and the parameters $\mathbf{p}$. In general, it is non-convex and therefore care must be taken to obtain feasible solutions.

A hybrid approach is proposed where a block coordinate descent (Gill et al., 1981) is used to fix $\mathbf{m}_s$ and minimize over $\mathbf{p}$ in the first, or parametric stage, and then fix $\mathbf{p}$ and minimize over $\mathbf{m}_s$ in the second, or voxel-based stage. Another option is to run the voxel-based stage first, prior to the parametric stage, but experience with the code so far suggests that the former procedure produces better results. The proposed hybrid scheme runs through each stage once, but this process could be iterated. The stopping criteria are when the inversion: a) has converged to a target data misfit of unity b) has reached a maximum number of user-defined iterations, or c) can not find a Gauss-Newton step that lowers the normalized data misfit by more than 0.1%. The program may also be terminated if the inversion is deemed to be over-fitting the data by placing obvious resistivity artifacts near transmitter or receiver locations.

This hybrid approach has the advantage of scale separation, in that the parametric inversion of $f(\mathbf{p})$ typically affects data locally, whereas optimizing over $\mathbf{m}_s$ affects data globally, and can fit large-scale and smooth features. In the first parametric stage, the method searches for one anomaly of interest, either conductive or resistive, in a background $\mathbf{m}_s$. This background can either be a uniform half-space or a heterogeneous resistivity distribution from a priori information or previous inversion work. Once again, the time-dependent quasi-static Maxwell's equations are solved with initial and boundary conditions as shown in Equations 3.1 through 3.3.

The parametric hybrid approach finds a best-fitting skewed Gaussian ellipsoid, by means of a finite-volume discretization on local and global ocTree meshes (Haber and Schwarzbach, 2014). The inversion requires an initial guess, which is composed of the quantities, r_x, r_y, r_z, ϕ_x, ϕ_y, ϕ_z, x_0, y_0, z_0, ρ_0, and ρ_1. The values r and ϕ represent an estimate for the radius and rotation angle of the ellipsoid for each Cartesian direction, while x_0, y_0 and z_0 represent the center coordinates of the anomaly, and ρ_0 and ρ_1 are the background and anomalous resistivities. Resistivity values can be fixed by the user, or alternatively, these resistivities can be set as active parameters in the inversion. The initial guesses for radii and rotation angles are multiplied together to give a transform matrix $\mathbf{T}$ as shown in Equations 3.10 to 3.14. Equation 3.15 then forms a symmetric positive definite matrix $\mathbf{M}$, com-

posed of stretching and skewing parameters m_1 through m_6, and more information regarding rotation matrices can be found in Modersitzki (2003). All unscaled parameters $\tilde{\mathbf{p}}$ are scaled by element-wise division denoted by $\oslash$ with the vector $\mathbf{s}$, to improve the conditioning of the system as seen in Equations 3.16 and 3.17. The vector $\mathbf{s}$ is composed of an appropriate length scale L, and a characteristic resistivity $\hat{\rho}$. In total, $\mathbf{p}$ contains 11 scaled parameters that are used in the parametric inversion.

$$\mathbf{S} = \begin{pmatrix} \frac{1}{r_x} & 0 & 0 \\ 0 & \frac{1}{r_y} & 0 \\ 0 & 0 & \frac{1}{r_z} \end{pmatrix} \tag{3.10}$$

$$\mathbf{R}_x = \begin{pmatrix} 1 & 0 & 0 \\ 0 & cos(\phi_x) & -sin(\phi_x) \\ 0 & sin(\phi_x) & cos(\phi_x) \end{pmatrix} \tag{3.11}$$

$$\mathbf{R}_y = \begin{pmatrix} cos(\phi_y) & 0 & sin(\phi_y) \\ 0 & 1 & 0 \\ -sin(\phi_y) & 0 & cos(\phi_y) \end{pmatrix} \tag{3.12}$$

$$\mathbf{R}_z = \begin{pmatrix} cos(\phi_z) & -sin(\phi_z) & 0 \\ sin(\phi_z) & cos(\phi_z) & 0 \\ 0 & 0 & 1 \end{pmatrix} \tag{3.13}$$

$$\mathbf{T} = \mathbf{S}\mathbf{R}_\mathbf{x}\mathbf{R}_\mathbf{y}\mathbf{R}_\mathbf{z} \tag{3.14}$$

$$\mathbf{M} = \begin{pmatrix} m_1 & m_4 & m_5 \\ m_4 & m_2 & m_6 \\ m_5 & m_6 & m_3 \end{pmatrix} = \mathbf{T}^\mathrm{T}\mathbf{T} \tag{3.15}$$

$$\tilde{\mathbf{p}} = \begin{pmatrix} m_1 \\ m_2 \\ m_3 \\ m_4 \\ m_5 \\ m_6 \\ x_0 \\ y_0 \\ z_0 \\ \log(\rho_0) \\ \log(\rho_1) \end{pmatrix} \quad \mathbf{s} = \begin{pmatrix} L^{-2} \\ L^{-2} \\ L^{-2} \\ L^{-2} \\ L^{-2} \\ L^{-2} \\ L \\ L \\ L \\ \log(\hat{\rho}) \\ \log(\hat{\rho}) \end{pmatrix} \tag{3.16}$$

$$\mathbf{p} = \tilde{\mathbf{p}} \oslash \mathbf{s}. \tag{3.17}$$

For any position x, y, z in the spatial domain Ω set

$$\mathbf{x} = \begin{pmatrix} x \\ y \\ z \end{pmatrix} \quad \mathbf{x_0} = \begin{pmatrix} x_0 \\ y_0 \\ z_0 \end{pmatrix} \tag{3.18}$$

and the level-set function τ is introduced in each mesh cell

$$\tau = c - (\mathbf{x} - \mathbf{x_0})^{\mathbf{T}} \mathbf{M} (\mathbf{x} - \mathbf{x_0}) \tag{3.19}$$

where c represents a positive constant and will be discussed in more detail later in this chapter. τ, ρ_0, and ρ_1 are used to generate the resistivity distribution through an analytic step function

$$\rho(\tau, \rho_0, \rho_1) = \rho_0 + \frac{1}{2} (1 + \tanh(a\tau)) (\rho_1 - \rho_0) \tag{3.20}$$

where

$$\lim_{\tau \to -\infty} \rho(\tau, \rho_0, \rho_1) = \rho_0$$
$$\lim_{\tau \to +\infty} \rho(\tau, \rho_0, \rho_1) = \rho_1$$
$$\rho(\tau = 0, \rho_0, \rho_1) = \frac{1}{2}(\rho_0 + \rho_1).$$

A hyperbolic tangent is chosen for the analytic step function, but other choices are possible (Tai and Chan, 2004). The transition zone between ρ_0 and ρ_1 occurs when $\tau = 0$, also known as the zero level set (Osher and Sethian, 1988), and its width is controlled by the parameter a. For numerical stability, a minimum of two mesh cells should occur within the transition zone to ensure a suitable Gauss-Newton step can be found. The optimization of the inversion follows a conventional Gauss-Newton procedure for time-domain AEM data (Haber and Schwarzbach, 2014), and a line search is used to determine an appropriate model update step within a minimum and maximum value. Other techniques such as the trust region approach introduced by Sturler and Kilmer (2011) can be applied if an acceptable step length is not found with a conventional line search, although this issue has not been encountered in this research. In the case where $\mathbf{m} = f(\mathbf{p})$ is sufficient to model the region of interest, the parametric code can be used as a stand-alone algorithm where $\mathbf{m}_s$ is fixed. Otherwise, the hybrid technique is achieved by setting the parametric inversion model as the initial and reference model when optimizing over $\mathbf{m}_s$.

3.4 Parametric Sensitivity and Initial Parameter Selection

Gauss-Newton optimization for minimizing Equation 3.9 requires a sensitivity matrix $\mathbf{J}_{i,j}$, or $\frac{\partial d_i}{\partial p_j}$, where d_i is the i^{th} data point and p_j is the j^{th} inversion parameter. For p_1 through p_9, the chain rule is used to calculate $\mathbf{J}_{i,j}$ as shown in Equation 3.21

$$\mathbf{J}_{i,j} = \sum_{\alpha,\beta} \frac{\partial d_i}{\partial \rho_\alpha} \frac{\partial \rho_\alpha}{\partial \rho_\beta} \frac{\partial \rho_\beta}{\partial \tau} \frac{\partial \tau}{\partial p_j} \tag{3.21}$$

where ρ_α is the cell center resistivity for each local mesh cell, α is the local mesh cell index, ρ_β is the cell center resistivity for each global mesh cell, and β is the global mesh cell index. This domain separation into local and global meshes is used for maximum computational efficiency as described in Haber and Schwarzbach (2014). For p_{10} and p_{11}, $\mathbf{J}_{i,j}$ is shown in Equation 3.22 where the derivative with respect to τ is replaced with a derivative with respect to ρ_0 or ρ_1

$$\mathbf{J}_{i,j} = \sum_{\alpha,\beta} \frac{\partial d_i}{\partial \rho_\alpha} \frac{\partial \rho_\alpha}{\partial \rho_\beta} \frac{\partial \rho_\beta}{\partial \rho_{0,1}} \frac{\partial \rho_{0,1}}{\partial p_j} \tag{3.22}$$

The voxel-based framework calculates the derivatives $\frac{\partial d_i}{\partial \rho_\alpha} \frac{\partial \rho_\alpha}{\partial \rho_\beta}$, therefore, the parametric algorithm requires the evaluation of $\frac{\partial \rho_\beta}{\partial \tau} \frac{\partial \tau}{\partial p_j}$ or $\frac{\partial \rho_\beta}{\partial \rho_{0,1}} \frac{\partial \rho_{0,1}}{\partial p_j}$. These derivatives are expressed below in Equation 3.23.

$$
\begin{aligned}
\frac{\partial \rho_\beta}{\partial m_1} &= -0.5a(\rho_1-\rho_0)(1-\tanh^2(a\tau))(x-x_0)^2 \\
\frac{\partial \rho_\beta}{\partial m_2} &= -0.5a(\rho_1-\rho_0)(1-\tanh^2(a\tau))(y-y_0)^2 \\
\frac{\partial \rho_\beta}{\partial m_3} &= -0.5a(\rho_1-\rho_0)(1-\tanh^2(a\tau))(z-z_0)^2 \\
\frac{\partial \rho_\beta}{\partial m_4} &= -a(\rho_1-\rho_0)(1-\tanh^2(a\tau))(x-x_0)(y-y_0) \\
\frac{\partial \rho_\beta}{\partial m_5} &= -a(\rho_1-\rho_0)(1-\tanh^2(a\tau))(x-x_0)(z-z_0) \\
\frac{\partial \rho_\beta}{\partial m_6} &= -a(\rho_1-\rho_0)(1-\tanh^2(a\tau))(y-y_0)(z-z_0) \\
\frac{\partial \rho_\beta}{\partial x_0} &= a(\rho_1-\rho_0)(1-\tanh^2(a\tau))(\mathbf{M}(x-x_0)) \\
\frac{\partial \rho_\beta}{\partial y_0} &= a(\rho_1-\rho_0)(1-\tanh^2(a\tau))(\mathbf{M}(y-y_0)) \\
\frac{\partial \rho_\beta}{\partial z_0} &= a(\rho_1-\rho_0)(1-\tanh^2(a\tau))(\mathbf{M}(z-z_0)) \\
\frac{\partial \rho_\beta}{\partial \rho_0} &= 0.5(1-\tanh(a\tau)) \\
\frac{\partial \rho_\beta}{\partial \rho_1} &= 0.5(1+\tanh(a\tau))
\end{aligned}
\tag{3.23}
$$

To calculate $\mathbf{J}_{i,j}$, the user defined inversion parameters $L, \hat{\rho}, a, c,$, from Equations 3.16, 3.19, and 3.20 need to be chosen. Experience suggests to choose L such that it represents a typical length scale of the problem, meaning it should be on the order of a few cell lengths, and in this thesis, L = 100. Select $\hat{\rho}$ such that it represents a moderately low resistivity value in the inversion. With resistivities varying by many orders of magnitude this can be difficult to select, but 10 Ωm is chosen throughout this work. Based on initial tests, the exact choice of L or $\hat{\rho}$ does not substantially change the inversion results and should not be a critical choice.

The parameters a and c collectively change the width of the transition zone between ρ_1 and ρ_0, as depicted in Figure 3.1 with initial parameters $[r_x, r_y, r_z] =$

$[25,50,25]$, $[\phi_x,\phi_y,\phi_z]=[0,0,0]$, $[x_0,y_0,z_0]=[0,0,0]$ and $[\rho_0,\rho_1]=[0,1]$. Selecting the parameter a to be larger results in a smaller transition zone. For the examples shown in this thesis, a = 10, such that a minimum of two mesh cells are present within the transition zone. It is suggested to choose a between 5 and 15 for best results. The inversion is less sensitive to the parameter c, but it is recommended to be set to 1 to keep initial radius guesses r_x, r_y and r_z consistent with the mapped radius values of the ensuing ellipsoid after the transformations from Equations 3.11 to 3.20. Figures 3.1a, 3.1b and 3.1c demonstrate a sharp step-off function followed by the resulting ellipsoids with a = 10 and the parameter c set to 1 and 5 respectively. Figures 3.1d, 3.1e and 3.1f show a gradual step-off followed by the corresponding ellipsoids with a = 0.5 and the parameter c set to 1 and 5 respectively. Figure 3.1b displays the ellipsoid constructed with the suggested choice of inversion parameters of $a=10$ and $c=1$.

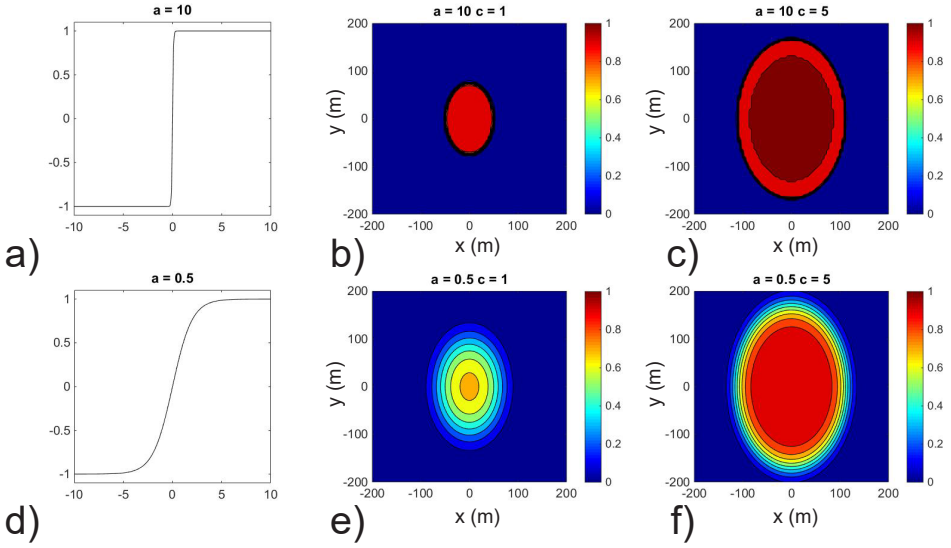

Figure 3.1: a) Analytic step-function with $a = 10$. b) Gaussian ellipsoid example with $a = 10$, $c = 1$. c) Gaussian ellipsoid example with $a = 10$, $c = 5$. d) Analytic step-function with $a = 0.5$. e) Gaussian ellipsoid example with $a = 0.5$, $c = 1$. f) Gaussian ellipsoid example with $a = 0.5$, $c = 5$.

3.5 Synthetic Results

3.5.1 Thin plate responses

Prior to inversion, it is worthwhile to look at $\frac{\partial \mathbf{b}_z}{\partial t}$ responses from a concentric loop time-domain AEM system over a thin, vertical or dipping conductive plate. The discretized triangular waveform used to calculate these curves is depicted in Figure 3.2 with measured time channels marked in black for reference. This waveform has a longer on-time pulse coupled with a slower shut-off decay compared to the NEWTEM-I waveform from Chapter 2, which is beneficial for detecting deep conductive targets (Allard, 2007).

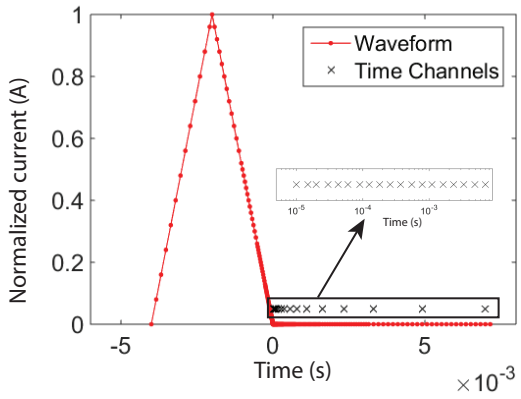

Figure 3.2: Triangular discretized waveform in red with measured time channels marked as black crosses.

Figure 3.3 displays three scenarios with a conductive 3 Ωm thin plate of dimensions 20 x 300 x 300 m in x, y, z buried 20 m below a flat topographic surface in a resistive half-space of 3000 Ωm. The transmitter and receiver are located 37.5 m above the earth, and the data consists of 19 time channels recorded between 10 μs - 7000 μs. Figure 3.3a demonstrates the classic symmetric double-peak response over a vertical dipping plate. Figure 3.3b displays how the symmetry is broken when the plate is tilted at a 45 degree angle, and Figure 3.3c shows a single broad high over a flat-lying thin conductive sheet.

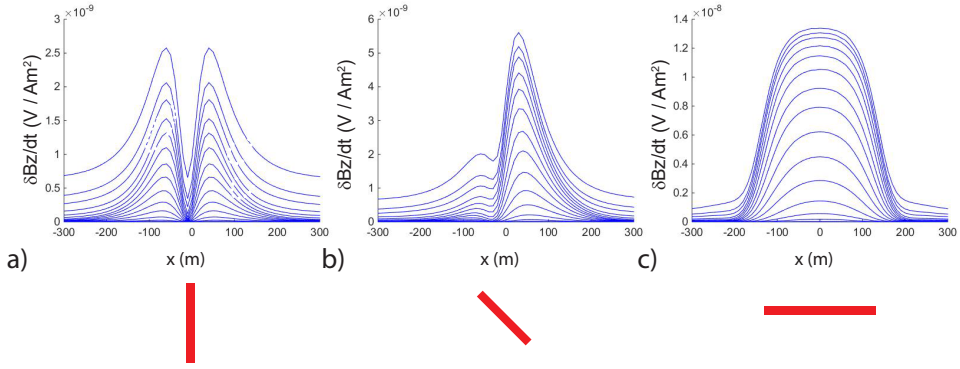

Figure 3.3: Noise-free $\frac{\partial \mathbf{b}_z}{\partial t}$ responses from a coincident loop AEM system flying 37.5 m over a thin 3 Ωm conductive plate in a 3000 Ωm background. a) Vertical plate buried 20 m below the surface. b) 45 degree dipping plate buried 20 m below the surface. c) Flat plate buried 20 m below the surface.

3.5.2 Synthetic dipping plate inversion results

To test the parametric inversion, a synthetic model of a buried plate-like dipping conductor is constructed in a resistive background. For simplicity, flat topography is included in this example. Figures 3.4a, 3.4b, and 3.4c portray sections through the synthetic model in each Cartesian direction. A time-domain AEM survey is simulated at a height of 37.5 m above ground with 49 transmitter locations over the dipping plate as shown by stars in Figure 3.4a. The data is composed of $\frac{\partial \mathbf{b}_z}{\partial t}$ data, contaminated with 5% Gaussian noise, calculated at 19 time channels using the waveform and time gates shown in Figure 3.2. The model is discretized on an ocTree mesh with core cells of 20 $\times$ 20 $\times$ 20 m for a total of 96,272 cells in the inversion mesh, and roughly 10,000 cells in the forward meshes. The resistivity of the plate is 3 Ωm in a uniform 3000 Ωm background. The dimensions of the dipping plate are 320 $\times$ 60 $\times$ 640 m in x, y, z respectively with a near vertical dip of 80 degrees in the positive y direction (east). Figures 3.4d, 3.4e, and 3.4f show the results from a voxel-based inversion alone (Haber and Schwarzbach, 2014) with a compact Ekblom regularization (Ekblom, 1973) on the smoothness component of the model norm, which demonstrates how a voxel algorithm has trouble imaging

this type of target. The resulting anomaly gets smeared, the resistivity magnitude is much too high, and the inversion is unable to capture the true dip.

For the parametric inversion, the initial guess consists of a 50 m radius sphere located at $[x, y, z]$ = [-120, 0, -150] in a uniform background. This is the same initial guess as the voxel-based inversion, although a similar voxel result ensues if a half-space is used as the starting guess. In the first example, the true anomalous and background resistivity is presumed known. In the second trial, incorrect values are assigned and the inversion calculates the resistivity parameters. Having a sphere as a starting guess provides minimal information with regards to the true size and dip of the anomaly, and it is a reasonable starting guess without having any a priori knowledge. Note, in the case where a portion of the recovered ellipsoid resides above ground, this region is set to a typical resistivity value of air.

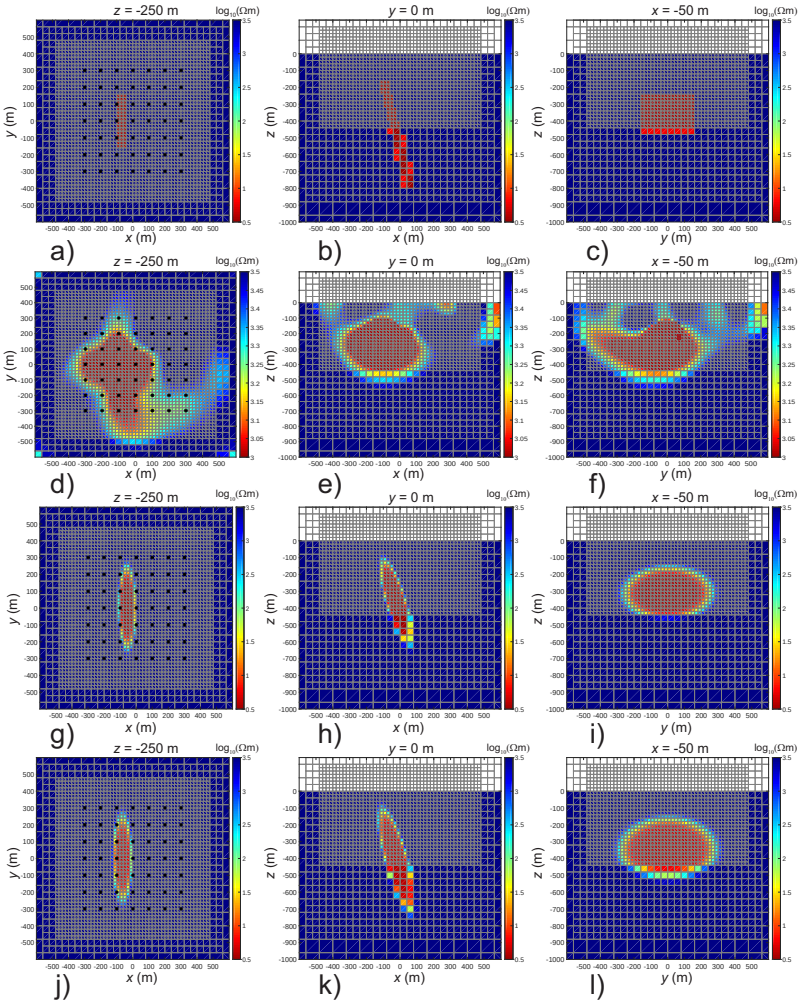

Figure 3.4: Plan view depth slices and cross-sections through the true model, recovered voxel-based inversion and recovered parametric models. a) True model at z = -250 m. b) True model along y = 0 m. c) True model along x = -50 m. d) Voxel model at z = -250 m. e) Voxel model along y = 0 m. f) Voxel model along x = -50 m. g) Parametric model at z = -250 m for fixed ρ. h) Parametric model along y = 0 m for fixed ρ. i) Parametric model along x = -50 m for fixed ρ. j) Parametric model at z = -250 m for variable ρ. k) Parametric model along y = 0 m for variable ρ. l) Parametric model along x = -50 m for variable ρ.

When the anomalous and background resistivities are fixed to the true values, the optimization over **p** finishes in 32 Gauss-Newton iterations. For the parametric stage, only a small number of poorly correlated parameters are sought, which in itself acts as a form of regularization. As such, an extra regularization term is not required and β is set to zero. Based on testing, this approach has been successful, but different regularization schemes in parametric and level-set inversions can be found in Aghasi et al. (2011); Dorn and Lesselier (2006); van den Doel and Ascher (2006); Zheglova and Farquharson (2016). At this point, the voxel-based stage solves for $\mathbf{m}_s$, but in this example there are no regional background features to resolve, and the sharp resistivity contrast between the homogeneous background and the thin plate favors a parametric inversion. Consequently, the voxel-based stage does not decrease the data misfit without adding spurious inversion artifacts. Although the parametric result does not reach the target data misfit, the voxel-based stage is considered to over-fit the data and the model after the first parametric stage is chosen as the final answer.

Although the concept of a target misfit is valuable for a stopping criteria, it is acknowledged that the Gaussian ellipsoid parameterization may not perfectly represent the true model or anomaly of interest, and the inversion may not reach the target misfit. As such, if the inversion terminates due to a stalled data misfit but does not reach the target level of unity, this suggests that the inversion has progressed as far as possible based on the assigned uncertainty values. In this case, the resulting model should have a significant reduction in data misfit to be considered an acceptable final result.

Sections through the recovered synthetic model are shown in Figures 3.4g, 3.4h, and 3.4i. These images show that the parametric algorithm is able to accurately recover the size, shape and dip of the anomaly compared to the true answer. The dip of the parametric model is roughly 74 degrees to the east, and this closely matches the true dip of 80 degrees to the east. One aspect not perfectly detected is the position of the plate bottom, which sits around 600 m in the parametric recovery and 800 m in the true model. This discrepancy can most likely be attributed to reduced sensitivity to model cells at depths greater than 600 m. Similar parametric results are produced when the initial guess is centered at z = -300 and z = -450, so the recovery is not highly sensitive to the exact depth of the initial guess.

The next example allows the resistivity to be variable, and incorrect anomalous and background values of 1 Ωm and 1000 Ωm are assigned. The choice of starting guess is open to the user, but naturally, the further the starting guesses are from the true resistivities, the more difficulties the program will have converging to the correct solution. With the chosen starting guesses, the parametric stage concludes after 29 Gauss-Newton iterations. As before, the voxel-based stage adds little improvement, and the model after the parametric stage is chosen as the final result. Cross-sections through the recovered variable resistivity inversion are displayed in Figures 3.4j, 3.4k, and 3.4l. The inversion defines the shape of the target with accurate precision with an estimated dip of 73 degrees to the east. The depth extent of the anomaly is slightly closer to the true model compared to the case when the true resistivities are assigned. Recovered anomalous and background resistivities are 3.97 Ωm and 3173 Ωm respectively.

A plan map of observed and predicted data at a mid-range time channel, 1110 μs, is displayed in Figure 3.5a and 3.5b. The plot is for the fixed resistivity inversion where the true values are assigned, although predicted data are similar in the variable resistivity case. An observed and predicted sounding from a selected location, marked with a cross in Figure 3.5a, is plotted in Figure 3.5c. Collectively, these images demonstrate the high level of agreement between the observed and predicted data. The initial and final data misfits are 70.4 and 3.8 for the fixed resistivity case and 2328.4 and 2.8 for the variable resistivity scenario. For both trials, the misfit at each Gauss-Newton iteration is summarized in Figure 3.5d. The misfit summary shows that both parametric inversions make excellent strides in reducing the data misfit but fall short of the target level.

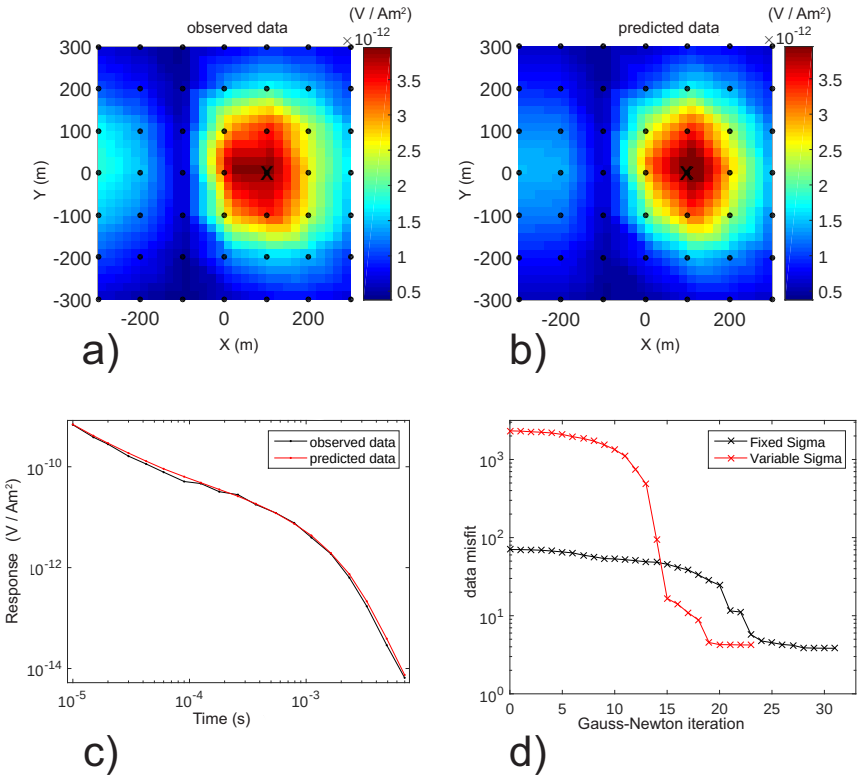

Figure 3.5: Synthetic dipping plate observed and predicted $\frac{\partial \mathbf{b}_z}{\partial t}$ data. a) Observed data at 1110 μs for fixed ρ, with a selected sounding marked with a cross. b) Predicted data at 1110 μs for fixed ρ, with a selected sounding marked with a cross. c) Fixed ρ observed and predicted data at selected sounding location. d) Fixed and variable resistivity data misfit progression.

A possible explanation for the lower final misfit when using a variable resistivity instead of true values is that a skewed Gaussian ellipsoid can not perfectly recover the staircase nature of a discretized dipping plate. It is also worth remembering that within the transition zone between ρ_0 and ρ_1, the anomaly does not contain the true resistivity value, but instead a weighted average of ρ_0 and ρ_1. Therefore, if the anomalous resistivity quantity is allowed to vary, it is possible that the inversion can find a shape and resistivity combination that fits the observed data better than correct values of ρ_0 and ρ_1. As an additional check to the code, the inversion reaches the same solution and data misfit as shown in the variable resistivity example when the initial guess is composed of spheres with fixed resistivities that match the previously achieved values of $\rho_0 = 3.97$ Ωm and $\rho_1 = 3173$ Ωm. This ensures that the fixed and variable version of the code are acting consistently.

Based on testing not presented, the parametric inversion achieves similar results when dealing with smaller resistivity contrasts, one or two orders of magnitude difference, between the background and target resistivity. In general, the encouraging results from the synthetic dipping plate parametric inversion suggest that similar success can be found with a more complicated field example.

3.6 Caber Case Study Results

3.6.1 Caber geology

The parametric hybrid approach is now applied to data from the Caber volcanogenic massive sulfide (VMS) deposit of western Quebec, Canada, as shown in Figure 3.6a. Within the Superior Province, the copper and zinc rich Caber deposit is part of the Matagami camp of the Abitibi greenstone belt (Carr et al., 2008). Geologically, the prominent McIvor fault separates Caber and accompanying gabbros, rhyolites and basalts from a granodiorite unit to the north-east (Adair, 2011). The local geology in plan view is depicted in Figure 3.6a and a simplified cross-section is displayed in Figure 3.6b (Prikhodko et al., 2010). The cross-section shows there is a thin conductive overburden layer above the ore-body that thickens to the north-east. The deposit itself is cigar-like in shape with a steep dip of 75 to 85 degrees to the south-west, and a strike direction of 125 degrees (Adair, 2011). The cross-section

also shows the near-vertical nature of a narrow shear zone proximal to the deposit, and nearby steeply dipping rhyolite and gabbro units.

The thin, buried nature of the Caber deposit, coupled with its position below conductive overburden, makes it a challenging target to detect with AEM techniques. Fortunately, the elevated conductivity of the deposit compared to surrounding rock units produces an anomalous electromagnetic response that is measurable from the air (Prikhodko et al., 2010). A small shear zone next to the deposit, which may be more conductive relative to the background but more resistive than the deposit, may contribute to the conductive response. For the purpose of this research, the response from the deposit and any contribution from the shear zone will be considered the target of interest.

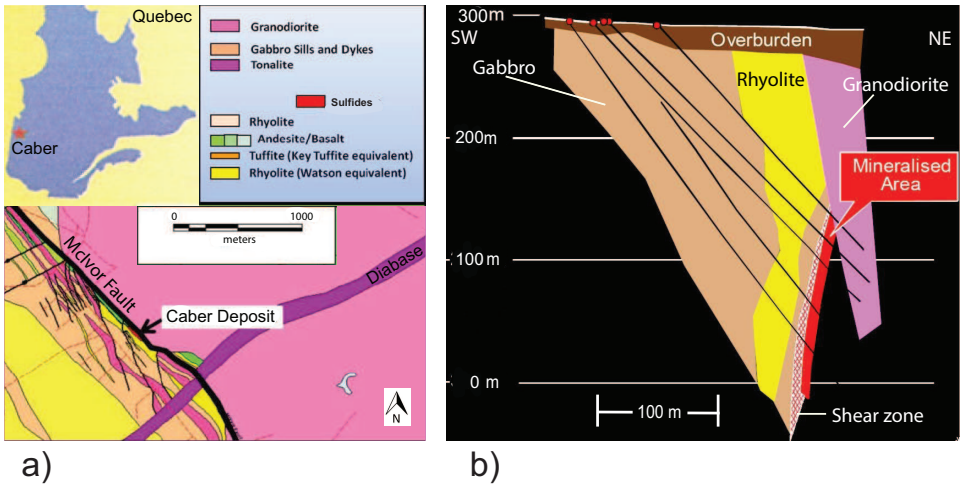

Figure 3.6: a) Caber deposit location and geology, modified from Prikhodko et al. (2010) and Adair (2011). b) Simplified deposit cross-section with drilling traces.

3.6.2 Caber time-domain AEM

The Caber AEM field data are inverted with the parametric hybrid approach. The AEM data at Caber consist of eight lines of Versatile Time-Domain Electromagnetic (VTEM-35) data, collected in 2012 with a 35 m diameter transmitter loop

and a peak dipole moment of 1,300,000 Am^2. See Allard (2007) for further information regarding the VTEM system. Due to relatively flat terrain, the drape of the transmitter above the ground varied between 34 m to 46 m, with a mean value of 40 m. The flight lines are spaced 50 m apart with a heading of 225 degrees. The discretized modified-triangular VTEM waveform is displayed in Figure 3.7 with 19 time channels ranging from 167 μs to 2021 μs marked with black x's for reference. Once again, a slower transmitter current shut-off compared to NEWTEM-I is designed to achieve a deeper penetration of the signal, but it is modified from a pure triangular wave to achieve a slightly steeper turn-off slope to detect near-surface weak conductors (Allard, 2007).

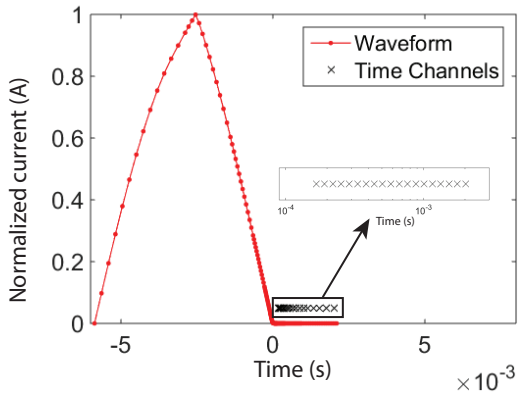

Figure 3.7: VTEM-35 (2012) discretized waveform in red with measured time channels marked as black crosses.

3.6.3 Caber parametric inversions

For the parametric inversion stage, a subsection of the total AEM survey over the Caber deposit is used, consisting of 102 transmitters of $\frac{\partial \mathbf{b}_z}{\partial t}$ data with 11 time channels ranging from 505 μs to 2021 μs. The model is discretized on an ocTree mesh with core cells of 20 $\times$ 20 $\times$ 20 m for a total number of 63,876 cells in the inversion mesh. The initial guess is a 50 m radius sphere, buried 150 m below the surface, with a resistivity of 0.2 Ωm positioned in the center of the observed $\frac{\partial \mathbf{b}_z}{\partial t}$ anomaly with a background of 1000 Ωm. In this field example, the true anomalous

and background quantities are unknown, and ρ_0 and ρ_1 are variables solved for in the inversion. Data uncertainties of 5% plus a time-channel dependent noise floor are applied. The noise floor is set to one order of magnitude lower than a 1000 Ωm half-space response. This varying noise floor is selected to weight each time channel as equally as possible in the inversion. The optimization over $\mathbf{p}$ concludes after 30 Gauss-Newton iterations and sections through the initial guess and resulting model in each Cartesian direction are shown in Figures 3.8a through 3.8f. The recovered model has a steep 80 degree dip to the south-west, which agrees with the known dip of the deposit. The final resistivities of the anomaly and background are 0.084 Ωm and 2118 Ωm respectively. As in the synthetic case, similar results are produced if the initial guess is moved to various locations and depths near the center of the observed $\frac{\partial \mathbf{b}_z}{\partial t}$ anomaly. The achieved anomaly value of 0.084 Ωm is well within the range of resistivities for massive sulfides (Palacky, 1988), and is similar to the value of 0.14 Ωm over a 30 m thickness obtained by Maxwell plate modeling (EMIT, 2005) of the 2012 AEM data over Caber from previous work (Prikhodko et al., 2012). Overall, the similarities between the two results are encouraging, and an exact match to a 30 m plate can not be expected with a Gaussian ellipsoid on a 20 m mesh discretization. Even with 15 m mesh cells, the results would not be expected to be identical since the methods use different approximations and parameterizations.

3.6.4 Caber hybrid parametric inversion

A plan map of observed and predicted parametric data for a mid-range time channel, 1010 μs, is displayed in Figure 3.9a and 3.9b. Overall there is a close agreement between the observed and predicted data, as they both exhibit a similar asymmetric double peaked response, indicative of a single dipping plate anomaly. Some discrepancies between the data sets exist, such as the break in the observed data that separates the southern lobe of the double peak that is not present in the predicted data. The inability to resolve fine levels of detail, such as this break, is a limitation of the first parametric stage of the hybrid approach, but the primary purpose of finding a best-fitting skewed Gaussian ellipsoid that matches the overall trend of the data is achieved. Observed and predicted data at a selected sounding

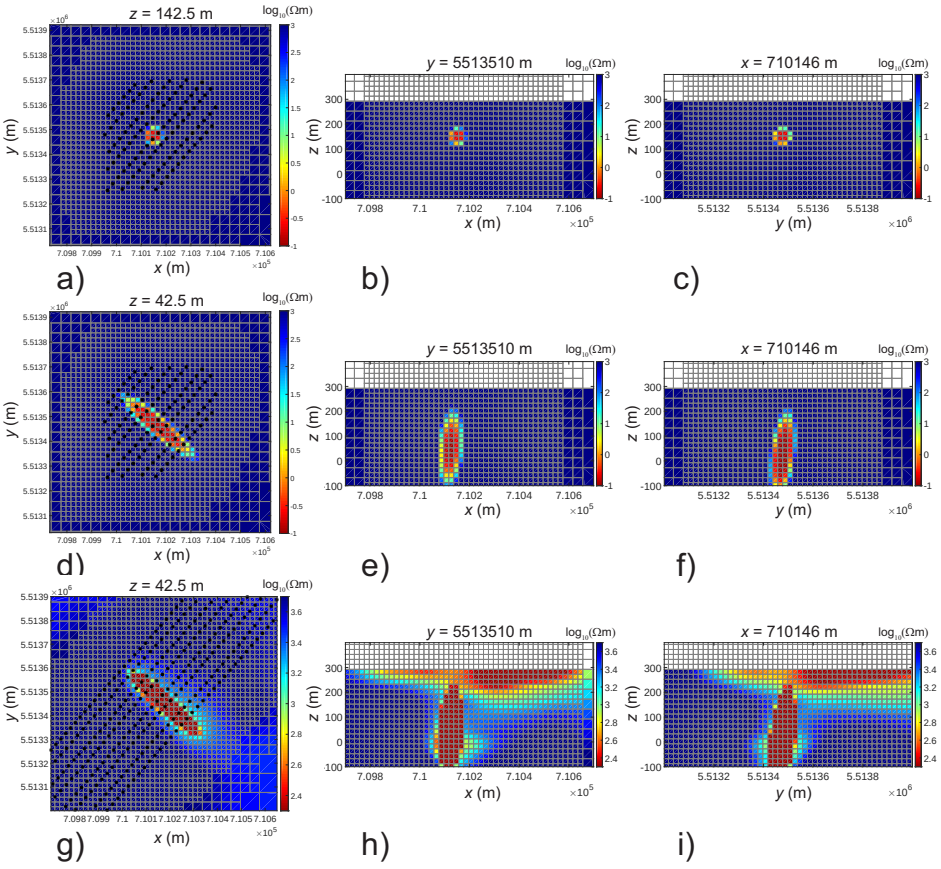

Figure 3.8: Plan view depth slices and cross-sections through the initial guess and recovered Caber parametric and hybrid models. a) Initial guess at z = 142.5 m. b) Initial guess along y = 5513510 m. c) Initial guess along x = 710146 m. d) Parametric model at z = 42.5 m. e) Parametric model along y = 5513510 m. f) Parametric model along x = 710146 m. g) Hybrid model at z = 42.5 m. h) Hybrid model along y = 5513510 m. i) Hybrid model along x = 710146 m.

in the center of the northern lobe, marked with a cross in Figure 3.9b are shown in Figure 3.9c, and a strong agreement is evident. The initial and final data misfits are 58.6 and 5.7 respectively, meaning the parametric approach reduces the data misfit by an order of magnitude, and the data misfit progression is summarized in

Figure 3.9d.

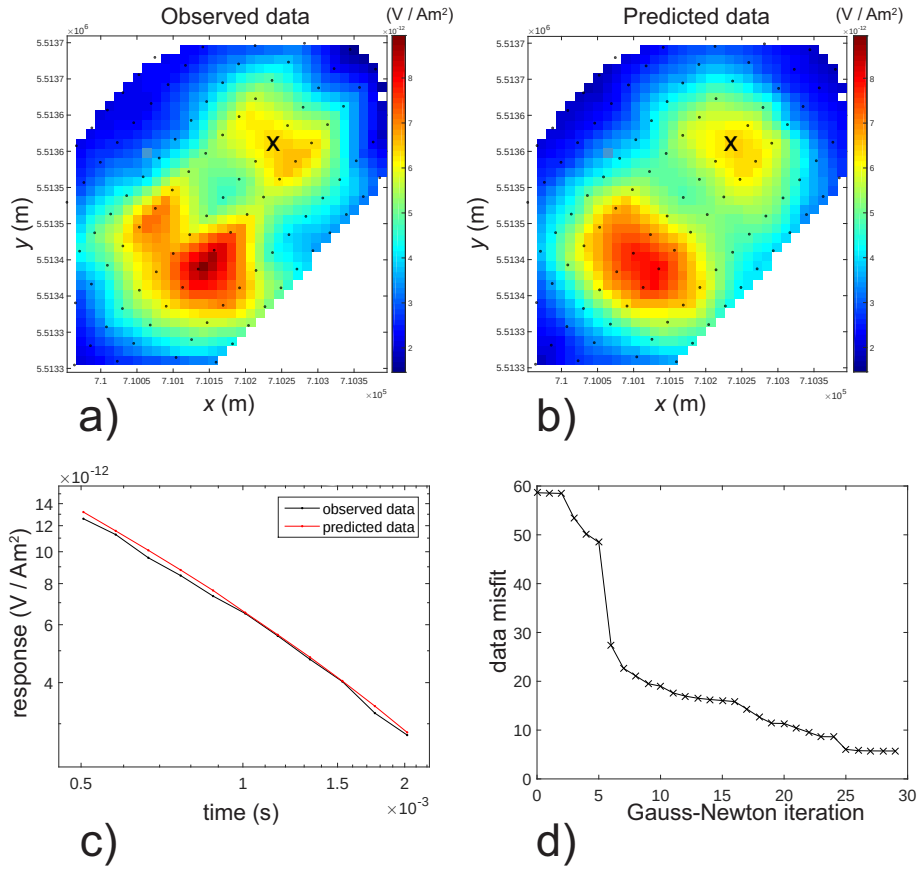

Figure 3.9: Caber observed and predicted $\frac{\partial \mathbf{b}_z}{\partial t}$ data. a) Observed data at 1010 μs with a selected sounding marked with a cross. b) Predicted data at 1010 μs with a selected sounding marked with a cross. c) Observed and predicted data at selected sounding location. d) Data misfit progression.

For the second stage of the hybrid approach, the parametric result is placed as the initial and reference model in order to optimize over $\mathbf{m}_s$, allowing the resistivity in every mesh cell to vary. Data from 19 time channels ranging from 167 μs to 2021 μs are included, and responses below a threshold of 1e-13 $\frac{V}{Am^2}$ are discarded because of potential noise concerns. In total, 727 transmitter locations from across the entire survey area are inverted with the same error assignments as in the para-

metric stage. Data over the central anomaly are included to allow the resistivity and shape of the parametric result to adjust if needed.

Over nine Gauss-Newton iterations, each composed of three inner iterations for a fixed β, $\mathbf{m}_s$ is optimized and the inversion converges to a data misfit of 0.95. The regularization parameter β starts at a value of 1e-3 and decreases by a factor of $\gamma = 0.2$ with each Gauss-Newton iteration. The starting β is much smaller compared to Chapter 2 because the parametric starting guess is a much more detailed initial model compared to a half-space, and the same cooling scheme as Chapter 2 is kept. Figures 3.8g, 3.8h and 3.8i show sections through the final hybrid parametric model. Once again the thin conductor is imaged, representing the Caber deposit. A different color bar is used for the hybrid result to show both the weakly conductive overburden and the strongly conductive target together. The Caber anomaly steeply dips to the south-west with a dip of 80 degrees, and an overburden unit over the conductor initially thickens to the north-east. The recovered size, dip and presence of overburden corroborates geologic information from Figure 3.6b, which adds confidence to this hybrid result. The shape and sharp boundaries of the dipping conductor are achieved through the parametric inversion, while the voxel-based inversion adds smooth features such as the overburden. Although the voxel-based stage can potentially alter the shape and resistivity of the Caber deposit, the anomaly only changes slightly from the parametric result.

Observed and predicted $\frac{\partial \mathbf{b}_z}{\partial t}$ data from time channel 505 μs, are illustrated in Figure 3.10. The predicted data at this time channel closely resemble the observed data, and clearly illustrate the response of the Caber deposit in addition to the conductive overburden in the north-east portion of the survey area. Holes in the observed and predicted data represent areas of resistive terrain where $\frac{\partial \mathbf{b}_z}{\partial t}$ responses drop below 1e-13 $\frac{\mathrm{V}}{\mathrm{Am}^2}$. Data from much of the south-west survey area is not shown due to data below this noise threshold.

To validate and ground truth the field inversion, Figure 3.11 displays a front and side view of a 0.4 Ωm iso-surface from the parametric result in red, the hybrid result in hatched gray, the massive sulfide deposit outline from drilling (M. Allard, personal communication, 2014) in light gray, and the aforementioned plate models for individual lines (Prikhodko et al., 2012) in yellow. The image demonstrates how the depiction of the Caber anomaly is extremely similar after both the para-

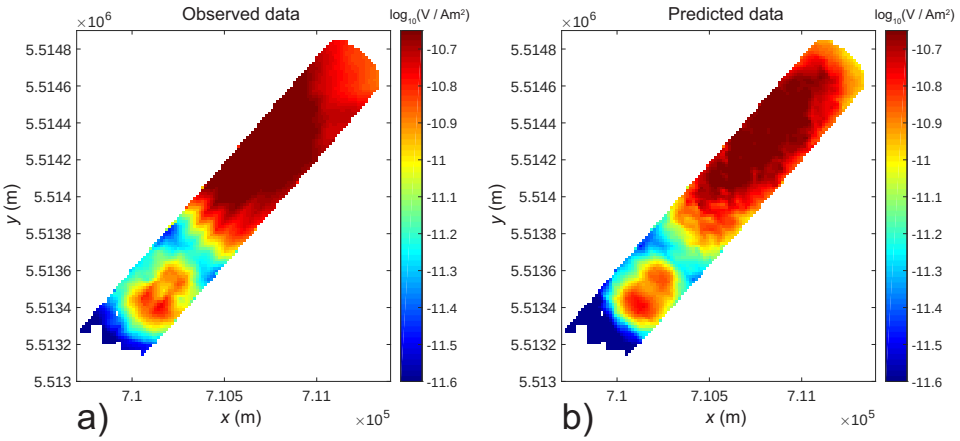

Figure 3.10: Caber observed and predicted data at 505 μs from the parametric hybrid inversion. a) Observed data. b) Predicted data.

metric and hybrid stages, however, the hybrid result is treated as the final model. The hybrid iso-surface accurately portrays the general size and dip of the target anomaly, although it stretches further to the south-east compared to the deposit model. Interestingly, previous AEM plate modeling also places conductive plates extending off the deposit. This suggests that additional conductive material to the south-east of the recorded sulfide zone is needed to explain the observed response. This anomalous material outside the deposit could be due to an unknown extension of the economic mineralization or the mapped shear zone shown in Figure 3.6b, or some combination of the two. As shown in the synthetic example, there is reduced inversion sensitivity at depth and caution must be taken when interpreting deep features. However, the parametric hybrid inversion provides a new interpretation to the cause of the conductive response from the 2012 time-domain AEM data.

The Gaussian ellipsoid parameterization has been shown to be successful for thin targets, but it also has the flexibility to map out larger anomalies such as intrusions or kimberlites. McMillan et al. (2015a) provides an example not shown in this thesis, where the parametric inversion uses time-domain AEM data to accurately image the DO-27 diamondiferous kimberlite deposit at Tli-Kwi-Cho (TKC) in the North-West Territories, Canada. Lessons from this work will be discussed in

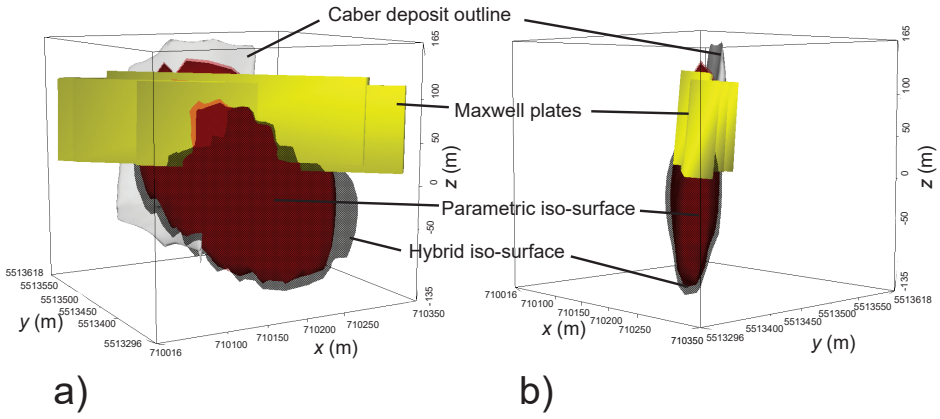

Figure 3.11: Caber deposit outline with inversion results. 0.4 Ωm iso-surface (red) from parametric stage, and 0.4 Ωm iso-surface (hatched gray) from hybrid inversion overlaid on Caber massive sulfide deposit model from drilling (light gray outline) and Maxwell plate anomalies (multiple yellow sheets) from five central lines of AEM data (Prikhodko et al., 2012). a) Looking north-east. b) Looking north-west.

further detail in Chapter 5.

3.7 Conclusions

A parametric hybrid inversion has been developed for AEM data to recover a target represented by a skewed Gaussian ellipsoid in a smooth background. This approach is valid for frequency and time-domain surveys, but it is tested in this chapter on time-domain synthetic and field AEM data. Here the target is a thin conductive plate-like body with a large resistivity contrast between itself and the resistive background. Both examples recover models that agree well with either the true synthetic answer or geologic information from past drilling respectively. The approach can be used as an alternative to a purely voxel-based inversion where sharp boundaries and large resistivity contrasts may not be imaged accurately. The parametric hybrid models are produced using a basic initial guess of a sphere without a priori information, which adds robustness to the algorithm. The results show

that the choice of parameterization is well suited for a thin, dipping plate target, but the approach is also applicable for other exploration environments such as mapping large intrusions or kimberlites.

For simplistic cases such as a synthetic dipping plate, the parametric stage does an admirable job in recovering the narrow target accurately. In a more complex example, such as the Caber case study, a hybrid approach is required, which is able to recover both the target of interest while including smooth features such as the conductive overburden. This task is not feasible with the parametric stage alone, and highlights the benefits of a hybrid approach.

For this single-anomaly version of the code, care must be taken in the parametric stage because in a scenario where two nearby conductive or resistive anomalies exist, the response may be modeled erroneously as a single anomaly. Thus, any a priori knowledge of the area coupled with a careful analysis of the observed and predicted data is needed to see whether one or multiple bodies are warranted. In this example, a priori information from plate modeling and drilling suggested that the Caber deposit could be depicted appropriately as one anomaly. Unfortunately, no physical property data existed from these bore holes to include as constraints into the inversion.

Chapter 4

Multiple Anomaly Parametric Inversion of AEM data

In this chapter, I demonstrate an extension of the single anomaly parametric inversion method to include multiple anomalies with distinct resistivity values for frequency and time-domain AEM data sets. The approach is designed to generalize the parametric inversion technique, making it more flexible for a variety of geologic settings and targets. The algorithm is tested with synthetic and field data from the West Plains orogenic gold deposit in Nunavut, Canada.

4.1 Introduction

Natural resource deposits come in all shapes and sizes. Some can be straightforward in their geometric nature as shown in the previous chapter, but this is true for only a handful of cases. A single body parametric code can be applied to simplistic examples, but for multiple targets, additional tools are needed. A logical progression, shown in this chapter, is to incorporate multiple parametric bodies into the inversion scheme, thus allowing the anomalies to interact and arrange themselves in more complex patterns. There are three primary research goals of this chapter and they are listed below.

- To extend the parametric inversion framework to include multiple anomalies and unique resistivity values for frequency and time-domain AEM data using

a skewed Gaussian ellipsoid parameterization.

- To show, with synthetic and field examples, that the multiple anomaly parametric inversion can accurately recover several thin dipping conductors, as typically found in orogenic gold settings.

- To apply the hybrid parametric approach to improve data fits and to fill in missing features not captured with a parametric inversion alone.

This chapter begins with a discussion regarding the extension of the parametric method from single to multiple anomalies. Synthetic inversions are then shown from frequency and time-domain AEM data over a model with three thin dipping conductors in a resistive half-space. Following the synthetic case, the hybrid inversion is tested on frequency and time-domain AEM field data from an orogenic gold deposit in the Canadian Arctic. The field results are subsequently evaluated in areas where geologic and mineralization knowledge from drilling exists.

4.2 Inversion methodology

The multiple anomaly parametric inversion method solves for an integer number (n) targets in a smooth or heterogeneous background. Each anomaly is once again represented by a skewed Gaussian ellipsoid; however, further discussion regarding the use of a multiple sphere parameterization can be found in Appendix A. Equation 4.1 shows the symmetric matrix $\mathbf{M}_n$ composed of the stretching and skewing parameters for the n^{th} ellipsoid.

$$\mathbf{M}_n = \begin{bmatrix} m_{1(n)} & m_{4(n)} & m_{5(n)} \\ m_{4(n)} & m_{2(n)} & m_{6(n)} \\ m_{5(n)} & m_{6(n)} & m_{3(n)} \end{bmatrix} \tag{4.1}$$

Observation locations ($\mathbf{x}$) are defined as described in the single anomaly version, with the central position of the n^{th} ellipsoid ($\mathbf{x}_{0(n)}$) written as

$$\mathbf{x}_{0(n)} = \begin{pmatrix} x_{0(n)} \\ y_{0(n)} \\ z_{0(n)} \end{pmatrix}. \tag{4.2}$$

The parametric function τ_n is now defined for the n^{th} anomaly as

$$\tau_n = c - (\mathbf{x} - \mathbf{x}_{0(n)})^{\mathbf{T}} \mathbf{M}_n (\mathbf{x} - \mathbf{x}_{0(n)}) \tag{4.3}$$

where c represents a positive constant, which is set to unity for all inversions. The zero level set is taken (Osher and Sethian, 1988) with a hyperbolic tangent analytic Heaviside function to split anomalous regions from the background. In each mesh cell, the separation of the n^{th} ellipsoid, denoted as H_n, from the background is defined as

$$\mathrm{H}_n = 1 - 0.5(1 + \tanh(a\tau_n)) \tag{4.4}$$

where a controls the steepness of the Heaviside function and is once again set to 10 for all inversions. H_n = 1 refers to a background resistivity value (ρ_0) and H_n = 0 equates to an anomalous resistivity value (ρ_a). To assign specific anomalous resistivity values, the approach from Tai and Chan (2004) is applied. For two anomalies in a homogeneous background the resistivity in each mesh cell is set to

$$\begin{aligned} \rho =& \rho_0(\mathrm{H}_1)(\mathrm{H}_2) + \rho_1(1-\mathrm{H}_1)(\mathrm{H}_2) + \\ & \rho_2(\mathrm{H}_1)(1-\mathrm{H}_2) + \rho_3(1-\mathrm{H}_1)(1-\mathrm{H}_2). \end{aligned} \tag{4.5}$$

Figure 4.1 shows an example of a cross-section through a parametric model with two anomalies, H_1 and H_2, with distinct resistivities, ρ_1 and ρ_2, an overlapping region with resistivity ρ_3 and a homogeneous background set to ρ_0.

For more than two anomalies, the method can be easily modified. One approach is to use an arbitrary number of parametric bodies, but to keep four unique resistivity values as in Equation 4.5. In this scenario, Heaviside functions from each anomaly H_n can be multiplied together (element-wise) to form two global Heaviside functions, Ψ_1 and Ψ_2, which are then substituted in for H_1 and H_2 in Equation 4.5. Here, all anomalies within Ψ_1 are assigned a value of ρ_1 and all within Ψ_2 are set to ρ_2. The overlap region of the two global Heaviside functions is set to ρ_3. The second approach is to assign a unique resistivity to each parametric body, however, with each additional anomaly, an overlap region must be

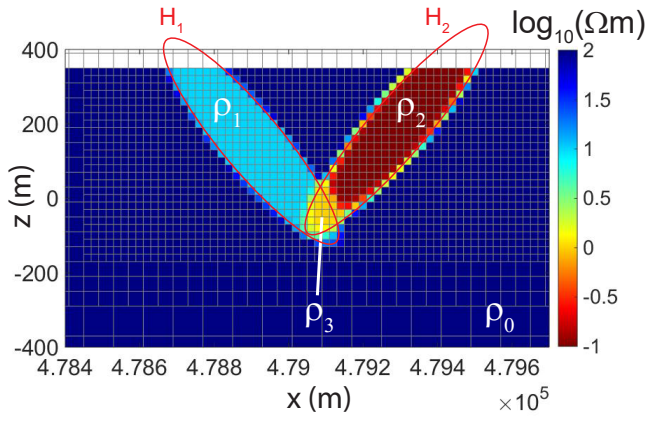

Figure 4.1: Cross section through a two-anomaly parametric model with four unique resistivity values (ρ_0 - ρ_3). H_1 and H_2 represent anomaly regions.

defined between itself and every other anomaly. This quickly increases the number of parameters needed, but may be necessary for certain situations. All examples shown in this thesis are suitable for the former approach, and this method is the focus moving forward.

The multiple anomaly parametric algorithm recovers a user-defined number of anomalies, and requires a starting guess for the location and resistivity of each target like the single anomaly version. Similar to Chapter 3, the inversion optimization follows a Gauss-Newton approach with a line search to determine an appropriate model update step, and the inversion parameters are scaled in the same manner. The sensitivity matrix $\mathbf{J}_{i,j}$ is also computed as in Chapter 3, except that $\frac{\partial \rho_\beta}{\partial \mathrm{H}} \frac{\partial \mathrm{H}}{\partial \tau}$ replaces $\frac{\partial \rho_\beta}{\partial \tau}$ for the derivatives with respect to location and skewing parameters as shown in Equation 4.6.

$$\mathbf{J}_{i,j} = \sum_{\alpha,\beta} \frac{\partial d_i}{\partial \rho_\alpha} \frac{\partial \rho_\alpha}{\partial \rho_\beta} \frac{\partial \rho_\beta}{\partial \mathrm{H}} \frac{\partial \mathrm{H}}{\partial \tau} \frac{\partial \tau}{\partial p_j} \tag{4.6}$$

4.3 Synthetic Results

To test the multiple body parametric approach, a frequency and time-domain AEM synthetic modeling study is performed, simulating an Arctic gold exploration setting. The motivation for the synthetic study comes from field data over the West Plains area of the Committee Bay greenstone belt in Nunavut, Canada. The location of this auriferous region is shown in Figure 4.2. This greenstone belt contains gold mineralization within ultramafic units such as komatiites and banded iron formations, which exist as a series of mainly linear, thin, dipping conductors in a resistive background (Kerswill, 1996). Hence, the synthetic model will contain multiple thin conductors, representing these ultramafic targets within a resistive host.

Figure 4.2: The West Plains area resides within the Archean Committee Bay greenstone belt in Eastern Nunavut, Canada

4.3.1 Synthetic model

The true synthetic model is composed of three dipping conductors of 0.2 Ωm, 2.0 Ωm and 2.0 Ωm respectively in a 1000 Ωm background with flat topography as shown in Figure 4.3a. The left panel displays a plan view at an elevation slice of 250 m (60 m below surface), and the solid white lines represent two East-West cross-sections shown in the right panel from top to bottom at y = 7333080 m and y = 7332780 m respectively. This same plan view and cross-section layout are used for all images in the synthetic study. Two of the conductors have a dip of 65 degrees with respect to the horizontal, one to the East and one to the West, while the third conductor has a vertical dip. The white dashed lines in plan view outline the starting guess locations for the parametric inversions. The synthetic data locations are taken from two overlapping AEM field data sets collected over the West Plains area: a 2005 frequency-domain RESOLVE (Viezzoli et al., 2009) and a 2003 time-domain VTEM (Allard, 2007) survey. The RESOLVE survey has 25 lines collected with a 310 degree heading with a variable line spacing of 60 m and 120 m. The drape of the transmitter varies between 22 m and 39 m with a mean terrain clearance of 30 m. The VTEM survey has 18 lines, and is also flown in a 310 degree direction with a variable line spacing of 60 m and 120 m. The transmitter height fluctuates between 22 m and 36 m with a mean height of 26 m. This average instrument drape is extremely low for a time-domain system, and is only possible due to essentially flat topography.

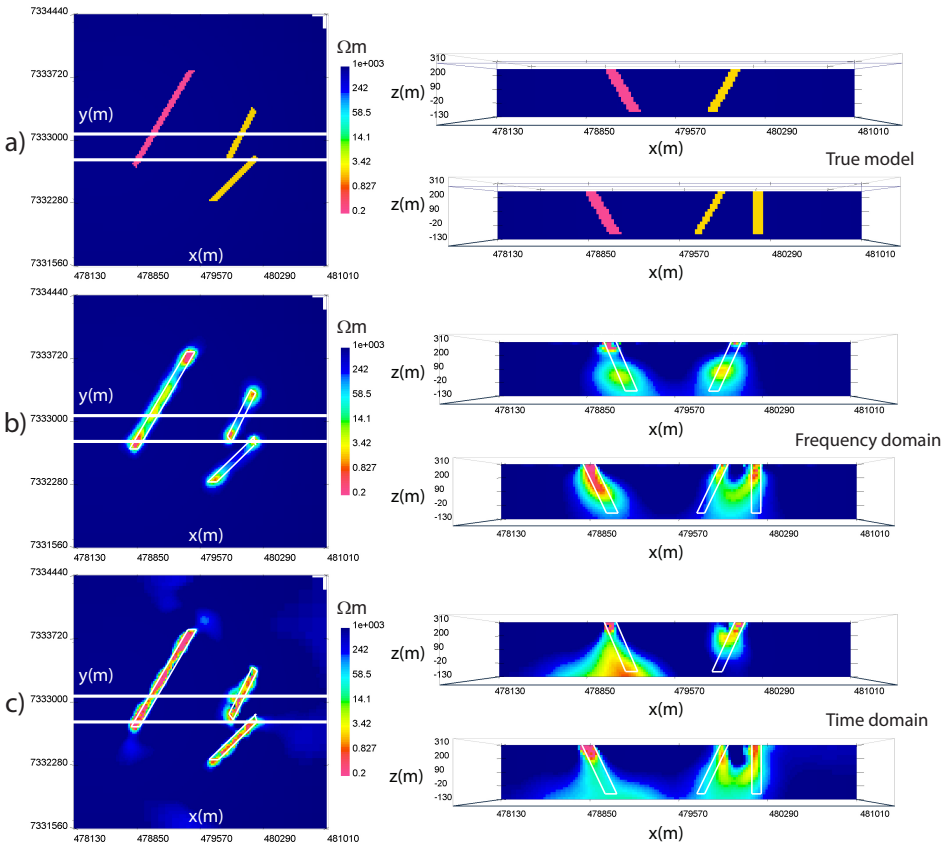

Figure 4.3: Frequency and time-domain AEM synthetic voxel inversions in plan view at z = 250 m (left panel) and cross-section across solid white lines at y = 7333080 m and y = 7332780 m (right panel). a) True synthetic model. b) Frequency-domain voxel inversion. c) Time-domain voxel inversion.

4.3.2 Synthetic data

Forward modeled data are contaminated with 3% Gaussian noise, and 3D inversions are completed with a conventional voxel-based inversion algorithm (Haber and Ascher, 2001; Oldenburg et al., 2013), and then with the multiple body parametric approach. In the frequency domain, the data consists of 793 source locations with 10 logarithmically spaced frequencies between 315 Hz and 6000 Hz of real and imaginary $\mathbf{H}_z$ data. In the time domain, 522 source locations are used with 20 logarithmically spaced time channels between 150 μs and 3180 μs of $\frac{\partial \mathbf{b}_z}{\partial t}$ data. The synthetic data uses a transmitter waveform similar to that seen in Figure 3.7 from Chapter 3, but with a 7.5 ms on-time pulse as shown in Figure4.4 to match the 2003 VTEM system. The inversion mesh consists of 289,979 cells with a finest dimension size of 20 x 20 x 20 m in x, y, z respectively, and the forward meshes contain roughly 10,000 cells per mesh. Inversion uncertainties are assigned as 3% of the observed data plus a noise floor that is one order of magnitude below the response from a 1000 Ωm half-space, to weight each time channel as equally as possible. In order to reduce the size of the system to speed up numerical computations, the data are down-sampled using a total horizontal gradient (THG) method of sampling. This technique computes the horizontal gradient amplitude for a particular frequency or time and uses this information to discard data in regions with slowly varying responses while preserving measurements where the response is rapidly changing. More details regarding THG sampling are described in Appendix B. To keep the locations consistent between the field and synthetic data, the THG sampling method is based on the field data observations at 385 Hz and 150 μs, although Appendix B shows that synthetic results improve when THG sampling is applied based on the synthetic data.

The time channels selected are from the 2003 VTEM system, and frequencies are chosen to give a similar depth of penetration compared to these time channels as per the skin depth and diffusion distance shown in Equations 1.7 and 1.8. This means that both data sets should have similar sensitivities to the target conductors. The synthetic study incorporates only 10 frequencies compared to 20 time channels to honor the reality that currently fewer frequencies are available on airborne systems such as RESOLVE compared to the number of time channels on time-domain

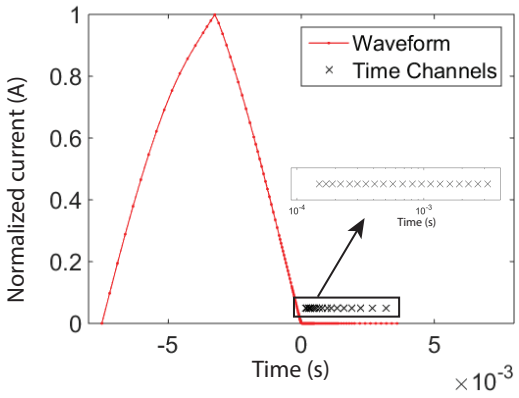

Figure 4.4: VTEM (2003) discretized waveform in red with measured time channels marked as black crosses.

airborne platforms such as VTEM, NewTEM, AeroTEM, HeliTEM MegaTEM and SkyTEM (Allard, 2007; Boyko et al., 2003; Eaton et al., 2013; Mulè et al., 2012; Smith et al., 2003; Sørensen and Auken, 2004).

4.3.3 Synthetic voxel inversions

Conventional voxel inversion results for the frequency and time-domain synthetic study are shown in Figure 4.3b and 4.3c respectively. The true background is presumed to be known for this study, and a 1000 Ωm half-space reference model is used with an Ekblom norm to promote thin anomalies. In Figures 4.3b and 4.3c, voxel inversions give a relatively accurate spatial recovery of the conductors in plan view but struggle to clearly identify the true dip and depth extent of the anomalies in cross-section.

4.3.4 Synthetic parametric inversions

Figure 4.5 shows the parametric inversion results using the same data and uncertainty values as the voxel trials, with the true model displayed in Figure 4.5a, the frequency inversion in Figure 4.5b and the time inversion in Figure 4.5c. Once again the true background is incorporated and the initial guess consists of three

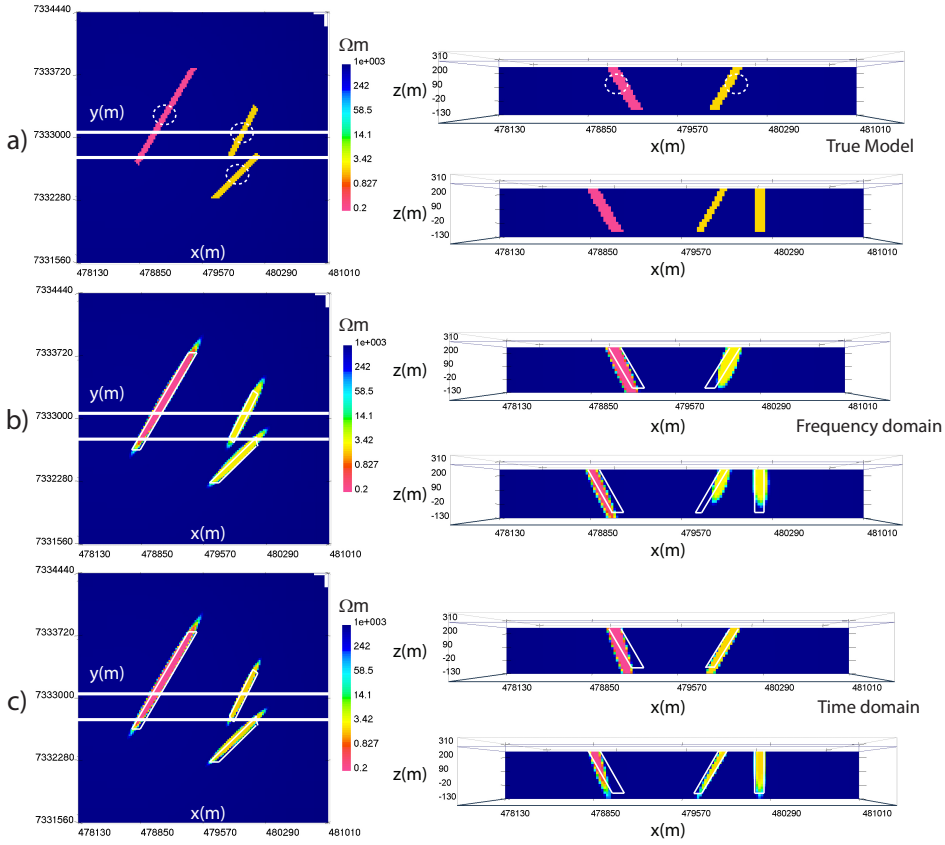

Figure 4.5: Synthetic parametric inversions in plan view at z = 250 m (left panel) and cross-section across solid white lines at y = 7333080 m and y = 7332780 m (right panel). Dashed white lines represent starting guess locations for parametric anomalies. a) True synthetic model. b) Frequency-domain parametric inversion. c) Time-domain parametric inversion.

200 m radius spheres of 1 Ωm centered over the anomalies of interest at a depth of z = 150 m. The starting guess locations are marked by dashed white lines in Figure 4.5a. Both the frequency and time-domain parametric results successfully spatially reconstruct the anomalies in plan view and give a much more accurate approximation of the respective dips in cross-section compared to the voxel inversions. The recovered target resistivities are 0.17 Ωm and 2.62 Ωm for the fre-

Table 4.1: Synthetic data inversion summary.

Inversion model	ρ_1	ρ_2	$\mathbf{R_c}$	$\mathbf{R_{All}}$	# GN	Final ϕ_d
True model	0.20 Ωm	2.00 Ωm	0.0	0.0	-	-
Voxel (freq)	Variable	Variable	2.73	0.39	96	4.2
Voxel (time)	Variable	Variable	2.58	0.75	45	17.2
Parametric (freq)	0.17 Ωm	2.62 Ωm	2.18	0.26	38	19.6
Parametric (time)	0.15 Ωm	1.99 Ωm	3.33	0.31	28	17.6

quency domain and 0.15 Ωm and 1.99 Ωm for the time domain. These values are extremely close to the true resistivities of 0.20 Ωm and 2.00 Ωm respectively. The results for all synthetic inversions are summarized in Table 4.1. Examining Figure 4.3 and Figure 4.5 suggests that a parametric inversion provides increased interpretation accuracy over voxel counterparts, and differences between frequency and time-domain inversions are minimal.

In an attempt to objectively evaluate the accuracy of each synthetic inversion, the quantitative metric from 2.1 is employed, and these values are displayed in Table 4.1. When only the conductive cells are taken into account, the frequency-domain parametric model outperforms the voxel result with a lower residual value of 2.18 compared to 2.73, but surprisingly the time-domain parametric model has a higher residual value of 3.33 compared to the voxel inversion at 2.58. This raises a concern with assessing synthetic inversions, because quantitatively the voxel model is more accurate, but the human eye can interpret and glean more true information in terms of the size and dip of the various conductors from the parametric model. In contrast, when all of the cells in the model are taken into account, both parametric models show a better quantitative result. These metrics demonstrate a potential issue when interpreting purely quantitative assessments of synthetic models, because a model may be deemed more accurate but could be less useful to the interpreter. This suggests that an improved model for human interpretation is not necessarily always quantitatively more accurate.

Observed and predicted $\mathbf{H}_z$ data at 450 Hz and $\frac{\partial \mathbf{b}_z}{\partial t}$ data at 150 μs from the synthetic parametric inversions are displayed in Figure 4.6 along with survey locations as black dots. All predicted data visually match closely with observed measurements, and data misfit curves are presented in Figure 4.7. Both data sets show a comparable decrease in misfit although the final data misfits of 19.6 and 17.6 are well above the target misfit of unity. This is most likely due to the small 3% assigned error percentage, and future models can be run with a higher assigned noise percentage to achieve a smaller data misfit, however similar results are expected. Note that the time-domain voxel inversion terminated at a similar data misfit level of 17.2, whereas the frequency-domain voxel inversion converged to a value of 4.2. This small misfit level for the frequency voxel model is most likely due to the placement of high-frequency near-surface conductive features, which may be artifacts.

Figure 4.8 shows a 5 Ωm iso-surface view of the parametric synthetic inversions, which gives a way of looking at only the conductive cells of interest. Figure 4.8a displays the true model with the starting guess model shown in Figure 4.8b. Figure 4.8c and Figure 4.8d display the frequency and time-domain parametric inversions. Collectively Figure 4.8 visually demonstrates how a Gaussian ellipsoid parameterization geometrically matches a dipping plate target extremely well. Of course this example is designed for this purpose, but the motivation stems from a case study that will now be discussed.

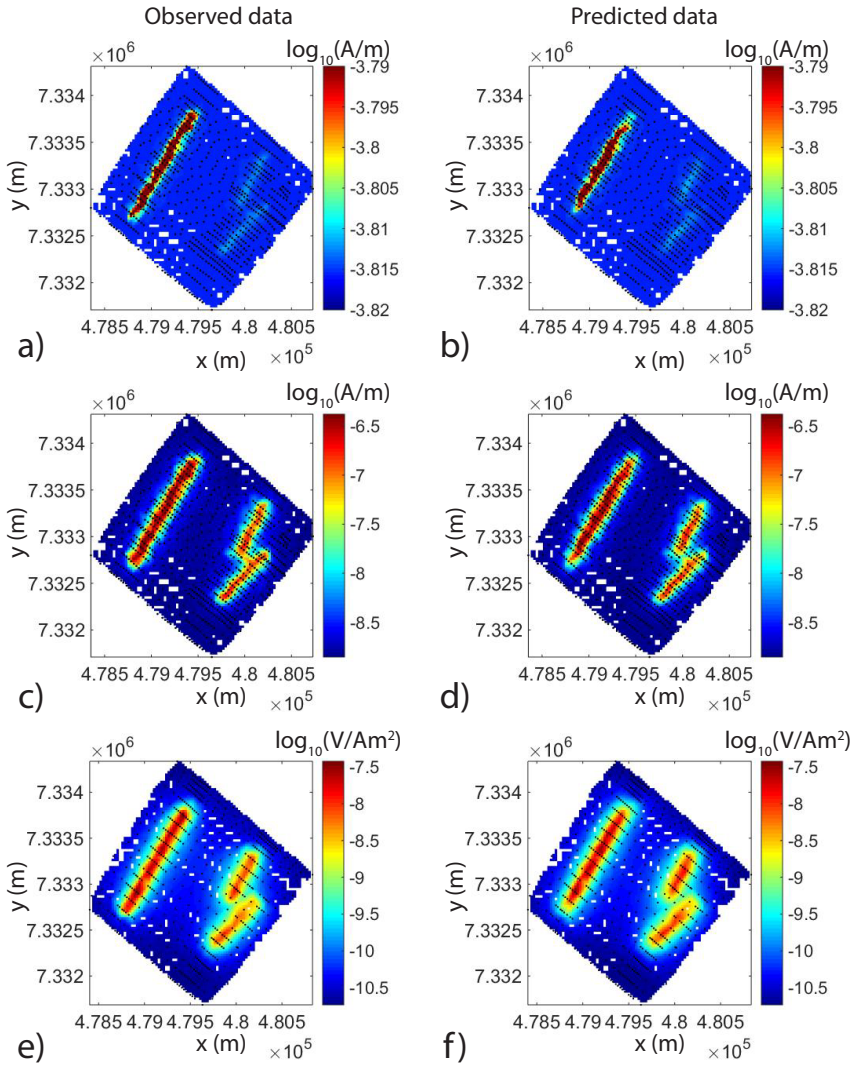

Figure 4.6: Observed and predicted synthetic data from parametric inversions with locations shown as black dots. a) Observed data - real $\mathbf{H}_z$ at 450 Hz. b) Predicted parametric data - real $\mathbf{H}_z$ at 450 Hz. c) Observed data - imaginary $\mathbf{H}_z$ at 450 Hz. d) Predicted parametric data - imaginary $\mathbf{H}_z$ at 450 Hz. e) Observed data - $\frac{\partial \mathbf{b}_z}{\partial t}$ at 150 μs. f) Predicted parametric data - $\frac{\partial \mathbf{b}_z}{\partial t}$ at 150 μs.

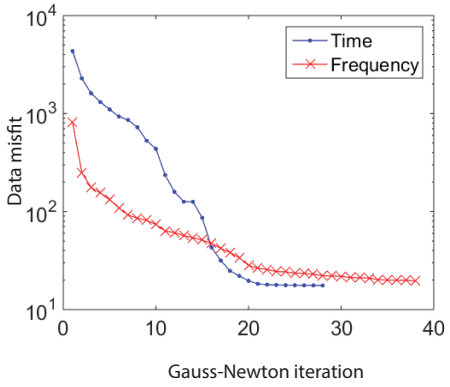

Figure 4.7: Synthetic parametric data misfit progression.

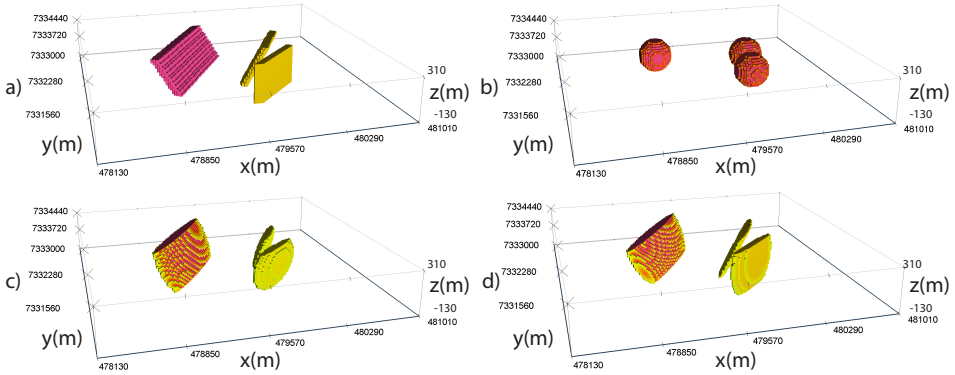

Figure 4.8: Frequency and time-domain parametric inversion 5 Ωm iso-surfaces. a) True synthetic model. b) Starting guesses. c) Frequency-domain parametric inversion. d) Time-domain parametric inversion.

4.4 West Plains Case Study Results

Based on the success of the synthetic study, the multiple body parametric approach is now applied to field AEM data from the West Plains project.

4.4.1 West Plains geology

West Plains is an active orogenic gold exploration project, located in the South-West portion of the Archean Committee Bay greenstone belt, which itself is part of the larger Rae geologic domain, in Eastern Nunavut, Canada (Skulski et al., 2003). The project is owned by Auryn Resources Inc., and the economic gold mineralization is hosted in conductive units within a resistive background, a scenario well suited for AEM data. A simplified geology map of West Plains is shown in Figure 4.9 with the outline of overlapping frequency and time-domain AEM surveys in black. The geology consists of a series of ultramafic komatiite units shown in dark purple, named the Prince Albert Group, that cut through a sediment package shown in light purple (Carson et al., 2004). The komatiites and sediments are bounded by granodiorites to the North-West and tonalites to the South-East. The komatiites contain the majority of the gold mineralization, and garnering a better understanding of their 3D geometry represents the focal point of this study.

Geologic outcrops are scarce in the West Plains region, and the simplified geology map is compiled mainly from regional magnetic data analysis. The geologic interpretation from Figure 4.9 does not include information from AEM data, which means there is plenty of room for improvement based off 3D AEM inversion results. From the geology and drilling, it is believed that three conductive units exist, comprised of a Western conductor, numbered 1 on Figure 4.9, and two near-parallel or possibly intersecting conductors in the East, numbered 2 and 3 on Figure 4.9.

4.4.2 West Plains AEM data

AEM field data locations and inversion meshes are kept the same as the synthetic case and the assigned uncertainties are applied in the same manner. $\mathbf{H}_z$ data from five coplanar frequencies (385, 1500, 6200, 25,000 and 115,000 Hz) are used in the frequency domain, and the same 20 time channels of $\frac{\partial \mathbf{b}_z}{\partial t}$ data from the synthetic section are inverted in the time domain.

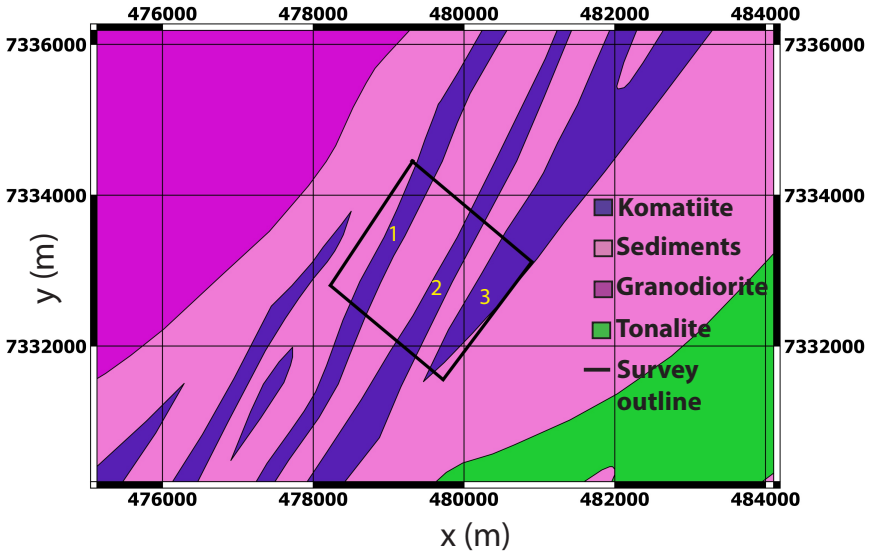

Figure 4.9: Simplified West Plains geology map with major lithology units defined and location of overlapping frequency and time-domain AEM surveys outlined in black. Conductive komatiite units of interest are numbered in yellow.

Selected data maps from West Plains are shown in Figure 4.10. Imaginary component $\mathbf{H}_z$ data from the lowest frequency, 385 Hz, is portrayed in Figure 4.10a and from the highest frequency, 115,000 Hz, in Figure 4.10b. The low-frequency grid clearly highlights the conductors of interest and has a relatively quiet signal elsewhere in the survey area. Conversely, the high-frequency grid has a response from the conductors, but also detects near-surface features such as clay layers associated with lakes and rivers. Subsets of the data could be used in an attempt to isolate the conductors, however all the data are input to show the robustness of the parametric algorithm.

Time-domain $\frac{\partial \mathbf{b}_z}{\partial t}$ data from the earliest time, 150 μs, are shown in Figure 4.10c and from the latest time, 3180 μs, in Figure 4.10d. The earliest time channel does

an excellent job in mapping out the target conductors without much influence from lakes. However, at later times the data become noisier and measurements below a perceived noise threshold of 5e-12 $\frac{V}{Am^2}$ are removed for quality control purposes. This threshold is chosen by looking at the amplitude at which point the electromagnetic response no longer consistently decays monotonically and oscillates due to noise. As can be seen in Figure 4.10d, only data points near the strong conductors have amplitudes above this threshold at late times. This perceived noise level is an order of magnitude higher compared to data over the Caber deposit described in Chapter 3. The noisiness of VTEM data at West Plains compared to Caber, emphasizes the improvements in noise reduction of time-domain AEM data between 2003 and 2012.

4.4.3 West Plains voxel inversions

Conventional voxel inversion results are shown for frequency and time-domain AEM data at West Plains in Figure 4.11a and 4.11b with plan view slices at a constant elevation of z = 190 in the left panel and cross-sections from y = 7333080 m and y = 7332780 m in the right panel. Inversion parameters are selected to match those from the synthetic example. Data misfit progression curves from the voxel inversions are shown in Figure 4.12a.

The voxel inversions recover a linear Western conductor and two Eastern conductors although the distinction between the two conductive units in the East is not consistently clear. In cross-section, the two inversions bare few similarities, as the conductors in the frequency-domain are compact near-surface objects while the time-domain result produces anomalies that are larger and extend to depth. The presence of near-surface features in the frequency domain and not in the time domain is not entirely surprising, since the skin depth from observed frequencies ranges from 47 m to 810 m, whereas the diffusion distance from observed time channels varies from 487 m to 2247 m, using a 1000 Ωm background.

4.4.4 West Plains parametric inversions

To complement the voxel models, parametric inversions are computed to image more clearly the three conductive komatiite units at West Plains. Appropriately,

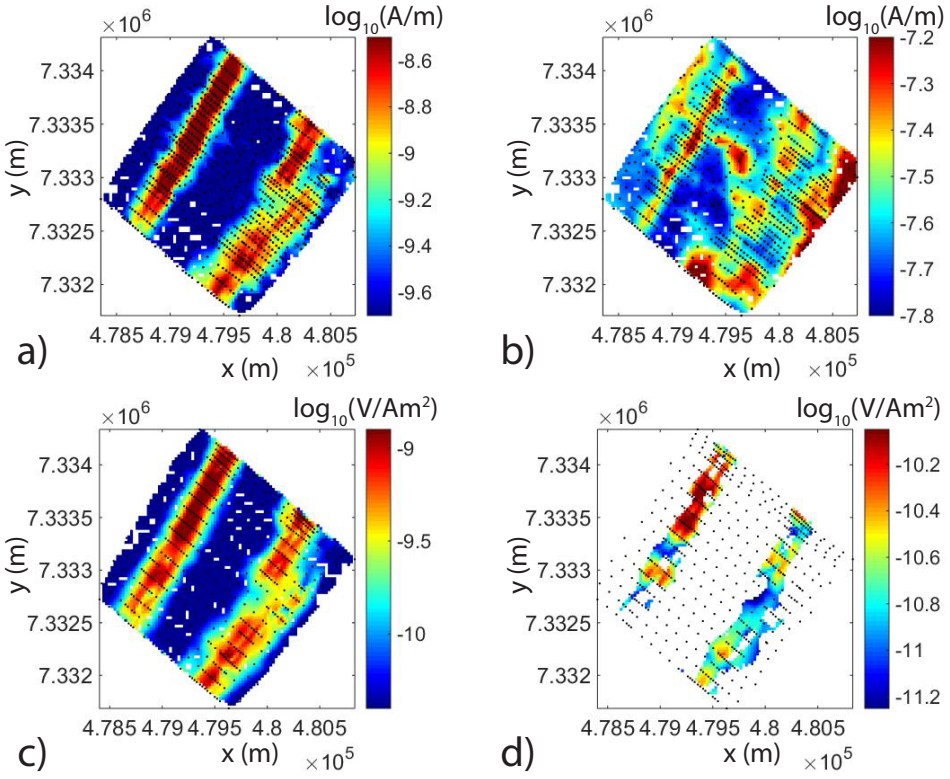

Figure 4.10: Frequency and time-domain field data. a) Imaginary $\mathbf{H}_z$ at 385 Hz. b) Imaginary $\mathbf{H}_z$ at 115000 Hz. c) $\frac{\partial \mathbf{b}_z}{\partial t}$ at 150 μs. d) $\frac{\partial \mathbf{b}_z}{\partial t}$ at 3180 μs.

the parametric algorithms are set to recover three conductors, with the Western conductor chosen to have its own resistivity value and the Eastern units sharing a best-fitting resistivity. This is based on a priori knowledge that the two Eastern conductors are similar in nature. Figure 4.13a shows the frequency-domain field parametric inversion, with a plan view slice through the model at $z = 190$ m in the left panel. The solid white lines represent two East-West cross-sections displayed in the right panel at y = 7333080 m and y = 7332780 m. The dashed white lines indicate the spatial outlines of the 1 Ωm starting guesses centrally located at a depth of $z = 150$ m. The recovered target resistivities in the frequency-domain are 0.15 Ωm and 7.28 Ωm with a background of 12,609 Ωm. Comparatively, the

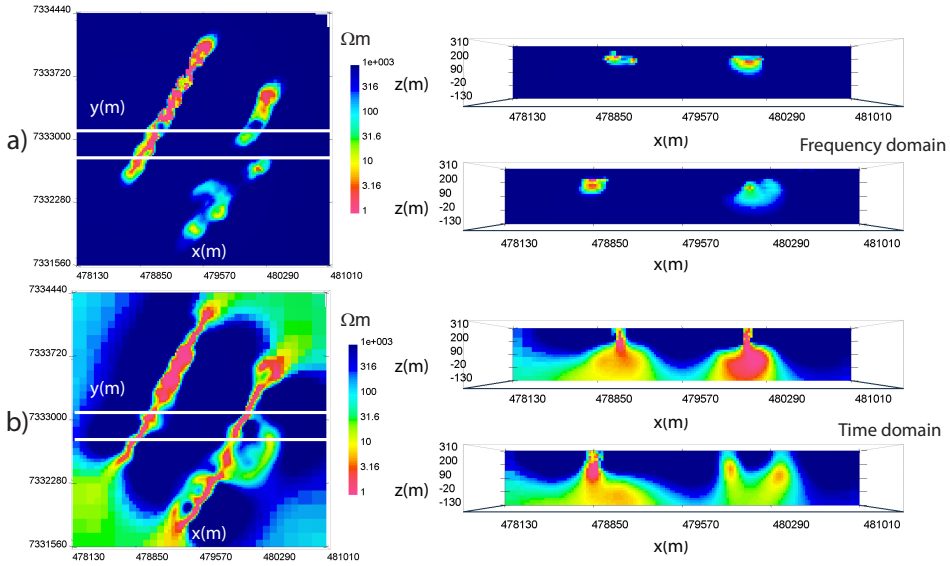

Figure 4.11: Frequency and time-domain West Plains voxel inversions in plan view at z = 190 m (left) and cross-section across solid white lines at y = 7333080 m and y = 7332780 m (right). a) Frequency domain. b) Time domain.

time-domain model, which is shown in plan view and cross section in Figure 4.13b, recovers resistivities of 0.28 Ωm and 0.11 Ωm with a background of 495 Ωm. West Plains parametric inversion statistics, including recovered resistivities, number of Gauss-Newton iterations required and final data misfit values are summarized in Table 4.2. Data misfit curves are displayed in Figure 4.12b, where the initial part of the curve represents the parametric portion while the latter half is the hybrid inversion discussed in the next section.

In plan view, the frequency and time-domain models have many spatial similarities, although the absolute recovered resistivities are much lower in the time-domain for the Eastern conductors (ρ_2) and the background (ρ_0). This suggests that there is some disagreement between the two AEM data sets, and the discrepancy in ρ_0 will be addressed in greater detail in Chapter 5. In cross-section, the Western conductor has a similar shape and steep dip to the West in both inversions;

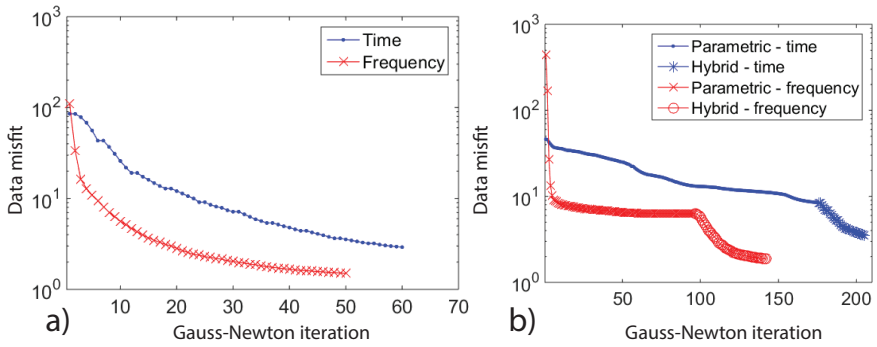

Figure 4.12: West Plains data misfit progression. a) Voxel inversions. b) Parametric and hybrid parametric inversions.

Table 4.2: Field data inversion summary.

Inversion model	ρ_1	ρ_2	ρ_0	# GN	Final ϕ_d
Voxel (freq)	variable	variable	variable	49	1.50
Voxel (time)	variable	variable	variable	60	2.92
Parametric (freq)	0.15 Ωm	7.28 Ωm	12609 Ωm	96	6.27
Parametric (time)	0.28 Ωm	0.11 Ωm	495 Ωm	175	8.49
Hybrid (freq)	variable	variable	variable	47	1.87
Hybrid (time)	variable	variable	variable	40	3.51

however, the Eastern conductors appear different. In the frequency domain, the Eastern conductors are rounder compared to the time-domain results, with a steep dip to the East. In contrast, the time-domain model has a thin central conductor that steeply dips to the West, and a small near-surface Eastern conductor. Rectangular blocky anomalies in the North-East corner of the parametric models are outside the observed data area, within padding cells, and should be ignored.

Observed and predicted field data are shown in Figure 4.14. Real-component $\mathbf{H}_z$ data at 385 Hz are shown in Figure 4.14a along with parametric predicted data in Figure 4.14b. Observed and parametric predicted imaginary $\mathbf{H}_z$ data are displayed in Figure 4.14d and Figure 4.14e respectively. Time-domain observed $\frac{\partial \mathbf{b}_z}{\partial t}$ data at 150 μs are shown in Figure 4.14g with parametric predicted data in Figure 4.14h.

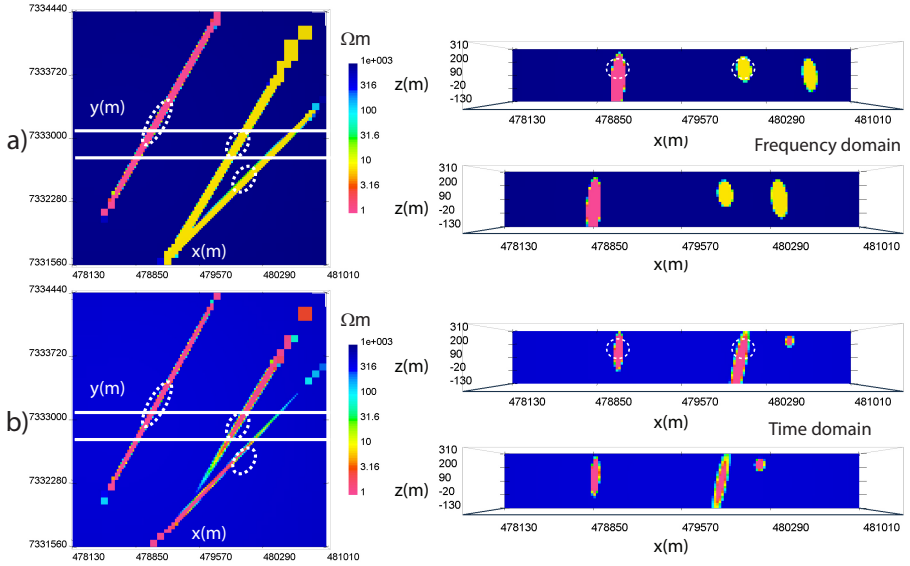

Figure 4.13: West Plains parametric inversions in plan view at an elevation of z = 190 m (left) and cross-section across solid white lines at y = 7333080 m and y = 7332780 m (right). Dashed white lines represent starting guess locations for parametric anomalies. a) Frequency domain. b) Time domain.

The parametric predicted data from Figure 4.14 closely resemble the observed data, but further improvements can be made such as fitting two amplitude highs in the real-component image of Figure 4.14a that are missing in the predicted data. Additional modifications to the parametric models to fit detailed features is the benefit of the hybrid parametric method.

4.4.5 West Plains hybrid parametric inversions

As shown in Chapter 3, a hybrid parametric inversion incorporates the parametric result as an initial and reference model for a voxel inversion. In the voxel stage, all cells are kept active, meaning that the resistivity value can change in each mesh cell. This process allows information from the parametric stage to be passed to the voxel stage, which then inserts complexities into the model not possible with Gaussian ellipsoids only. The hybrid method is applied to parametric results from the

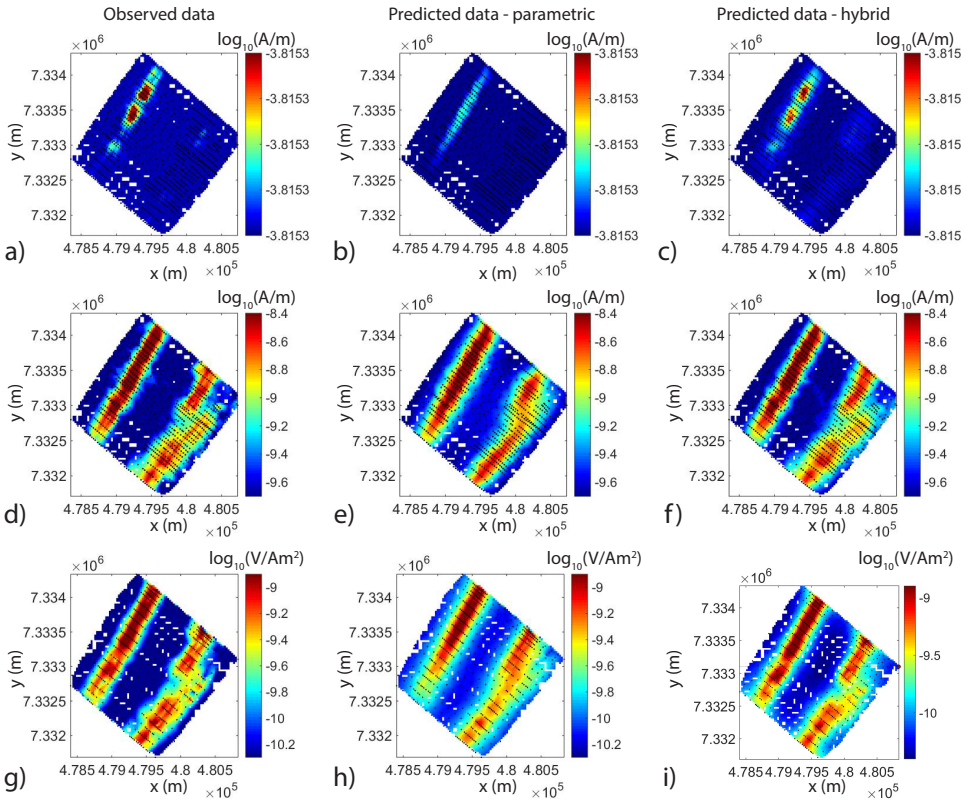

Figure 4.14: Observed and predicted field data from parametric and hybrid inversions with locations shown as black dots. a) Observed data - real $\mathbf{H}_z$ at 385 Hz. b) Predicted parametric data - real $\mathbf{H}_z$ at 385 Hz. c) Predicted hybrid parametric data - real $\mathbf{H}_z$ at 385 Hz. d) Observed data - imaginary $\mathbf{H}_z$ at 385 Hz. e) Predicted parametric data - imaginary $\mathbf{H}_z$ at 385 Hz. f) Predicted hybrid parametric data - imaginary $\mathbf{H}_z$ at 385 Hz. g) Observed data - $\frac{\partial \mathbf{b}_z}{\partial t}$ at 150 μs. h) Predicted parametric data - $\frac{\partial \mathbf{b}_z}{\partial t}$ at 150 μs. i) Predicted hybrid parametric data - $\frac{\partial \mathbf{b}_z}{\partial t}$ at 150 μs.

previous section and hybrid frequency and time-domain AEM models from West Plains are displayed in Figure 4.15. Figure 4.15a displays the frequency model, and in plan view it is evident that the voxel stage alters the resistivity within the three conductors in an attempt to concentrate areas of high conductivity in certain places. In cross-section, this effect is even more apparent as the Eastern conductor now has

a concentrated near-surface conductivity high similar to the time-domain result. Figure 4.15b shows the hybrid time-domain inversion, which only has minor deviations from the parametric result. The voxel inversion places diffuse conductive zones around the main anomalies, but does not change the resistivity distribution within the conductors to any large degree.

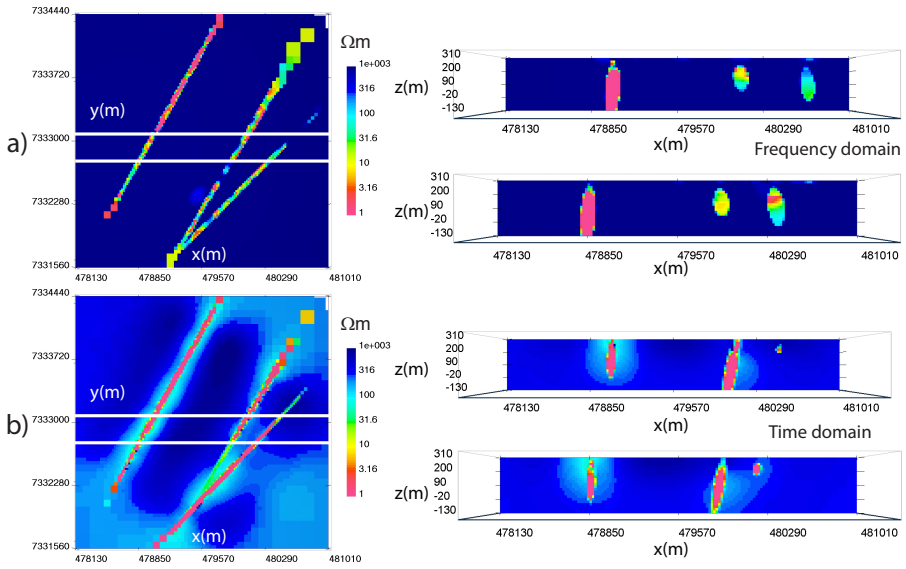

Figure 4.15: West Plains hybrid parametric inversions in plan view at an elevation of z = 190 m (left) and cross-section across solid white lines at y = 7333080 m and y = 7332780 m (right). a) Frequency domain. b) Time domain.

The hybrid inversion also adds near-surface conductive zones due to clay layers and lakes as seen in Figure 4.16 where plan view slices at the model surface are displayed from both data sets. The colorbars have been modified to best display near-surface features, which are more pronounced in the frequency-domain model compared to the time-domain, as would be expected due to a greater near-surface sensitivity.

Modified conductivity structures added from the voxel stage of the hybrid method permit a closer data fit compared to parametric inversions alone as presented in Figure 4.14. Here the hybrid predicted data closely matches the observed

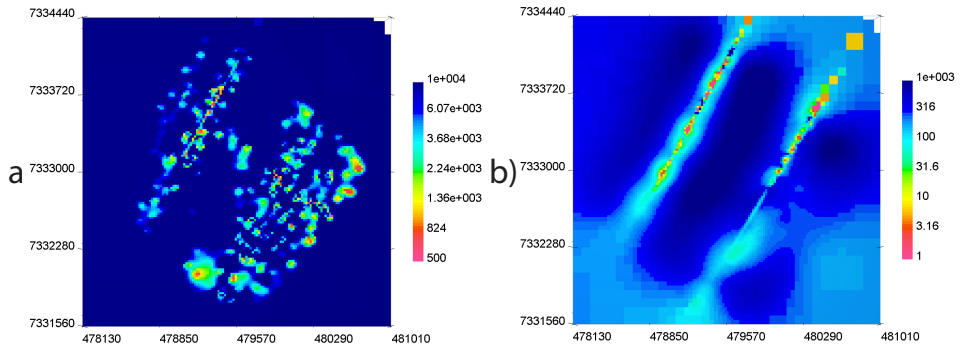

Figure 4.16: West Plains hybrid parametric inversions in plan view at an elevation of z = 310 m (surface). a) Frequency domain. b) Time domain. Note the colorbars are different to highlight near-surface features.

data. Specifically, the double amplitude high in the real-component $\mathbf{H}_z$ data is now present in the hybrid predicted data in Figure 4.14c. Hybrid misfit curves are displayed in the latter half of Figure 4.12b where the voxel stage lowers the achieved misfit from 6.27 to 1.87 in the frequency domain, and from 8.49 to 3.51 in the time domain. Note that final hybrid data misfit values are marginally higher than voxel inversion misfits, but the hybrid model is judged to give a clearer interpretation of the shape and dip of the conductive anomalies. Originally, the starting regularization parameter β for the voxel portion of the hybrid inversion was chosen to be 1e-3 with a cooling parameter of $\gamma = 0.2$ like in Chapter 3. However, this setup had trouble reducing the data misfit and the model update simply put diffuse conductivity zones around the central conductors with little change to the actual conductor shape. As a result, the hybrid inversions in this section use $\beta = 0$ for all Gauss-Newton iterations.

To compare the inversion models to ground truth information, Figure 4.17 displays conductive zones from the West Plains inversions in the form of a 30 Ωm iso-surface along with 1 g/t gold mineralization within the Western conductive komatiite unit. Almost no drilling exists in the Eastern conductors, and the focus shifts primarily to the Western anomaly. A rock model of the komatiite unit itself does not exist, therefore, the 1 g/t gold shape that is known to reside within

the komatiite acts as a proxy for highly conductive zones. A full model view and a closeup of the Western conductor is provided at y = 7333300 m. Figure 4.17a shows the frequency-domain voxel iso-surface, which provides a broad spatial correlation with the gold shape but no clear dip information. Figure 4.17b displays the time-domain voxel inversion iso-surface where a better sense of the dip is achieved but the anomaly is still much broader compared to the thin nature of the mineralization. The frequency and time-domain hybrid parametric inversion iso-surfaces are displayed in Figures 4.17c and 4.17d respectively. Both of these inversion demonstrate an excellent match with the compact dipping nature of the gold mineralization within the conductive komatiite, although the time-domain model achieves a slightly tighter spatial correlation.

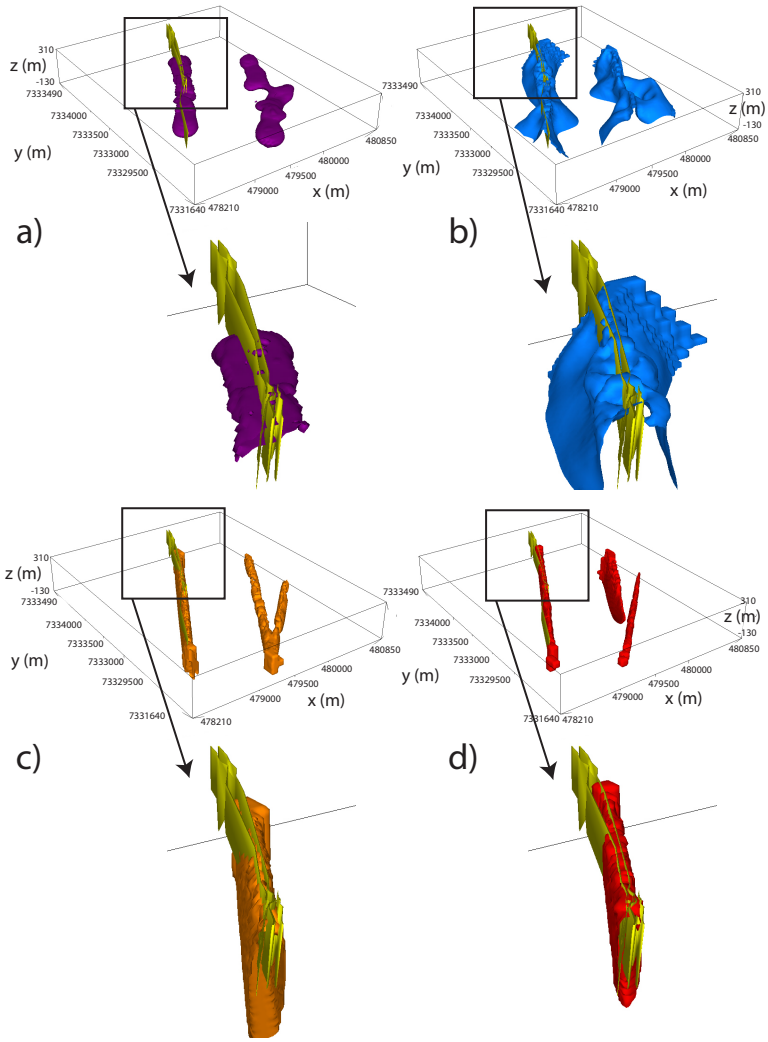

Figure 4.17: 30 Ωm iso-surfaces from voxel and hybrid inversions from West Plains field data. 1 g/t gold shapes from drilling in the West conductor are shown in yellow and correspond with the conductive komatiite unit. a) Frequency-domain voxel. b) Time-domain voxel. c) Frequency-domain hybrid parametric. d) Time-domain hybrid parametric.

4.5 Conclusions

A multiple body parametric inversion framework has been developed for frequency and time-domain AEM data with unique resistivity values. The merits of the approach are demonstrated through synthetic and field inversions where the anomalies of interest are thin dipping conductors. The targets are designed to represent a typical orogenic gold exploration setting, such as the West Plains area of the Committee Bay greenstone belt in the Canadian Arctic. The parametric inversion is coupled with a voxel approach to form a hybrid inversion in order to recover sharp targets in addition to background features. The parametric anomalies are composed of skewed Gaussian ellipsoids that can change location, radius and rotation angle in all three Cartesian planes. The synthetic example shows that the parametric stage of the hybrid inversion successfully recovers the spatial location, dip and resistivity of all three anomalies. The parametric results make interpreting the dip and depth extent of the conductors much easier compared to conventional voxel-based approaches.

In the West Plains field example, three near-vertical conductors are imaged with the parametric algorithm. The frequency and time-domain field inversions contain similarities with regards to the spatial extent of the targets in plan view and the dip of the Western conductor in cross-section, although discrepancies exist when examining the dip and depth extent of the two Eastern conductors. To achieve an improved data fit and to fill in any remaining details missed by the parametric stage, a hybrid parametric technique is employed where the parametric results are used as initial and reference models for voxel-based inversions. Final hybrid results have improved agreement with the gold mineralization from drilling compared to pure voxel inversions, and contain added detail not present within the parametric stage. Like the Caber example, no physical property information was available at West Plains for constrained inversion, but would be beneficial for future inversions.

As multiple models have been produced over a common spatial area at West Plains, it is well suited for a cooperative approach to produce one consistent model, and this topic will be addressed in Chapter 5.

Chapter 5

Cooperative Multiple Anomaly Parametric Inversion of AEM Data

In this chapter, I apply both the cooperative and parametric methods to a scenario where spatially overlapping frequency and time-domain AEM data sets exist over multiple thin dipping conductors. This approach is first tested with synthetic measurements before being applied to field data over the West Plains orogenic gold deposit. The cooperative parametric results highlight the benefits of this method when data sets are compatible and provide complementary information, but also identify potential pitfalls when data inconsistencies arise between surveys.

5.1 Introduction

The discovery of a natural resource deposit generally takes years if not decades, and over the course of that time frame, many rounds of geophysical surveys are often collected. Due to changes in technology, budget, geologic target, or a myriad of other reasons, multiple AEM data sets can be flown over the same area. Each of these data sets contains valuable information regarding the complex nature of the resistivity distribution of the target of interest. Chapter 2 introduced a cooperative technique for inverting overlapping surveys with voxel-based codes, but the

approach is equally applicable for parametric inversions where sharp anomalies are sought with large resistivity contrasts compared to the background. This setting exists at the West Plains orogenic gold deposit discussed in Chapter 4, where two overlapping frequency and time-domain AEM surveys were flown in different years over a greenstone geologic setting with multiple thin gold-bearing conductors.

The two research goals in this chapter are listed below.

- To apply the cooperative approach to a parametric inversion framework.
- To demonstrate and discuss the pros and cons of a cooperative parametric inversion with synthetic and field data.

This chapter first revisits the cooperative algorithm from Chapter 2, adding a few modifications designed for the parametric problem. The cooperative parametric method is then applied to overlapping synthetic frequency and time-domain AEM data introduced in Chapter4. Finally the process is implemented for overlapping field data at West Plains in an attempt to produce one consistent resistivity inversion model for the area. Results are compared to models from Chapter 4 and to information from drilling, and the observations are discussed.

5.2 Inversion Methodology

As shown in Figure 2.8 the voxel-based cooperative algorithm operates by iterating through each data set with a cooling schedule for the regularization parameter β, and swapping the data back and forth between inversion codes. Recall the strength of the cooperative method is its ability to rely on all possible sources of information instead of a single data set alone. However, since the parametric technique assigns $\beta = 0$, the methodology is altered slightly to iterate between data sets after a fixed number of Gauss-Newton iterations. Also, the cooperative inversion now passes parameters relating to the size and shape of the anomalies back and forth instead of conductivity values as shown in Chapter 2. How many Gauss-Newton iterations to choose depends on how well the data sets complement one another, with fewer needed if the data misfit reduces steadily after each cooperative iteration, and more if the data misfit has trouble decreasing. This research chooses to start with five

Gauss-Newton iterations for the synthetic data while a few choices are tested with field measurements. Once this number has been selected, the model swapping continues until both data sets ideally hit the target misfit or the data misfits start increasing. The cooperative parametric result can then be passed along as the initial and reference model to a voxel-based cooperative inversion where the process starts over as described in Chapter 2. The model at the end of this process is considered the final hybrid cooperative parametric model.

5.3 Synthetic Results

5.3.1 Cooperative parametric inversion

The cooperative parametric approach is tested on synthetic frequency and time-domain AEM data sets from Chapter 4, where the model consists of three dipping conductors in a resistive background. The parametric inversion, with β set to zero, begins with time-domain data, although results are similar by starting with frequency measurements. The process continues until the inversion reaches the end of the eighth cooperative iteration, when both the frequency and time-domain inversions have a higher data misfit compared to the seventh iteration. The process terminates at this point and the result after the seventh cooperative iteration is considered the final model. The data misfit progression is outlined in Figure 5.1 where two black circles represent final data misfits. For clarity, five Gauss-Newton steps are first taken for the time-domain data, numbered 1) on Figure 5.1. The parameters from this result are used as starting guesses for five Gauss-Newton steps for the frequency-domain data, numbered 2) on Figure 5.1. The parameters after the second segment are subsequently incorporated as starting values for the next five time-domain Gauss-Newton steps, as numbered 3) on Figure 5.1, and the process continues as such.

Figure 5.2a displays in plan view and cross-section the true model, Figures 5.2b and 5.2c re-shows the frequency and time-domain parametric results from Chapter 4, and Figure 5.2d portrays the cooperative parametric model. The cooperative parametric inversion produces resistivity values of 0.16 Ωm and 1.87 Ωm respectively, and the shape and dip of the anomalies represent the closest approximation

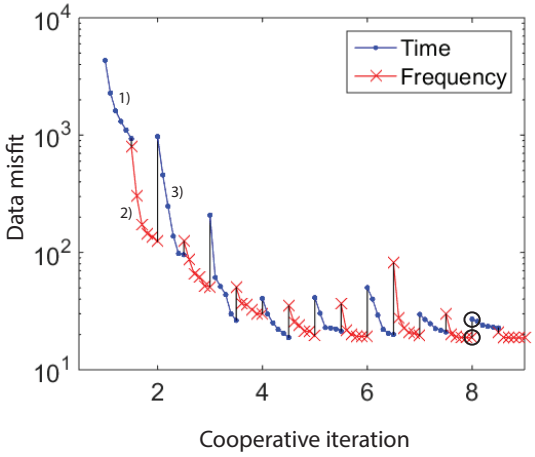

Figure 5.1: Synthetic cooperative parametric inversion data misfit progression with the final model circled in black. The first three segments are numbered for explanation purposes.

to the true model of any of the synthetic inversions. Moreover, the quantitative residual for the cooperative model is the lowest number of any inversion at $\mathbf{R_c}$ = 2.15 for the conductive cells only and $\mathbf{R_{All}}$ = 0.18 for all cells. The synthetic inversion results collectively from Chapter 4 and Chapter 5 are summarized in Table 5.1. It is worth noting a comparable number of Gauss-Newton iterations are required per data set in the cooperative approach versus the individual parametric inversions, and final data misfit levels are also similar. Altogether, it is proposed that the synthetic cooperative parametric inversion is an improvement over both individual parametric and voxel inversions.

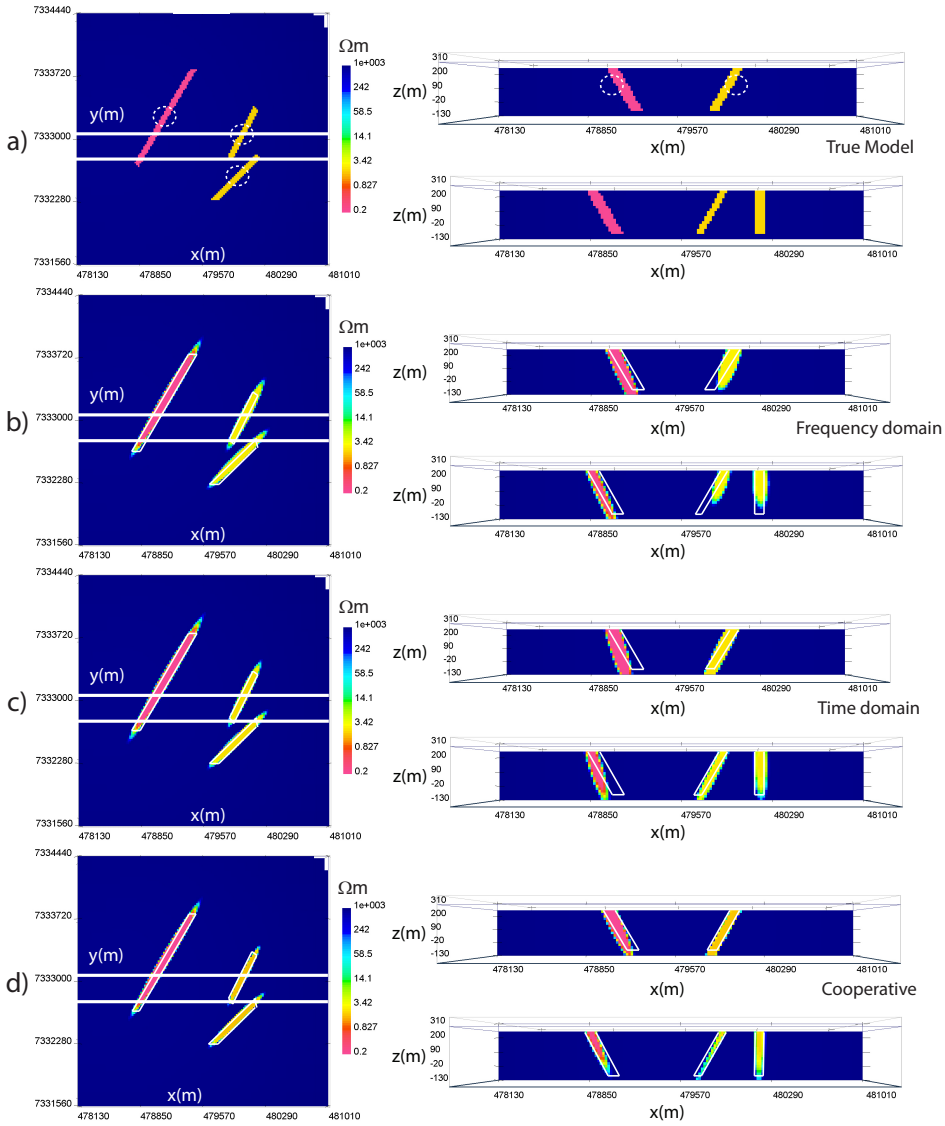

Figure 5.2: Synthetic parametric inversions in plan view at z = 250 m (left panel) and cross-section across solid white lines at y = 7333080 m and y = 7332780 m (right panel). Dashed white lines represent starting guess locations for parametric anomalies. a) True synthetic model. b) Frequency-domain parametric inversion. c) Time-domain parametric inversion. d) Cooperative parametric inversion.

Table 5.1: Synthetic data parametric inversion summary.

Inversion model	ρ_1	ρ_2	$\mathbf{R_c}$	$\mathbf{R_{All}}$	# GN	Final ϕ_d
True model	0.20 Ωm	2.00 Ωm	0.0	0.0	-	-
Parametric (freq)	0.17 Ωm	2.62 Ωm	2.18	0.26	38	19.6
Parametric (time)	0.15 Ωm	1.99 Ωm	3.33	0.31	28	17.6
Parametric (coop)	0.16 Ωm	1.87 Ωm	2.15	0.18	35	18.7 (freq)
					35	27.0 (time)

5.4 West Plains Case Study Results

5.4.1 Cooperative parametric inversions

The cooperative parametric method is now applied to West Plains AEM data introduced in Chapter 4, and once again inversion parameters are kept the same as before. However, as shown in Chapter 4, the best fitting half-spaces of 12,609 Ωm and 495 Ωm for the frequency and time-domain observations respectively suggest that a discrepancy exists between the two data sets. Not surprisingly this creates problems for the cooperative inversion, because during each cooperative iteration the inversion drastically changes the background level, which takes away from the focus of adjusting the shape of the target conductors.

From research presented in Fournier et al. (2014); McMillan et al. (2015a) and discussed further in a full paper currently in revision, an analogous discrepancy was encountered over the Tli-Kwi-Cho (TKC) diamond exploration project in the North-West Territories, Canada. At TKC, two spatially overlapping AEM data sets were flown over a kimberlite complex, a 1992 DIGHEM frequency-domain (Fountain, 1998) and a 2004 VTEM time-domain survey. Similarly to West Plains, the two AEM data sets over TKC generate best-fitting half-spaces that are an order of magnitude apart. At TKC, the frequency-domain data also produces a more resistive half-space, which corroborates the observed discrepancy seen at West Plains.

Literature states that unweathered igneous or metamorphic rock, representative of background geology at TKC and West Plains, has an average background resistivity of 10,000 Ωm (Palacky, 1988). This suggests that the frequency-domain

half-space value is more trust worthy. One possible explanation stems from the lack of transmitter waveform knowledge from 2003 or 2004 VTEM data, as the exact transmitter current used during the survey was not recorded in these years. Instead, it was presumed that the transmitter produced an ideal waveform with an electric current level of zero during the off-time. Modern systems monitor the actual transmitted waveform, which decays to zero during the early off-time. This small time-varying current produces an additional primary field that increases the observed $\frac{\partial \mathbf{b}_z}{\partial t}$ response measured by the receiver. Incorrectly assuming a current level of zero in the off-time generates a spuriously elevated conductivity level in the inversion model to compensate for the increased observed response, and would explain the background level inconsistency at West Plains and TKC.

Figure 5.3 illustrates this waveform effect. Here, $\frac{\partial \mathbf{b}_z}{\partial t}$ responses at the first five time channels from West Plains are modeled with both a practical and ideal waveform shown in Figure 5.3a. The data are modeled using a VTEM setup with the transmitter and receiver 30 m above a 1000 Ωm half-space. 3% Gaussian noise is added to the responses shown in Figure 5.3b, and it is clear that a small decaying current in the off-time shifts the response curve up significantly. Although every time-domain AEM system has a different current shut-off signature, this waveform is based off the 2012 VTEM waveform used in Chapter 3.

With this data incompatibility in mind, the cooperative parametric algorithm is altered to start with frequency-domain data, and after five Gauss-Newton iterations the best-fitting background level is fixed and the parameters are used as starting values for the time-domain data. To de-emphasize the early time channels, which are the most likely to be contaminated by waveform issues, a 20% uncertainty assignment is added to the first three channels as opposed to 3% for all others. A higher uncertainty is added to the first three time channels only, because in resistive regions, later time channels generally fall below the perceived noise threshold and are discarded. In contrast, the effect of the unknown waveform is minimized in conductive terrain as the response level is higher, and the data are deemed suitable for a lower uncertainty level. Figure 5.4a shows the data misfit progression with the final model circled in black, which illustrates that after four cooperative iterations both data misfits increase and the process stops. Even with adjustments to the background level and uncertainty assignments, the time-domain data misfit

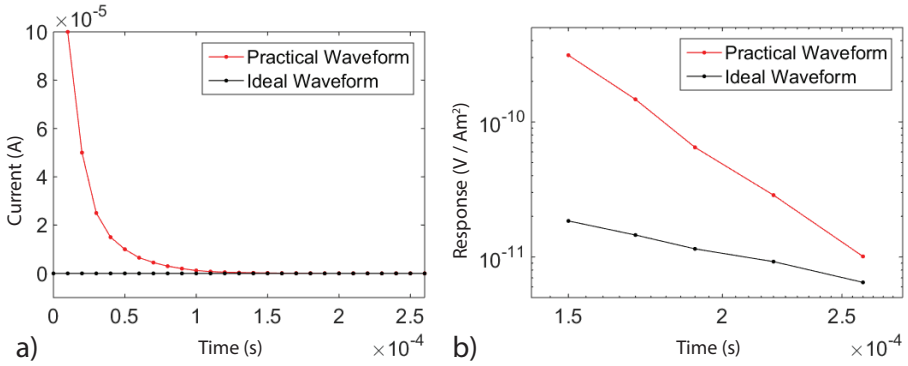

Figure 5.3: Comparison of a practical waveform with a small decaying current during early off-time $\frac{\partial \mathbf{b}_z}{\partial t}$ measurements compared to an ideal instantaneous shut-off waveform. a) Practical waveform (red) and ideal waveform (black) in early off-times. b) $\frac{\partial \mathbf{b}_z}{\partial t}$ responses at early times for the practical and ideal waveforms modeled 30 m above a 1000 Ωm half-space.

has trouble decreasing with each progressive cooperative iteration. Therefore, a second inversion is run with ten Gauss-Newton steps per cooperative iteration, and the data misfit curve is displayed in Figure 5.4b. Once again, there is no great reduction in misfit with subsequent cooperative iterations, and the process terminates after the fifth round of data swapping. It appears in this case that multiple cooperative iterations adds little value to the overall data fit, so a third trial is completed with 25 Gauss-Newton steps. This inversion terminates after only two cooperative iterations, and the data misfit graph is displayed in Figure 5.4c. Although the time-domain data misfit noticeably decreases in the first cooperative iteration, the incompatibility between data sets is evident by the extremely high initial misfit value at the start of the second frequency-domain cooperative iteration. An alternative option is to let each stage run as many Gauss-Newton iterations as possible before swapping, but this process not only takes longer to compute, but also produces a similar model to the 25 Gauss-Newton iteration case; consequently, this result is not shown.

At this point, no cooperative inversion has shown an ability to match both data

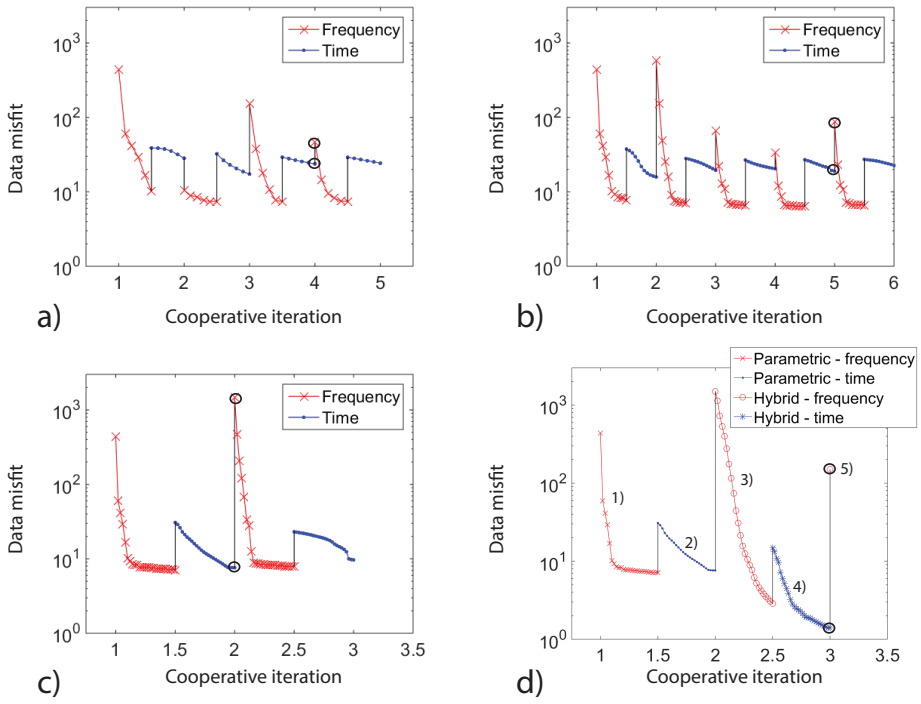

Figure 5.4: West Plains cooperative parametric inversion data misfit progressions with varying numbers of Gauss-Newton iterations per cooperative iteration. Final models circled in black. a) 5 Gauss-Newton iterations. b) 10 Gauss-Newton iterations. c) 25 Gauss-Newton iterations. d) Hybrid cooperative inversion with 25 Gauss-Newton iterations, with each segment numbered for explanation purposes.

sets sufficiently, and the relative importance of each survey must be evaluated. Frequency-domain measurements provide the best estimate for the background resistivity, but time-domain data have more time channels with a greater depth of penetration. Therefore, even with an uncertain waveform, it is deemed that fitting time-domain data will provide the most information with relation to the shape, dip and resistivity of the target conductors. With this in mind, the cooperative parametric result using 25 Gauss-Newton steps is chosen as the final parametric model since it produces the lowest time-domain data misfit.

5.4.2 Hybrid cooperative parametric inversion

A hybrid inversion is now completed using the final cooperative parametric result. This involves computing a further 25 Gauss-Newton steps for each data set with voxel-based codes. Figure 5.4d shows the data misfit progression, where every segment is numbered for clarity. The first segment represents the frequency-domain parametric stage, and the parameters after this segment are passed along as starting guesses for the time-domain parametric stage, numbered 2) on Figure 5.4d. The third segment represents the frequency-domain voxel inversion, the latter half of the hybrid method, using the parameters from the second stage. The fourth and final segment represents the time-domain voxel inversion using the result from the third segment as an initial model. After this stage, the time-domain data misfit reaches a low point of 1.56, and this is considered the final hybrid cooperative parametric model. Like in Chapter 4, the regularization parameter β is set to zero for the duration of this process and all model cells are kept active in the voxel stage. This model still does not accurately fit the frequency-domain data as shown by the subsequent initial data misfit of 150, numbered 5) on Figure 5.4d, but this is considered a consequence of incompatible data sets and the goal of fitting the time-domain measurements is deemed a success. Note that with only one cooperative iteration, this is a similar style of sequential voxel inversion as used for electromagnetic and magnetotelluric data in Commer and Newman (2009). The difference in this example is the use of a parametric algorithm to provide the initial guess for the cooperative voxel inversion.

Plan view slices and cross-sections from the cooperative parametric model are presented in Figure 5.5a and through the final hybrid cooperative parametric result in Figure 5.5b. The similarities between the parametric and hybrid models are obvious, but in plan view the hybrid approach outlines subtle concentrated areas of conductivity highs within the parametric bodies, which could be helpful to target areas of greatest mineralization. In both parametric and hybrid models, the Western conductor has a steep vertical dip and a comparable shape to individual parametric models of Chapter 4. In contrast, the Eastern conductors are both wider compared to parametric results, but the central conductor maintains a similar steep dip to the West. The Eastern conductor changes the most and possesses an elongate

near-vertical shape instead of being a near-surface compact body. This anomaly represents the most uncertain target, especially at depth, but as a whole this hybrid model can be used to make new interpretations regarding the location and dip of the Eastern conductors.

With such a high final data misfit value, it may not seem like the frequency-domain data contributes much to the cooperative process apart from the background value, but it provides a valuable starting model, making it easier to fit time-domain responses. The frequency measurements also provide near-surface information not present in the time domain data, as seen in a surficial view of the hybrid parametric model in Figure 5.5c. Once again, some caution must be taken interpreting these surface anomalies due to the poor fit of the frequency data, but there is a general correlation with these features to near-surface clay layers in lakes.

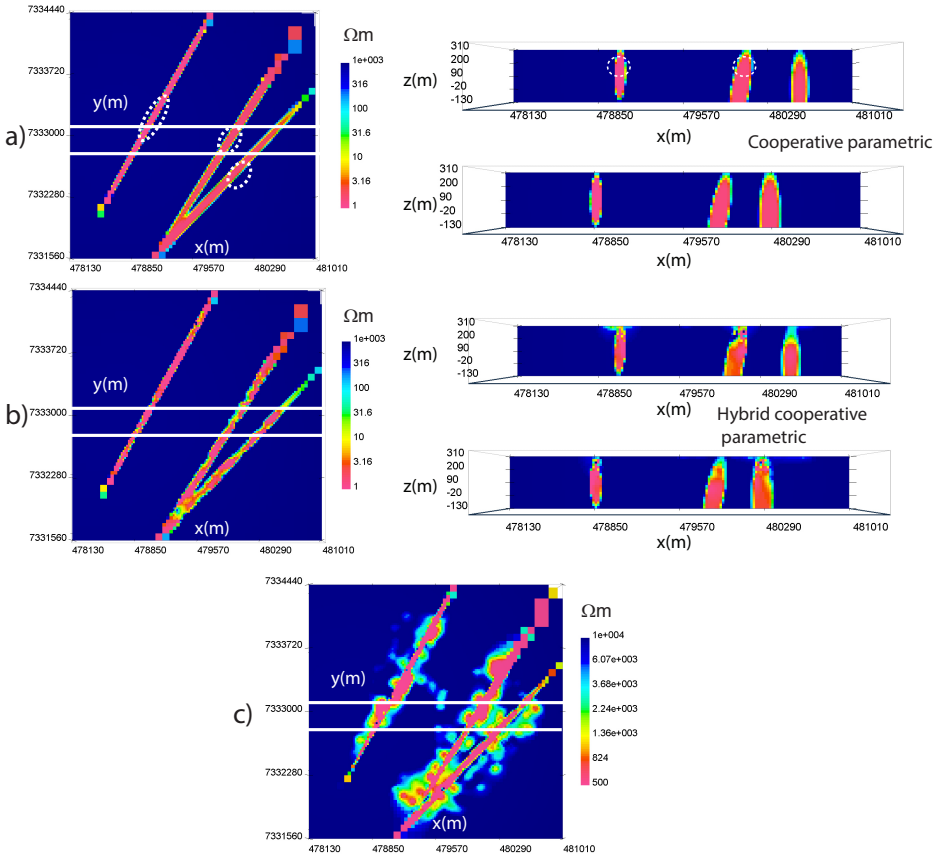

Figure 5.5: Cooperative and hybrid cooperative parametric inversions at West Plains. Dashed white lines represent starting guess locations for parametric anomalies. Plan view slices at z = 190 m (left) and cross-section across solid white lines at y = 7333080 m and y = 7332780 m (right). a) Cooperative parametric model. b) Hybrid cooperative parametric model. c) Hybrid cooperative parametric model with a plan view slice at surface.

5.5 Cooperative Inversion Discussion

The purpose of the cooperative approach is to find one consistent 3D resistivity model from two overlapping AEM data sets at West Plains, but this proved problematic as no one model matched this criteria. The incompatibility between data sets led to fixing the background resistivity at the best-fitting level derived from frequency-domain data and focusing on fitting time-domain observations thereafter. Figure 5.6a portrays the 30 Ωm iso-surface through the final hybrid cooperative parametric model. A closeup view in Figure 5.6b demonstrates a high correlation with gold mineralization within the Western komatiite. Figure 5.6c circles an area of widening in the Western conductor at an elevation slice of z = 280 m that corresponds to a zone of concentrated gold mineralization. This is highly beneficial information achieved through the hybrid approach. Finally Figure 5.6d shows the excellent correlation between the dip of the Western conductor and gold mineralization.

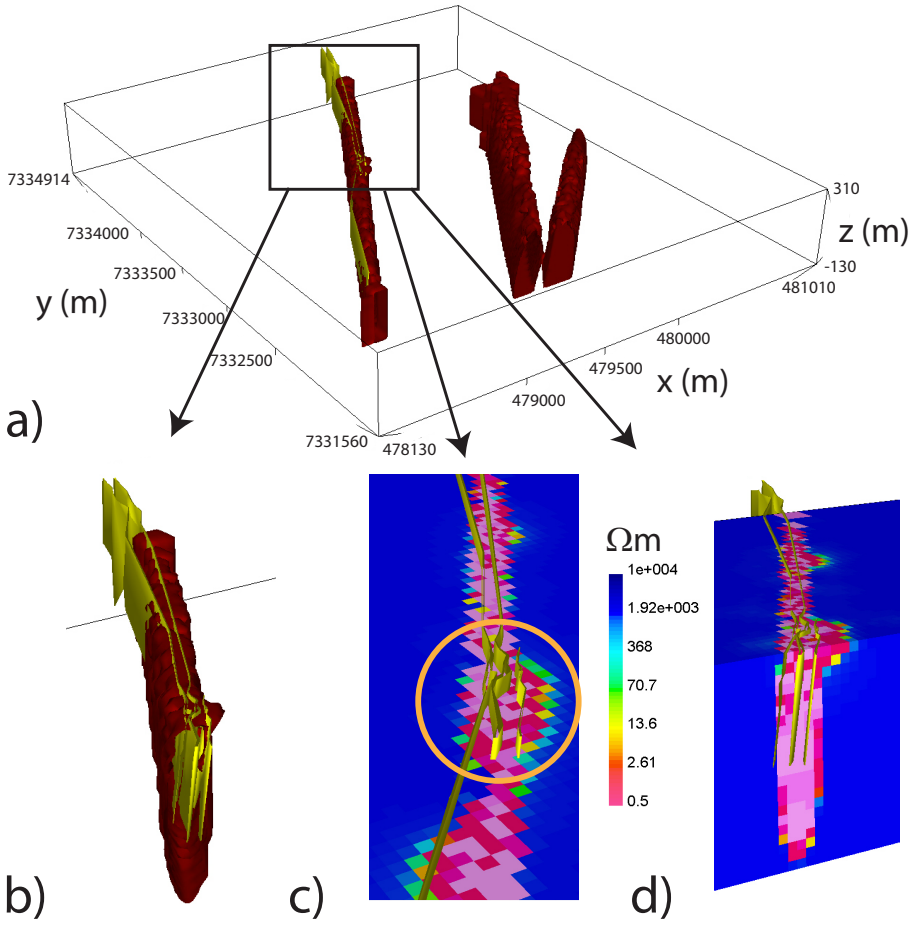

Figure 5.6: Final hybrid cooperative parametric inversion at West Plains with 1 g/t gold shapes in yellow. a) 30 Ωm iso-surface. b) Closeup view of Western conductor with 30 Ωm iso-surface. c) Closeup view of Western conductor with 280 m elevation slice. Orange circle highlights area of condensed mineralization that corresponds with a widening of the recovered conductor. d) Cross section at y = 7333230 m.

Even though the recovered model extends to a greater depth compared to the gold shapes, this deeper zone contains higher uncertainty as few drill holes reached this depth, and mineralization could extend further. Overall, the accurate correlations with gold mineralization in the Western conductor suggests that valuable interpretations can now be made regarding the Eastern conductors. To this end, a 190 m elevation slice from the final hybrid cooperative parametric model is overlaid on the simplified geology map in Figure 5.7. The recovered conductors are much thinner compared to the mapped komatiites, and new spatial outlines in plan view and cross-section can be applied to update the geology image.

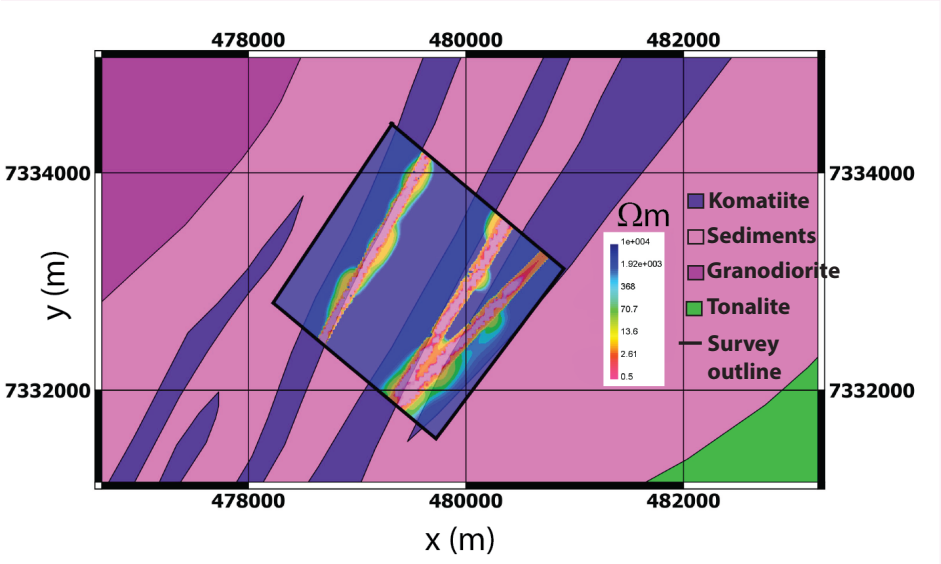

Figure 5.7: Final hybrid cooperative parametric inversion at West Plains. Elevation slice at z = 190 m overlaid on simplified geology map.

This field example is meant to demonstrate a few difficulties that can be encountered with overlapping field data that do not necessarily agree. Weighting schemes could also be applied to down-weight one data set over the other such as described in Meqbel and Ritter (2014) and Commer and Newman (2009); alternatively, an ADMM approach (Wahlberg et al., 2012) could be implemented. At West Plains, certain elements of each data set are deemed important, such as the

frequency-domain background level and time-domain information from later time channels. Finding the optimal way to treat overlapping incompatible data sets is still an open question, but this chapter sheds some light on ways to progress forward in this scenario. Fortunately, time-domain AEM data in recent years have started recording the exact waveform transmitted, and the background level issue presented here should not be as prevalent in present-day and future surveys.

5.6 Conclusions

A cooperative parametric approach is applied to spatially overlapping frequency and time-domain AEM data sets where the targets of interest are thin dipping conductors. The method is tested on both synthetic and field examples. In the synthetic example, the cooperative method produces one consistent model that achieves a closer match to the true model compared to individual parametric or voxel inversions.

In the West Plains field example, the cooperative method fails to find one model that accurately fits both data sets, and it is deemed that the overlapping AEM surveys contain incompatible measurements. This is possibly due to a small decaying current in the transmitter waveform for time-domain data during off-time measurements. The proposed solution is to use frequency-domain data to generate an initial parametric model with a best-fitting background resistivity, and to fix this background level for the time-domain parametric inversion stage. This process is then repeated with voxel based algorithms to produce a final hybrid cooperative parametric model.

The corresponding agreement to gold mineralization is excellent, and new interpretations can now be made with regards to the shape of the Eastern conductors. Although this is perceived to be the best possible model from this data, it is acknowledged that the final data fit on the frequency-domain data is still poor and more research is needed to fully rectify this discrepancy.

Chapter 6

Conclusions

Airborne electromagnetic data remains one of the most commonly used tools for geophysical exploration as a means to image the subsurface of the earth. This method is sensitive to contrasts in electrical resistivity, which can be used to help locate and characterize buried natural resources such as metal, water and oil. While surveys have been flown for decades, 3D AEM inversion is a relatively new and rapidly developing field. As such, I designed this thesis to contribute to the scientific community by advancing 3D AEM inversion accuracy over a wide range of geologic environments. In particular, I present practical strategies that address two important and unresolved questions.

1. How to improve 3D AEM inversion with spatially overlapping surveys.

2. How to improve 3D AEM inversion to recover thin, high contrast anomalies.

The following sections summarize the findings of this thesis followed by a discussion on future research questions.

6.1 Cooperative Inversion

In Chapter 2 I investigated the first topic listed above, and looked at how to invert multiple overlapping electromagnetic data sets to produce one consistent 3D resistivity model that satisfied all geophysical observations. Three overlapping field data sets, time-domain AEM, CSAMT and DC, were examined over the Antonio

high-sulfidation epithermal deposit in Peru. After comparing inversion results from each individual data set, I found that resulting models contained many discrepancies in their resistivity distributions. This phenomenon was studied in more detail through a synthetic example which was designed to emulate the geology at Antonio with a large resistor that hosted two buried conductors. The individual synthetic inversions were able to recover similar looking resistive regions, but the detection of the contained conductive bodies varied greatly. A cooperative approach was subsequently developed, where the inversion iterated between data sets and constructed a result that satisfied all geophysical information provided. This method created one consistent 3D model that successfully imaged the resistive region as well as the conductive bodies to a closer degree to the true model compared to any individual inversion.

Following the success of the synthetic example, I applied the cooperative technique to the Antonio field data and generated a common physical property model that mapped a large gold-bearing silica-rich resistor interspersed with smaller conductive zones. The final cooperative model resolved this resistive region with a high level of agreement compared to known silica alteration from drilling and geologic mapping, and highlighted small conductive regions that could be indicative of sulfide and gold mineralization. These inferences represented new potential targets of interest at this project, and showed the applicability of the cooperative approach to a field setting. This chapter also demonstrated how physical property information derived from drill holes assisted in constraining both the synthetic and field cooperative inversion models through upper and lower resistivity bounds. This showed that drill hole information should be incorporated into cooperative inversions when available.

6.2 Parametric Inversion - Single Anomaly

Chapter 3 addressed the second thesis topic of how to improve 3D AEM inversion over thin conductive targets. Here I developed a parametric solution where the algorithm recovered a single anomaly in the shape of a best-fitting skewed Gaussian ellipsoid that represented the target of interest in a smooth background. The method was first tested on a synthetic example composed of a thin conductive

plate-like anomaly in a uniform resistive background, and the parametric method was able to recover the target to a much higher degree of accuracy compared to a purely voxel-based solution.

The approach was then applied to time-domain AEM field data over the Caber volcanogenic massive sulfide deposit in Quebec where the parametric inversion model was able to replicate the thin dipping nature of the copper-zinc resource as defined by drilling. The Caber parametric model was subsequently used as a reference model for a voxel-based inversion to fill in missing features such as a conductive overburden layer. The hybrid parametric inversion was designed to combine elements from both parametric and voxel methods, and this proved beneficial to map out the Caber target in addition to relevant surrounding geology.

6.3 Parametric Inversion - Multiple Anomalies

In Chapter 4 I modified the parametric framework to include multiple skewed Gaussian ellipsoids with individual resistivity values. This extension made the parametric approach suitable for a wider range of geologic settings and target styles. The multiple anomaly parametric code was first tested on synthetic frequency and time-domain AEM data over three narrow dipping conductors in a resistive background. This synthetic model was built to replicate an orogenic gold exploration setting such as the West Plains area of the Committee Bay greenstone belt in Nunavut. The synthetic results recovered the shape, dip and resistivity value of the dipping conductors with excellent precision, and made interpreting the models much simpler compared to voxel-based inversions.

The technique was subsequently tested on the West Plains frequency and time-domain AEM field data, and recovered three narrow, elongate, near-vertical conductors. The Western anomaly from both parametric models displayed a high level of correlation to the shape and dip of gold mineralization hosted in a conductive komatiite unit known from drilling, and managed to depict its thin nature with greater ease compared to conventional voxel inversions. The Eastern conductors were less consistent between the parametric models and were not as thoroughly evaluated since little ground truth was available in this area. I applied the hybrid approach to the parametric field results which helped fit the observed data to a higher degree

and added near-surface features not possible with a parametric method alone. The hybrid inversion also generated concentrated areas of conductivity within the target anomalies, which could be valuable to detect high grade mineralization.

6.4 Cooperative Parametric Inversion

For Chapter 5 I combined the cooperative and parametric methods for spatially overlapping AEM data sets. This approach saw improved inversion accuracy with synthetic data, but encountered issues with incompatible field data. With synthetic data from Chapter 4, the cooperative parametric result imaged three dipping conductors with greater precision compared to individual parametric inversions. The latter were already a close approximation to the synthetic model, but the cooperative method was able to extract additional information and created subtle improvements. As these data were computer generated, they represented a test example with perfectly calibrated and compatible data.

The cooperative parametric algorithm was subsequently tested on overlapping frequency and time-domain AEM field measurements at West Plains, and it became quickly apparent that the data sets were incompatible and did not provide fully complementary information. The biggest discrepancy came in the form of the best-fitting recovered background resistivity, where the frequency observations produced a highly resistive value and the time-domain data suggested a much more conductive background. A similar inconsistency was previously identified at the TKC kimberlite deposit in the Canadian Arctic with comparable AEM systems. It is postulated to be caused from the time-domain transmitter possessing an unknown non-zero decaying current level during the system off-time. Consequently, it was determined that the frequency-domain data produced the more accurate background value and this was fixed for time-domain iterations.

The final hybrid cooperative parametric model at West Plains imaged the Western conductor with excellent agreement to drilling information, and was able to isolate areas of high conductivity within the Western conductor that corresponded with areas of concentrated gold mineralization. Similar interpretations can now be made for the shape and dip of the two Eastern conductors where little drilling knowledge exists. However, as the surveys were deemed incompatible, the final

model was unable to fit both data sets, and in this example the priority was given to time-domain measurements. This was due to more available time channels compared to frequencies coupled with a greater depth of penetration. However, the frequency-domain data were still beneficial for providing the background value and near-surface features. Collectively this chapter showed that a hybrid cooperative parametric method can be advantageous when the observations provide complementary information, but caution must be taken when compatibility issues arise between data sets.

6.5 Future Research

In this thesis I have introduced practical cooperative and parametric strategies for 3D AEM inversion, both in the frequency and time domain, but further research is needed to optimize algorithm robustness and efficiency. The ADMM method (Wahlberg et al., 2012) would be worthwhile testing for multiple spatially overlapping data sets and comparing the results against the cooperative algorithm presented. In terms of the parametric algorithm, future trials should raise the complexity level of the target geometry to push the limits of the inversion capability. It will be important to include small-scale compact targets and also large-scale smoothly varying features to thoroughly test the hybrid parametric method. Multiple data sets can be synthetically generated over these complex models to test the hybrid cooperative parametric method, and additional field data sets should be sought for practical applications. These future trials should incorporate alternative parameterizations such as multiple spheres and potentially other relevant shapes in order to evaluate a broad scope of parametric methods. Finally this dissertation has focused on airborne electromagnetic data but the cooperative and parametric strategies developed are designed to be general, and are equally applicable to ground EM measurements, potential field or induced-polarization surveys.

Bibliography

Abubakar, A., T. M. Habashy, V. Druskin, L. Knizhnerman, and S. Davydycheva, 2006, A 3D parametric inversion algorithm for triaxial induction data: Geophysics, **71**, G1–G9. → pages 44

Adair, R., 2011, Technical Report on the Resource Calculation for the Matagami Project , Québec: Technical report. → pages xiv, 63, 64

Aghasi, A., M. Kilmer, and E. L. Miller, 2011, Parametric Level Set Methods for Inverse Problems: SIAM Journal on Imaging Sciences, **4**, 618–650. → pages 44, 45, 60, 129

Albouy, Y., P. Andrieux, G. Rakotondrasoa, M. Ritz, M. Descloitres, J.-L. Join, and E. Rasolomanana, 2001, Mapping coastal aquifers by joint inversion of DC and TEM soundings-three case histories: Groundwater, **39**, 87–97. → pages 11

Allard, M., 2007, On the Origin of the HTEM Species in B. Milkereit ed.: Proceedings of Exploration 07: Fifth Decennial International Conference on Mineral Exploration, 355–374. → pages 19, 46, 56, 65, 78, 81

Arribas, A., 1995, Characteristics of high-sulfidation epithermal deposits, and their relation to magmatic fluid: Mineralogical Association of Canada Short Course Series, **23**, 419–454. → pages 16

Ascher, U., and F. Roosta-khorasani, 2016, Algorithms that Satisfy a Stopping Criterion , Probably: Vietnam Journal of Mathematics, **44**, 49–69. → pages 44

Bezanson, J., S. Karpinski, V. B. Shah, and A. Edelman, 2012, Julia: A Fast Dynamic Language for Technical Computing: arXiv preprint arXiv:1209.5145. → pages 10

Boyko, W., S. Balch, and N. Paterson, 2003, The AeroTEM airborne electromagnetic system: The Leading Edge, **22**, 562–566. → pages 4, 81

Carr, P. M., L. M. Cathles III, and C. T. Barrie, 2008, On the size and spacing of volcanogenic massive sulfide deposits within a district with application to the Matagami district, Quebec: Economic Geology, **103**, 1395–1409. → pages 63

Carson, C. J., R. G. Berman, R. A. Stern, M. Sanborn-barrie, T. Skulski, and H. A. I. Sandeman, 2004, Age constraints on the Paleoproterozoic tectonometamorphic history of the Committee Bay region , western Churchill

Province , Canada : evidence from zircon and in situ monazite SHRIMP geochronology: Canadian Journal of Earth Sciences, **41**, 1049–1076. → pages 87

Caudillo-Mata, L. A., E. Haber, and C. Schwarzbach, 2016, An oversampling technique for the multiscale finite volume method to simulate electromagnetic responses in the frequency domain: arXiv preprint arXiv:1610.02105, 1–15. → pages 26

Chen, T., G. Hodges, and P. Miles, 2015, MULTIPULSE high resolution and high power in one TDEM system: Exploration Geophysics, **46**, 49–57. → pages 4

Commer, M., and G. A. Newman, 2004, A parallel finite-difference approach for 3D transient electromagnetic modeling with galvanic sources: Geophysics, **5**, 1192–1202. → pages 7

———, 2009, Three-dimensional controlled-source electromagnetic and magnetotelluric joint inversion: Geophysical Journal International, **178**, 1305–1316. → pages 10, 15, 109, 114

Constable, S. C., R. L. Parker, and C. G. Constable, 1987, Occam's inversion: A practical algorithm for generating smooth models from electromagnetic sounding data: Geophysics, **52**, 289–300. → pages 9

Cox, L. H., G. A. Wilson, and M. S. Zhdanov, 2010, 3D inversion of airborne electromagnetic data using a moving footprint: Exploration Geophysics, **41**, 250–259. → pages 7, 9

———, 2012, 3D inversion of airborne electromagnetic data: Geophysics, **77**, WB59–WB69. → pages 9, 10, 43

Dorn, O., and D. Lesselier, 2006, Level set methods for inverse scattering: Inverse Problems, **22**, R67–R131. → pages 44, 60

Dorn, O., E. L. Miller, and C. M. Rappaport, 2000, A shape reconstruction method for electromagnetic tomography using adjoint fields and level sets: Inverse Problems, **16**, 1119–1156. → pages 44

Eaton, P., 1998, Application of an improved technique for interpreting transient electromagnetic data: Exploration Geophysics, **29**, 175–183. → pages 9

Eaton, P. A., R. G. Anderson, S. V. Queen, B. Y. Nilsson, E. Lauritsen, C. T. Barnett, M. Olm, and S. Mitchell, 2013, Helicopter time-domain electromagnetics - Newmont and the NEWTEM experience: Geophysics, **6**, W45–W56. → pages 4, 19, 81

Egbert, G. D., and A. Kelbert, 2012, Computational recipes for electromagnetic inverse problems: Geophysical Journal International, **189**, 251–267. → pages 7

Ekblom, H., 1973, Calculation of linear best Lp approximations: BIT Numerical Mathematics, **13**, 292–300. → pages 8, 57

EMIT, 2005, Maxwell 4.0: Modeling, presentation and visualization of EM and electrical geophysical data: Technical report. → pages 11, 66

Farquharson, C. G., and D. W. Oldenburg, 1998, Non-linear inversion using general measures of data misfit and model structure: Geophysical Journal International, **134**, 213–227. → pages 44

Farquharson, G., and D. W. Oldenburg, 1993, Inversion of time-domain electromagnetic data for a horizontally layered Earth: Geophysical Journal International, **114**, 433–442. → pages 9

Fountain, D., 1998, Airborne electromagnetic systems - 50 years of development: Exploration Geophysics, **29**, 1–11. → pages 105

Fournier, D., 2015, A Cooperative Magnetic Inversion Method With Lp-norm Regularization: PhD thesis. → pages 8, 44

Fournier, D., L. Heagy, N. Corcoran, D. Cowan, S. G. R. Devriese, D. Bild-enkin, K. Davis, S. Kang, D. Marchant, M. S. McMillan, M. Mitchell, G. Rosenkjar, and D. Yang, 2014, Multi-EM systems inversion - Towards a common conductivity model for the Tli Kwi Cho complex: 84th Annual International Meeting, SEG, Expanded Abstracts, **33**, 1795–1799. → pages 105

Fraser, D. C., 1978, Resistivity mapping with an airborne multicoil electromagnetic system: Geophysics, **43**, 144–172. → pages 9

Gallardo, L. A., and M. A. Meju, 2004, Joint two-dimensional DC resistivity and seismic travel time inversion with cross-gradients constraints: Journal of Geophysical Research, **109**, B03311. → pages 11

Gill, P. E., W. Murray, and M. H. Wright, 1981, Practical Optimization: Academic Press Inc. → pages 48

Goldie, M. K., 2000, A geophysical case history of the Yanacocha gold district, northern Peru: 70th Annual International Meeting, SEG, Expanded Abstracts. → pages 17, 18

Haber, E., and U. M. Ascher, 2001, Fast finite volume simulation of 3D electromagnetic problems with highly discontinuous coefficients: Siam Journal of Scientific Computing, **22**, 1943–1961. → pages 80

Haber, E., U. M. Ascher, and D. W. Oldenburg, 2004, Inversion of 3D electromagnetic data in frequency and time domain using an inexact all-at-once approach: Geophysics, **69**, 1216–1228. → pages 23, 46

Haber, E., and S. Heldmann, 2007, An octree multigrid method for quasi-static Maxwell's equations with highly discontinuous coefficients: Journal of Computational Physics, **223**, 783–796. → pages 46

Haber, E., S. Heldmann, and U. Ascher, 2007a, Adaptive finite volume method for distributed non-smooth parameter identification: Inverse Problems, **23**, 1659–1676. → pages 22, 46

Haber, E., D. W. Oldenburg, and R. Shekhtman, 2007b, Inversion of time domain three-dimensional electromagnetic data: Geophysical Journal International, **171**, 550–564. → pages 7, 46

Haber, E., and C. Schwarzbach, 2014, Parallel inversion of large-scale airborne time-domain electromagnetic data with multiple OcTree meshes: Inverse Problems, **30**, 1–28. → pages 7, 9, 10, 19, 22, 23, 43, 46, 48, 51, 52, 57

Hoschke, T., 2011, Geophysical signatures of copper-gold porphyry and epithermal gold deposits, and implications for exploration: PhD thesis, University of Tasmania. → pages xi, 17

Isakov, V., S. Leung, and J. Qian, 2011, A Fast Local Level Set Method for Inverse Gravimetry 1 Introduction: Communications in Computational Physics, **10**, 1044–1070. → pages 44

Keating, P. B., and D. J. Crossley, 1990, The inversion of time-domain airborne electromagnetic data using the plate model: Geophysics, **55**, 705–711. → pages 11

Keller, G. V., 1988, Rock and mineral properties: Electromagnetic methods in applied geophysics, **1**, 13–52. → pages 2, 43

Kerswill, J. A., 1996, Iron-formation-hosted stratabound gold: Geology of Canadian mineral deposit types. Geology of Canada, **8**, 367–382. → pages 77

Key, K., and C. Weiss, 2006, Adaptive finite-element modeling using unstructured grids: The 2D magnetotelluric example: Geophysics, **71**, G291–G299. → pages 7, 10

Kunetz, G., 1966, Principles of direct current resistivity prospecting: Gebruder Borntraeger, Berlin. → pages 4

Last, B. J., and K. Kubik, 1983, Compact gravity inversion: Geophysics, **6**, 713–721. → pages 8, 44

Lelièvre, P. G., and D. W. Oldenburg, 2009, A comprehensive study of including structural orientation information in geophysical inversions: Geophysical Journal International, **178**, 623–637. → pages 11

Lelièvre, P. G., D. W. Oldenburg, and N. C. Williams, 2009, Integrating geological and geophysical data through advanced constrained inversions *: Exploration Geophysics, **40**, 334–341. → pages 11

Li, Y., and K. Key, 2007, 2D marine controlled-source electromagnetic modeling : Part 1 An adaptive finite-element algorithm: Geophysics, **72**, WA51–WA62. → pages 7

Li, Y., and D. W. Oldenburg, 2000, Incorporating geological dip information into geophysical inversions: Geophysics, **65**, 148–157. → pages 11

Lines, L. R., A. K. Schultz, and S. Treitel, 1988, Cooperative inversion of geophysical data: Geophysics, **53**, 8–20. → pages 10, 15

Loayza, C., and J. Reyes, 2010, Geologic overview of the Yanacocha mining district: Presented at the SIMEXMIN10 - IV Brazilian symposium of mineral exploration. → pages 17

Lu, W., and J. Qian, 2015, A local level-set method for 3D inversion of

gravity-gradient data: Geophysics, **80**, G35–G51. → pages 44
Macnae, J., A. King, A. Osmakoff, and A. Blaha, 1998, Fast AEM data processing and inversion: Exploration Geophysics, **29**, 163–169. → pages 9
Macnae, J., and Y. Lamontagne, 1987, Imaging quasi-layered conductive structures by simple processing of transient electromagnetic data: Geophysics, **52**, 545–554. → pages 9
Macnae, J. C., R. Smith, B. D. Polzer, Y. Lamontagne, and P. S. Klinkert, 1991, Conductivity-depth imaging of airborne electromagnetic step-response data: Geophysics, **56**, 102–114. → pages 3, 9
McMillan, M. S., and D. W. Oldenburg, 2012, Three-dimensional electromagnetic and electrical inversions over the Antonio gold deposit in Peru: 82nd Annual International Meeting, SEG, Expanded Abstracts, **31**, 1316–1320. → pages iv
———, 2014, Cooperative constrained inversion of multiple electromagnetic data sets: Geophysics, **79**, B173–B185. → pages iv, xi, 16
McMillan, M. S., D. W. Oldenburg, E. Haber, and C. Schwarzbach, 2015a, Parametric 3D inversion of airborne time domain electromagnetics: ASEG Expanded Abstracts, 1–5. → pages 70, 105
McMillan, M. S., D. W. Oldenburg, E. Haber, C. Schwarzbach, and E. Holtham, 2015b, 3D Multiple Body Parametric Inversion of Time-domain Airborne EM Data: First European Airborne Electromagnetics Conference, 1–4. → pages iv
McMillan, M. S., C. Schwarzbach, E. Haber, and D. W. Oldenburg, 2015c, 3D parametric hybrid inversion of time-domain airborne electromagnetic data: Geophysics, **80**, K25–K36. → pages iv
———, 2016, 3D Cooperative Parametric Inversion of Frequency and Time-domain Airborne Electromagnetic Data: Presented at the First Conference on Geophysics for Mineral Exploration and Mining. → pages v
McMillan, M. S., C. Schwarzbach, D. W. Oldenburg, E. Haber, E. Holtham, and A. Prikhodko, 2014, Recovering a thin dipping conductor with 3D electromagnetic inversion over the Caber deposit: 84th Annual International Meeting, SEG, Expanded Abstracts, **33**, 1720–1724. → pages iv
Meqbel, N., and O. Ritter, 2014, New Advances for a Joint 3D Inversion of Multiple EM Methods: 76th EAGE Conference and Exhibition-Workshops, 1–4. → pages 114
Modersitzki, J., 2003, Numerical Methods for Image Registration: Oxford university press. → pages 49
Mulè, S., R. Miller, H. Carey, and R. Lockwood, 2012, Review of three airborne EM systems: ASEG Expanded Abstracts, 26–29. → pages 4, 81
Nabighian, M. N., and J. C. Macnae, 1991, Time domain electromagnetic prospecting methods: Electromagnetic methods in applied geophysics, **2**, 427–479. → pages 9, 20

Nelson, P. H., and G. D. Van Voorhis, 1983, Estimation of sulfide content from induced polarization data: Geophysics, **48**, 62–75. → pages 38

Oldenburg, D. W., R. A. Eso, S. Napier, and E. Haber, 2005, Controlled source electromagnetic inversion for resource exploration: First Break, **23**, 41–48. → pages 17, 23, 39

Oldenburg, D. W., E. Haber, and R. Shekhtman, 2013, Three dimensional inversion of multisource time domain electromagnetic data: Geophysics, **78**, E47–E57. → pages 7, 9, 44, 80

Oldenburg, D. W., and Y. Li, 1994, Inversion of induced-polarization data: Geophysics, **59**, 1327–1341. → pages 23

Oldenburg, D. W., Y. Li, and R. G. Ellis, 1997, Inversion of geophysical data over a copper gold porphyry deposit : A case history for Mt. Milligan: Geophysics, **62**, 1419–1431. → pages 10, 11, 15

Oldenburg, D. W., R. Shehktman, R. A. Eso, C. G. Farquharson, P. Eaton, B. Anderson, and B. Bolin, 2004, Closing the gap between research and practice in EM data interpretation: 74th Annual International Meeting, SEG, Expanded Abstracts, **23**, 1179–1183. → pages 23, 39

Osher, S., and R. P. Fedkiw, 2001, Level Set Methods: An Overview and Some Recent Results: Journal of Computational Physics, **169**, 463–502. → pages 44

Osher, S., and J. A. Sethian, 1988, Fronts Propagating with Curvature- Dependent Speed : Algorithms Based on Hamilton-Jacobi Formulations: Journal of Computational Physics, **79**, 12–49. → pages 44, 51, 75

Palacky, G. J., 1988, Resistivity Characteristics of Geologic Targets: Electromagnetic methods in applied geophysics, **1**, 53–129. → pages 66, 105

Palacky, G. J., and G. F. West, 1973, Quantitative interpretation of AEM measurements: Geophysics, **38**, 1145–1158. → pages 3, 9

Pidlisecky, A., K. Singha, and F. D. Day-Lewis, 2011, A distribution-based parametrization for improved tomographic imaging of solute plumes: Geophysical Journal International, **187**, 214–224. → pages 45, 129

Portniaguine, O., and M. S. Zhdanov, 1999, Focusing geophysical inversion images: Geophysics, **64**, 874–887. → pages 8, 44

Prikhodko, A., T. Eadie, N. Fiset, and L. Mathew, 2012, VTEM (35 m) test results over the Caber and Caber North Deposits (October 2012): Technical report. → pages xiv, 66, 69, 71

Prikhodko, A., E. Morrison, A. Bagrianski, P. Kuzmin, P. Tishin, and J. Legault, 2010, Evolution of VTEM technical solutions for effective exploration: ASEG Expanded Abstracts, **1**, 1–4. → pages xiv, 63, 64

Raiche, A., 1998, Modelling the time-domain response of AEM systems: Exploration Geophysics, **29**, 103. → pages 11, 44

Raiche, A. P., D. L. B. Juppt, H. Rutter, and K. Vozoff, 1985, The joint use of

coincident loop transient electromagnetic and Schlumberger sounding to resolve layered structures: Geophysics, **50**, 1618–1627. → pages 9

Ruthotto, L., E. Treister, and E. Haber, 2016, Jinv a flexible julia package for pde parameter estimation: arXiv preprint arXiv:1606.07399, 1–19. → pages 7, 9, 10, 44

Schwarzbach, C., and E. Haber, 2013, Finite element based inversion for time-harmonic electromagnetic problems: Geophysical Journal International, **193**, 615–634. → pages 7

Skulski, T., H. A. I. Sandeman, and M. Sanborn-barrie, 2003, Bedrock geology of the Ellice Hills map area and new constraints on the regional geology of the Committee Bay area: Natural Resources Canada, Geological Survey of Canada, 1–11. → pages 87

Smith, R., D. Fountain, and M. Allard, 2003, The MEGATEM fixed-wing transient EM system applied to mineral exploration: A discovery case history.: First Break, **21**, 73–77. → pages 81

Sørensen, K. I., and E. Auken, 2004, SkyTEM a new high-resolution helicopter transient electromagnetic system: Exploration Geophysics, **35**, 194–202. → pages 81

Sosa, A., A. A. Velasco, L. Velazquez, M. Argaez, and R. Romero, 2013, Constrained optimization framework for joint inversion of geophysical data sets: Geophysical Journal International, **195**, 1745–1762. → pages 11

Steklova, K., and E. Haber, 2016, Joint hydrogeophysical inversion: state estimation for seawater intrusion models in 3D: Computational Geosciences, 1–20. → pages 10

Sturler, E. D. E., and M. E. Kilmer, 2011, A regularized GaussNewton trust region approach to imaging in optical tomography: Siam Journal of Scientific Computing, **33**, 3057–3086. → pages 51

Tai, X.-c., and T. F. Chan, 2004, A survey on multiple level set methods with applications for identifying piecewise constant functions: International Journal of Numerical Analysis and Modeling, **1**, 25–47. → pages 51, 75

Teal, L., and A. Benavides, 2010, History and geologic overview of the Yanacocha mining district, Cajamarca, Peru: Economic Geology, **105**, 1173–1190. → pages 16, 17

van den Doel, K., and U. Ascher, 2006, On level set regularization for highly ill-posed distributed parameter estimation problems: Journal of Computational Physics, **216**, 707–723. → pages 44, 60

Viezzoli, A., E. Auken, and T. Munday, 2009, Spatially constrained inversion for quasi 3D modelling of airborne electromagnetic data an application for environmental assessment in the Lower Murray Region of South Australia: Exploration Geophysics, **40**, 173–183. → pages 78

Vozoff, K., and D. L. B. Jupp, 1975, Joint inversion of geophysical data: Geophysical Journal of the Royal Astronomical Society, **42**, 977–991. → pages 11

Wahlberg, B., S. Boyd, M. Annergren, and Y. Wang, 2012, An ADMM Algorithm for a Class of Total Problems: arXiv preprint arXiv:1203.1828, 1–6. → pages 10, 114, 120

Ward, S. H., and G. W. Hohmann, 1988, Electromagnetic theory for geophysical applications: Electromagnetic methods in applied geophysics, **1**, 131–311. → pages 20

Weiss, C. J., and S. Constable, 2006, Mapping thin resistors and hydrocarbons with marine EM methods , Part II Modeling and analysis in 3D: Geophysics, **71**, G321–G332. → pages 7

Williams, N., D. Oldenburg, and P. Lelièvre, 2009, Constraining gravity and magnetics inversions for mineral exploration using limited geological data: ASEG Expanded Abstracts. → pages 11

Wilson, G. A., A. Raiche, and F. Sugeng, 2006, 2.5D inversion of airborne electromagnetic data: Exploration Geophysics, **37**, 363–371. → pages 9

Xiong, Z., and A. C. Tripp, 1995, A block iterative algorithm for 3D electromagnetic modeling using integral equations with symmetrized substructures: Geophysics, **60**, 291–295. → pages 11, 44

Yang, D., D. W. Oldenburg, and E. Haber, 2014, 3-D inversion of airborne electromagnetic data parallelized and accelerated by local mesh and adaptive soundings.: Geophysical Journal International, **196.3**, 1492–1507. → pages 9

Zhdanov, M. S., 2010, Electromagnetic geophysics : Notes from the past and the road ahead: Geophysics, **75**, 75A49–75A66. → pages 7

Zhdanov, M. S., and L. H. Cox, 2013, Multinary Inversion for Tunnel Detection: IEEE Geoscience and Remote Sensing Letters, **10**, 1100–1103. → pages 44

Zheglova, P., and C. Farquharson, 2016, Joint level set inversion of gravity and travel time data : application to mineral exploration: 86th Annual International Meeting, SEG, Expanded Abstracts, **35**, 2165–2169. → pages 44, 60

Zonge, K. L., and L. J. Hughes, 1991, Controlled source audio-frequency magnetotellurics: Electromagnetic methods in applied geophysics, **2**, 713–809. → pages 4, 20

Appendix A

Multiple Sphere Parametric Inversion

A.1 Introduction

Here I introduce a multiple sphere parameterization for AEM data as a way to complement the Gaussian ellipsoid approach discussed in this dissertation. This is meant to demonstrate the flexibility of the developed parametric framework and to emphasize how various shape choices are available. The reader is also encouraged to see Aghasi et al. (2011); Pidlisecky et al. (2011) for discussions about other shape reconstructions.

A.2 Sphere Parameterization

A sphere is a simplified shape compared to a Gaussian ellipsoid, because although the radius and central location of the sphere can change, it can not stretch or rotate. This means that fewer parameters are needed to describe a sphere compared to an ellipsoid, with the obvious drawback of a reduction in shape flexibility.

Mathematically, the transition in the parametric algorithm from multiple Gaussian ellipsoids to multiple spheres is straight forward. For positions x, y, z in the spatial domain, define a position vector $\mathbf{x}$ and a central location vector $\mathbf{x}_{0(n)}$ for the

n^{th} anomaly as in Equation 4.2

$$\mathbf{x} = \begin{pmatrix} x \\ y \\ z \end{pmatrix} \quad \mathbf{x}_{0(n)} = \begin{pmatrix} x_{0(n)} \\ y_{0(n)} \\ z_{0(n)} \end{pmatrix}. \tag{A.1}$$

The parametric function τ_n is once again defined as

$$\tau_n = c - (\mathbf{x} - \mathbf{x}_{0(n)})^{\mathbf{T}} \mathbf{M}_n (\mathbf{x} - \mathbf{x}_{0(n)}) \tag{A.2}$$

but the former skewing matrix $\mathbf{M}_n$ is now a diagonal matrix with the inverse of the squared sphere radius, r, on the diagonal

$$\mathbf{M}_n = \begin{pmatrix} \frac{1}{r^2} & 0 & 0 \\ 0 & \frac{1}{r^2} & 0 \\ 0 & 0 & \frac{1}{r^2} \end{pmatrix}. \tag{A.3}$$

Each sphere can be given its own radius value, but in this example the radii are fixed at r. The resistivity of each sphere, ρ_1, is also fixed with the idea that anomalies can arrange themselves in ways to either increase or decrease the desired resistivity effect. In this manner, the inversion is designed to be an iterative process that gives the user the ability to test different scenarios. Finally the resistivity in each mesh cell is defined as

$$\rho(\tau_n, \rho_0, \rho_1) = \rho_0 + \frac{1}{2}(1 + \tanh(a\tau_n))(\rho_1 - \rho_0) \tag{A.4}$$

and the derivatives for the Jacobian matrix are calculated in the same manner as Equation 3.23, without the need for derivatives with respect to skewing parameters which no longer exist. To compensate for the rigid form of the sphere, the mesh is populated with many spheres, i.e. 100 or more, allowing the inversion the flexibility to fit non-linear target features not well suited for a Gaussian ellipsoid parameterization. With a large number of spheres in the inversion, the regularization trade-off term β is set to unity and follows a cooling schedule as described in Chapter 2 with a cooling factor $\gamma = 0.9$. This ensures there exists a penalty term for deviating from a reference model, which prevents the spheres from scattering eas-

ily throughout the model. A much more conservative cooling schedule is needed compared to previous chapters, otherwise the effect of the regularization is too mild and spheres begin to spread out too quickly.

A.3 Synthetic Example

To test the multiple sphere approach, synthetic AEM data from Chapter 4 are revisited. In this example, frequency-domain data are used, but similar results are expected for time-domain measurements. The data and inversion parameters are kept the same as Chapter 4, but instead of three Gaussian ellipsoids, the starting guess is composed of 100 spheres of 75 m radius with a fixed resistivity of 1 Ωm. Three cluster centers are spatially chosen from the observed synthetic data, and the initial spheres are split up and populated randomly around these points with a standard deviation of 200 m, 200 m, 50 m in x, y, z respectively. The depth of the cluster centers is chosen to be 60 m, or z = 250 m. This keeps the spheres near the surface and ensures that any depth or dip information from the ensuing inversion comes from the data and not from the initial model. The left panel of Figure A.1a shows a plan slice through the true model at z = 250 m, where cluster centers are shown as black crosses and the location of two East-West cross-sections at y = 7332880 m and y = 7332640 m are displayed in white. These cross-sections through the synthetic model are shown in the right panel of Figure A.1a. Figure A.1b presents a plan view and two cross-sections through the initial guess. The exact nature of the initial guess is clearly user-dependent and will vary, but this example is meant to demonstrate a typical guess when little a priori information is available.

A.4 Synthetic Result

Figure A.1c portrays the synthetic multiple sphere parametric inversion results in plan view and cross-section. In plan view, the spheres are able to reconstruct the true model quite well, and even in cross-section there is some sense of the true dip in all three anomalies. The initial data misfit is 6.3e5, and after 74 Gauss-Newton iterations the final data misfit levels off at 38.1. Recall the data misfit for the Gaussian ellipsoid example was 19.6, so the multiple spheres method does not achieve a similar level of data fit, but it does provide valuable information. If

the anomalies were curved or non-linear the sphere approach would have a much greater advantage, and is worthy of future research.

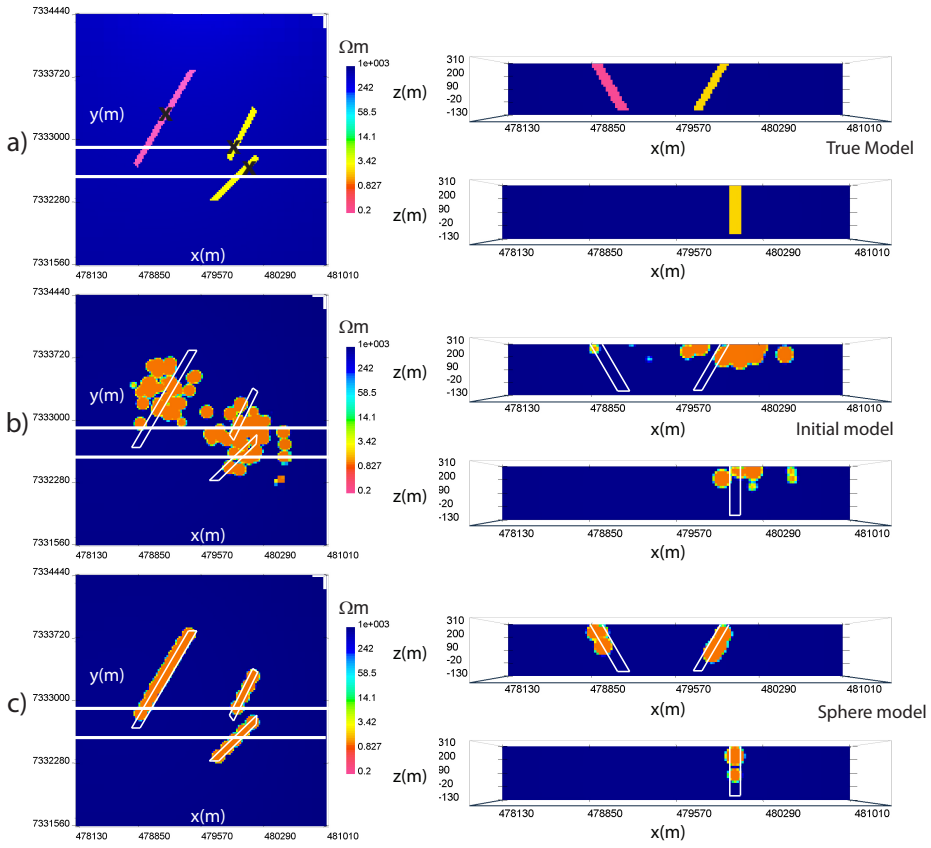

Figure A.1: Multiple sphere parametric inversion, frequency-domain AEM data. Plan view at z = 250 m (left) and cross-section across solid white lines at y = 7332880 m and y = 7332640 m (right). a) True model with cluster centers marked with black x's. b) Initial guess. c) Parametric sphere inversion.

Appendix B

Airborne Electromagnetic Data Sampling

B.1 Total Horizontal Gradient Data Sampling

The survey locations in Chapter 4 are selected through a data reduction sampling method based on the total horizontal gradient (THG) magnitude of the data, defined for time-domain $\frac{\partial \mathbf{b}_z}{\partial t}$ measurements as

$$\text{THG} = \sqrt{\left(\frac{\partial(\frac{\partial \mathbf{b}_z}{\partial t})}{\partial x}\right)^2 + \left(\frac{\partial(\frac{\partial \mathbf{b}_z}{\partial t})}{\partial y}\right)^2}. \tag{B.1}$$

Figure B.1 visually demonstrates the THG sampling method, where Figure B.1a shows the synthetic time-domain AEM $\frac{\partial \mathbf{b}_z}{\partial t}$ data from chapter 4 at 150 μs with the full data set of 1172 source locations presented as black dots. Figure B.1b then illustrates a standard evenly down-sampled $\frac{\partial \mathbf{b}_z}{\partial t}$ data set at 150 μs where every second source location along-line is discarded. Figure B.1c depicts a THG down-sampled data set overlaid on the THG of $\frac{\partial \mathbf{b}_z}{\partial t}$ data at 150 μs. Here, all data points are kept in regions where the THG value remains above a user-defined threshold, 0.06 in this case, whereas outside this core region only every fourth point is selected.

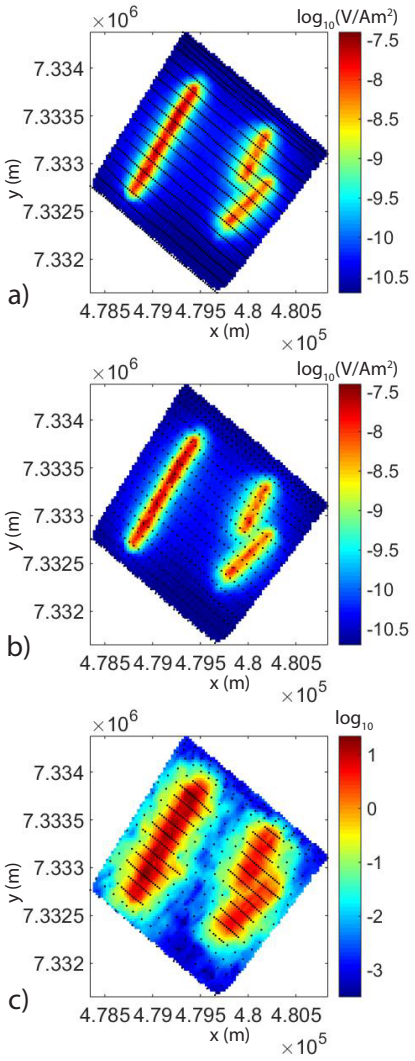

Figure B.1: Time-domain AEM data sampling techniques. Data locations shown as black dots. a) Full synthetic $\frac{\partial \mathbf{b}_z}{\partial t}$ data set at 150 μs with 1172 total source locations. b) Evenly down-sampled synthetic $\frac{\partial \mathbf{b}_z}{\partial t}$ data set at 150 μs with 533 total source locations. c) THG of $\frac{\partial \mathbf{b}_z}{\partial t}$ data at 150 μs with 522 selected source locations based from the THG.

The THG down-sampling technique focuses on keeping data points where the signal is rapidly changing to retain the most valuable information from the data set while eliminating data where the signal is constant or slowly varying. This method is clearly dependent on which time channel or frequency is chosen to calculate the THG. In this example the first time-channel is selected because its THG image is representative of the entire data set, but this may not be the case for every scenario.

Synthetic parametric inversion results are displayed in Figure B.2 for each of the aforementioned data sampling methods. Inversion parameters and meshes are kept to match those from Chapter 4. The left panel shows a 250 m constant elevation slice through the inversion models and the thick white East-West lines depict two cross-section locations at y = 7333080 m and y = 7332780 m that are displayed in the right panel. The true model conductors are outlined in thin solid white and the location of the starting guesses are in thin dashed white. All methods recover an accurate reconstruction of the true conductors in both plan and cross-section; however, the full and THG sampled data inversions have a better overall recovery of the dip of the Western conductor and a closer match to the true resistivities.

Recovered resistivities, total number of Gauss-Newton iterations and final data misfits are displayed in Table B.1. This table shows that the THG sampling method quantitatively has the best result of the three methods with a reconstruction accuracy $\mathbf{R_c}$ of 1.52 when looking only at conductive cells and $\mathbf{R_{All}}$ = 0.17 using all cells in the true model. Note that the evenly down-sampled recovery has a worse reconstruction accuracy of $\mathbf{R_c}$ = 3.27, and also requires 269 Gauss-Newton iterations before terminating and achieves a final data misfit of 31.1. This is compared to only 23 Gauss-Newton iterations and a final misfit of 21.4 for the THG data set. This suggests that a THG down-sampling approach is preferable over evenly down-sampling the data, and little information is lost compared to inverting the full data set. Although this method is presented with a time-domain example, similar results occur for frequency measurements, but are not shown.

Table B.1: Synthetic inversions summary: down-sampling methods.

Model or method	ρ_1	ρ_2	$\mathbf{R_c}$	$\mathbf{R_{All}}$	# GN	Final ϕ_d
True model	0.20 Ωm	2.00 Ωm	0.0	0.0	-	-
Full data	0.14 Ωm	1.94 Ωm	2.01	0.21	22	15.8
Even sampling	0.45 Ωm	1.91 Ωm	3.27	0.30	269	31.1
THG sampling	0.16 Ωm	1.95 Ωm	1.52	0.17	23	21.4

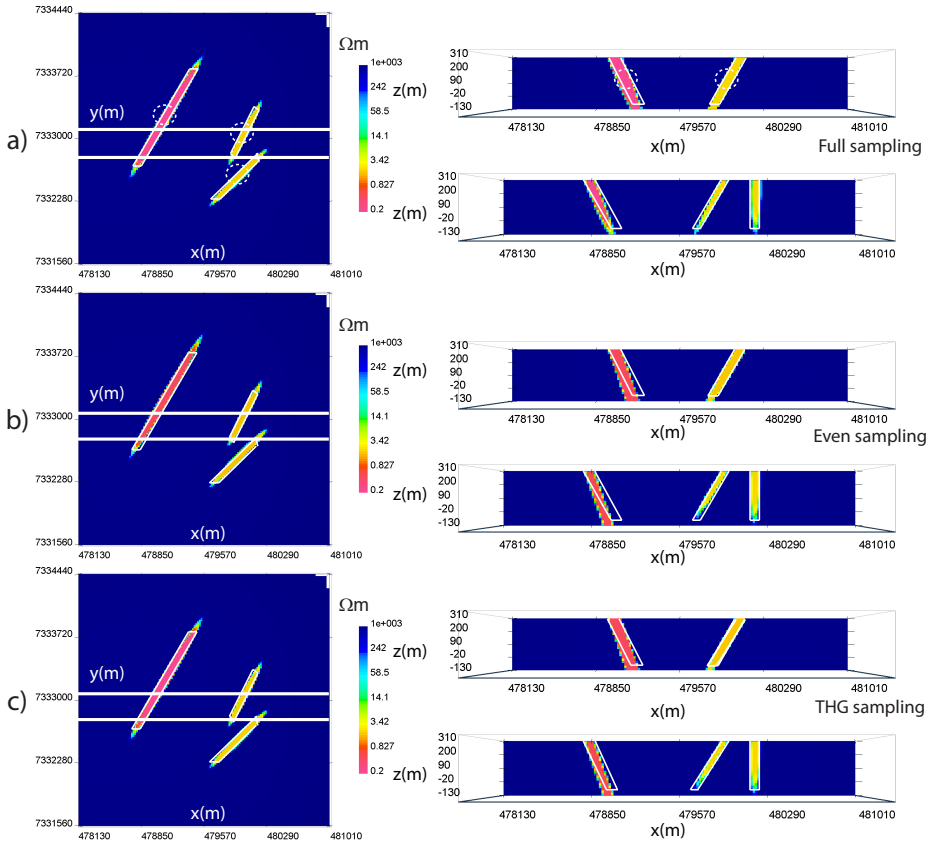

Figure B.2: a) Full sampling. b) Even sampling. c) THG sampling.